



The effects of geometry and dynamics on biological pattern formation

Author: John M. Brooke

Degree: PhD in Computational Neuroscience

Department: Department of Psychology, The University of Sheffield, Sheffield, United Kingdom

Registration number: 180249464

Supervisors: Dr. Stuart Wilson, Dr. Robert Schmidt

Date of submission: 09/2022

Abstract

This project examines the influence of geometry and dynamics on pattern formation in biological development. Since the work of Turing (1952) it has been known that patterns can form spontaneously given certain relatively simple conditions. The Turing mechanism involved a symmetry-breaking bifurcation from a stable spatially homogeneous state. However the development of patterns in developing organisms does not take place from such simple conditions, biological development causes pattern formation to occur within geometric structures which are complex and the environment is very noisy. This thesis examines the effects of such complexity and noise on pattern formation.

The biological situations modelled in this thesis relate to the development of the mammalian cortex. The cortex is a very thin sheet, and there is evolutionary and developmental pressure to utilise cortical space to the maximum. This promotes the formation of spatial superstructures encompassing regions serving different functions. Also cortical development produces two types of pattern, one in the actual physical structure, this is common to much biological pattern formation, but also in terms of patterns of neural response which can be viewed as a feature mapping and is specific to cortical function.

We examine the first type of pattern formation within the barrel field of the rat cortex, a geometric superstructure that has the properties of a Voronoi tessellation and apply a dynamical constraint from the observation that the patterns are sparse. We show that these constraints produce a distribution of patterns closer to what is observed than predictions derived from studies in a single domain of perfect circular shape. We also discover a novel effect of geometric alignment of patterns in neighbouring domains, without any physical communication between them, in a wide class of tessellations. This effect is confirmed by analysis of actual images of the subbarrel patterns in the developing rat cortex.

The effect of geometry and dynamics of the second type of pattern formation is investigated in the patterns of orientation preference of neuronal response in the visual cortex of certain mammals. Where the domains are sufficiently small so that topological defects (pinwheels) cannot form the behaviour is similar to the reaction-diffusion equations. However, when there are many defects in the region alignment at the boundaries disappears.

Contents

1	Constraints on biological pattern formation	1
1.1	Function and process in biology	1
1.2	Morphogenesis and pattern formation in biology	4
1.3	Constraints on biological pattern formation	5
1.4	Cortical maps	7
1.5	Tessellations in the cortex	9
1.6	The role of simulation in understanding biology	11
1.7	Aim and scope of the project	13
1.8	Research question	14
1.9	Contributions	16
1.10	Structure of the thesis	16
1.11	Community contributions	17
2	Simulating biological pattern formation	19
2.1	Pattern Formation	19
2.2	Dynamics of pattern-forming mechanisms	20
2.3	Nonlinear effects	28
2.3.1	Importance of initial conditions	30
2.3.2	Random initial perturbation	31

2.3.3	Hexagonal coordinate system	34
2.3.4	Numerical methods on hexagonal grids	36
2.4	Influence of domain shape on pattern formation	38
2.5	Metrics to evaluate the effects of domain shape	40
3	Cortical domain size alone cannot explain within-domain patterning	45
3.1	Introduction	45
3.2	Results	50
3.2.1	Observational and simulation data	50
3.2.2	Solutions on circular domains	52
3.2.3	Solving on a tessellation	52
3.2.4	Patterns on a square tessellation	56
3.2.5	Properties of solutions on the rat cortex tessellation	60
3.3	Discussion	66
3.4	Materials and Methods	70
4	Correlated pattern formation in adjacent tessellation domains	73
4.1	Preamble	73
4.2	Introduction	73
4.3	Results	78
4.3.1	Bimodal pattern correlations amongst adjacent domains signal boundary constraints	78
4.3.2	Correlated pattern formation in adjacent domains of naturalistic tessellations	81
4.3.3	Measuring the effect of boundary constraints on pattern formation and alignment	82
4.3.4	Correlations are not bimodally distributed if borders are imposed after pattern formation	83
4.3.5	Emergence of bimodal correlations confirms that column boundaries constrain thalamocortical patterning in the developing barrel cortex	86

4.4	Discussion	88
4.5	Materials and Methods	93
4.5.1	Numerical methods	93
4.5.2	Derivation of a test for the influence of boundary shape	94
5	Constraints on topological feature-map self-organisation	101
5.1	Introduction	101
5.2	Results	104
5.2.1	Construction of a model for pattern formation	104
5.2.2	Swift-Hohenberg equations	107
5.3	Effects of boundary shape	109
5.3.1	Periodic and noflux boundary conditions	109
5.3.2	Comparison of patterns across boundaries	114
5.4	Materials and Methods	115
5.4.1	Weakly nonlinear analysis	115
5.4.2	Amplitude dynamics	119
5.4.3	Numerical methods	122
5.5	Discussion	123
6	The effects of geometry and dynamics on biological pattern formation	125
6.1	Review of research question	125
6.2	Implications for biology	127
6.3	Implications for mathematics	129
6.4	Future work	131

Chapter 1

Constraints on biological pattern formation

1.1 Function and process in biology

The success of the theory of evolution by natural selection in the 19th century and the discovery of the genetic code and its role in the transmission of a blueprint for development for living organisms in the 20th century have encouraged the development of a functional approach to explain the structure and of organisms. Traits that enable the survival of an organism are developed by evolution and this process is physically enacted by gene transmission and expression. Alongside this there is another tradition which looks at organism development and structure in terms of the physical processes within the organism and with its environment (Thompson, 1917). These are complementary views of evolution and development because the genetic information acts on physical processes and utilises them, and vice versa, (Kauffman and Goodwin, 1990). In this way, much of the information necessary for development does not have to be completely in the genetic code, but rather the code can guide a complex chain of processes whose dynamics derives from the laws of physics. (Green and Sharpe, 2020) argue that positional information that can be genetically encoded and the physical processes of reaction-diffusion are complementary

rather than antagonistic.

(Schrödinger, 1944) pointed out that it is necessary for a living organism to protect itself from the normal direction of the physical processes of entropy. Living cells are surrounded by selectively permeable membranes and can export unwanted entropy which then has to be dissipated as waste products by the organism. He therefore postulated that some robust mechanism for handing on such structure must exist and this was soon after explained by the discovery of the structure of DNA. Thus a key feature of the development of biological structure is orchestration of physical processes by information bearing molecules. If this sequence is interrupted either due to defects in the genetic code or by catastrophic events in development the consequences can be devastating for the organism. In terms of the physical processes that have been co-opted by evolution they need a certain robustness against the thermodynamically noisy environment.

Physical processes have their own laws, separate from genetic control and outside the influence of natural selection. When we see structure in biological organisms it may not always have a functional purpose, it may be a byproduct of a physical process only part of whose output is necessary for the organism's survival. Also, the same function may be achieved in differing species by different processes. An example is the patterns observed on the skin of many animals in widely differing environments. (Turing, 1952) proposed a simple but very powerful and flexible physical dynamics to explain such patterns which may or may not have functional advantage. A key contention of this thesis is that it is a legitimate subject of investigation to explain possible physical processes that produce structure independently of whether such structure is currently known to have a beneficial function, leaving open the possibility that such functionality may be discovered later.

This point was made in a very poetic paper (Gould and Lewontin, 1979) which used the illustration of the spandrels of Medieval or Renaissance cathedrals which are triangular spaces where the supports for domed ceilings converge on the pillars that support them. These have been decorated with various motifs and scenes according to the faith and artistic taste of the designers, see figure 1.1. Once created these motifs provide an adaptation to the socio-religious environment of the building. In San Marco,



Figure 1.1. A close up of a spandrel in the dome of San Marco Venice. The arches that span the roof must curve out to span and support the roof but also come to rest on the columns that provide the support from the earth. This convergence produces triangular areas by necessity of the geometry of the supports and column. However they also provide a convenient area for mosaics which amplify the function of the building, in this case to glorify the evangelist St Mark and by extension the Venetian Republic for whom he was the patron saint. (Gould and Lewontin, 1979) point out that it is clearly incorrect to explain the existence of the spandrels by this function and by analogy criticise the trend to explain all biological structure and behaviour purely in terms of the survival benefit it brings to the organism. Reproduced by kind permission of Richard Carter, Friends of Charles Darwin.

Venice, to glorify the Evangelist, in King's Chapel, Cambridge, to glorify the Tudor monarchs. However the spandrels did not come into being for that purpose, they came from the necessities of architectural engineering and were then co-opted for the purposes of art or propaganda. (Thompson, 1917) provides many examples where the form of living organisms can be deduced from the laws of physics, or the constraints of geometry. To take one example, the shape of simple invertebrate organisms in the ocean resemble drops of ink in water. However physical processes in biological organisms are affected by the biological processes of growth, development and evolution. One very striking feature of biological growth is how structure develops from an initially spherical blastoderm and this structure affects the mechanical and chemical processes in the developing organism, so the same physical processes such as elasticity and diffusion react and respond differently in different parts of the organism as it develops. For

example (Waddington, 1948) describes the many complex structural changes that occur in the formation of the wings of *Drosophila*, with each change comes a different pattern of mechanical stresses. When physical processes are studied in physics and applied mathematics it is often in geometries which are simple and idealised making it possible to model them using analytical tools that give rigour and generality to the analysis. In applied domains, such as engineering, the interest is in specific and complex structures. Airflow over a cylinder is too simplified, the airflow is modelled numerically on a digital recreation of a particular wing type and the detail of this particularity is key to improvements in aircraft design. In biology the situation is even more complex because the structures being studied are changing as the organism develops or evolves. Once the organism is adult, say once the *Drosophila* wings have reached their final form, they can be studied in a manner similar to the aircraft wing.

As an example of the interplay of dynamic process and function we can consider the markings on a zebra's skin. These can come from a pattern forming process (Bard, 1981) and the existence of patterns on the skin of so many organisms argues for a generality of process. However it has also been postulated that the zebra's markings confuse the optical systems of flies preventing blood loss and infection from their bites (Caro et al., 2019). The general process can be co-opted for a particular function as with the spandrels in cathedrals and chapels.

1.2 Morphogenesis and pattern formation in biology

A unique feature of living organisms is how they self-organise into complex shapes from a very simple spherical beginning and how reliable this process is. This is so unlike structure formation in the nonliving world that mathematicians have been fascinated with the process of morphogenesis. The French mathematician René Thom considered the structural changes occurring in the embryo which involve changes that seem discontinuous compared to the continuous process of growth (Thom, 1989). Thom explained this in terms of catastrophe theory, (Thom, 1975), where the system evolves on a topological structure in phase space that has critical points such as cusps, where derivatives can be discontinuous and at such points the system can jump to a very different configuration.

This is a very high level view of morphogenesis, the process can also be studied in great detail in terms of the chemical signalling and gene expression guiding the processes. An intermediate view was developed by (Goodwin and Kauffman, 1990), (Kauffman, 1993) where the bifurcations that occur in reaction diffusion equations on a growing domain lead to a code that can cause certain genes to express. For example a bifurcation that produces two regions on an ellipsoidal domain has potential information in that the environment in each half can be given a binary code. After a sequence of such period-doubling bifurcations each region will potentially have a binary code of length equal to the number of bifurcations and Kauffman considers how this can lead to different gene expression in each region so that the genes that sculpt the tissue into the head of the larva are expressed in one part and those responsible for the legs or the rear are expressed in other regions.

When morphogenesis happens on a two dimensional domain it is usually called pattern formation, this is what Turing's original work considered. Two prime systems which can be approximated as 2D domains are the skin and the cortex and it is to these systems that the research of this thesis is particularly applicable.

1.3 Constraints on biological pattern formation

A recent development to attempt to conceptualise and formalise what is different about processes in biology compared to those in the nonliving world is the idea of constraint-closure, (Montévil and Mossio, 2015). A *constraint* is conceived as some structure or process that influences but is not influenced by another dynamical process. The *closure* of constraints requires that all such constraints are produced by other processes in the total system, there are no constraints that need to be applied from outside. They propose that such constraint-closure is a core property of living systems. Applying these ideas over time spans longer than an individual organism can include the whole of a species and even further the whole of the biological web of life within the concept of constraint-closure. This allows living organisms to develop and flourish against the thermodynamic arrow of increasing entropy.

(Kauffman, 2019) claims that this makes biology a radically different discipline from physics, in that every biological organism has a unique constraint-closure structure determined by past evolution, and this is more important than the more general physical laws operating in the organism. By contrast, in physics the laws of gravitation apply in the same way to all the matter/energy in the universe and even to the structure of space-time itself. The celestial mechanics of the solar system can be studied without considering the individual differences between the planets, that Jupiter is a gas giant and Mercury a rocky planet with no gaseous envelope. Arguing against this concept is the observation that certain key physical properties are common to all biological organisms. The unique behaviour of water compared to other liquids, for example its ability to dissolve a wide range of chemicals to form electrolytic solutions, is essential to all living organisms but such properties are determined by the molecular structure of water which is outside the ability of any organism to alter. Other physical processes such as diffusion, advection, conduction, convection operate throughout both the living and non-living world. These physical processes can be modelled generally, for example by considering them operating in an idealised domain, without reference to any specific organism.

Since this thesis is based on the use of numerical simulation in order to understand certain behaviour and structures observed in the mammalian cortex, it is relevant that for such modelling to be computationally tractable given current resources, many details have to be left out of the model. This is similar to the situation in physics, in many models of the behaviour of the solar system, the bodies within it are idealised as points or spheres interacting by general mechanisms such as gravitation and collision. This is discussed in the context of the specific systems of chapters 4, 3, 5. Also, in an experimental context, organs, tissues and cells can be taken out of the constraint-closed total system and studied for their reaction to external manipulation. A key distinction here is the difference between the ultimate properties of biological systems acting as Kantian wholes, (Kauffman, 2019), where the parts exist for and by means of the whole, and the study of the behaviour of the parts separately. Both viewpoints are relevant to the study of organisms and they can be complementary rather than antagonistic.

An important constraint on the development of an organism is its environment. This might sound contradictory, the environment is by definition outside the organism. However what is key is the interaction

of the organism with its environment and this is a property of the behaviour of the organism. Particularly relevant to this thesis are the sensori-motor systems that develop in the central nervous system. The sensory organs of vision, hearing, touch, smell etc. provide information to the developing brain and this influences its development. If the sensory input is not typical for the organism, say owing to damage to the sensory organs, the brain will develop atypically. The tissues of the central nervous system are a precious and expensive (in energetic terms) resource and if an area of the brain normally devoted to processing visual information no longer receives such information, it may be rewired to process other sensory input, e.g. auditory. However this plasticity is strongest in certain key stages in development, after such stages it may be impossible or very difficult to change the function of brain regions.

1.4 Cortical maps

In the previous section the issue of the development of different functionality of areas of the brain was looked at in general terms. We now focus on such issues in the neocortex, which is in evolutionary terms the most recent structure in the animal brain and one that is exclusive to mammals. (Krubitzer and Dooley, 2013) survey the evidence for its plasticity and dynamic evolution in the development of individual animals and over evolutionary sequences. This plasticity allows mammals to learn from experience, behaviour is more than a series of pre-programmed responses to the environment but can be influenced by learning, thus allowing adaptation to changing and unpredictable environmental conditions. In individual animals, the development of the neocortex results from a dynamic interplay between the control and guidance from genes and the sensory inputs from the animals sensory system. One of the outcomes of this process is the arealization of the cortex, specific areas of its surface are mapped to particular sensory inputs. For example there are separate regions for processing auditory, visual and sensori-motor input. Although three dimensional the cortex is very thin with respect to its surface and can often be modelled as a sheet, thus we refer to such regions as areas and refer to their development as the arealization of the cortex. This arealization is guided by gradients of markers that attract neurons from particular sensory input, and also by the sensory input itself. For example, restricting certain types of sensory input from the eyes or ears can result in cortical areas normally reserved from such input being assigned to processing

different sensory input. This is an example of *cortical plasticity*.

Related to the plasticity of the cortex is the existence of cortical maps. Here different sensory and motor inputs and output are mapped to specific regions of the cortex. For example the motor homunculus in the human brain is a representation in the somatosensory area of the cortex of the different organs in the body that provide sensory input. This is an example of a topographic map because it maps the topographic structure of the sensory organs onto the cortical surface. Another class of maps are topological maps in which features of the sensory input that are “near” in some feature space, which may be of a higher dimension than the cortical surface. An example of this are patterns in the visual cortex which are related to input from sensory neurons tuned to particular spatial orientations. These form structures known as pinwheels, where thin ribbons of cortical tissue responsive to particular orientations form wheel structures around a focal point (Bonhoeffer and Grinvald, 1991). Regions which are adjacent in the pinwheel are also adjacent in orientation, the description of the map as *topological* because it preserves this adjacency in feature space in the range of the map in cortical space.

Since both topographic and topological maps structure the cortex which is whose primary overall function is information processing, we may ask if either class of maps has advantages for such processing. In examining the case of topological maps, (Wilson and Bednar, 2015) examined four current explanations for topological maps and came to the conclusion that none of them demonstrated convincingly the existence of information processing benefits from the topological structure. However they showed that, using mechanistic models of cortical development, topological maps developed via the statistical properties of sensory input combined with simple rules based on Hebbian learning.

However in terms of cortical development it is important to note that the neurons in the cortex are capable of more complex interactions than Fickian diffusion, which is essentially based on random motions at very small scales, see (Crank, 1975) for further details. This is because neurons influence each other over much longer distances and much more rapidly than diffusion, via synaptic connections. In addition, since the cortex is layered, connections can be made horizontally in different layers that can affect layers above and below by vertical connections. In terms of relevance to cortical maps, (Wolf, 2005b) shows that in

a plausible model of cortical development, pinwheel organisation and long range inhibitory interactions between regions on distant pinwheels that represent the same orientation are necessary for stability. Thus, the organisation of topological maps can be governed by physical processes linked to simple rules for interactions between topologically nearby inputs. Based on this, mechanistic computational models have been developed that include such long range and inter-layer effects, for example LISSOM (Bednar and Miikkulainen, 2006) and GCAL (Stevens et al., 2013). Due to these long range effects, there is no reason to suppose that the structures that develop in these models will be the same as those that appear in the solutions of the reaction diffusion equations.

1.5 Tessellations in the cortex

Where there is competition for space between competing centres, a particular form of tessellation known as a Voronoi tessellation is likely to arise. This is a collection of tessellated regions, each of which has a single point such that all points in the region are closer to this point than to the points of any other region. These points need not be, and usually are not, coincident with the centroid of the region. (Honda, 1978) showed that a number of biological tissues were Voronoi tessellations (the paper refers to them by the name Dirichlet domain which is applied to 2 dimensional Voronoi tessellations). He derived a metric that would measure how close any tessellation was to the Voronoi structure and showed that a range of cell cultures, for example epithelial cells, formed Voronoi tessellations. (Honda, 1983) applied the same analysis to the cells of starfish embryos under the influence of tensile stress as the embryo developed and became constrained in space.

(Senft and Woolsey, 1991), used Honda's methods to show that the barrel field in the mouse somatosensory cortex was a Voronoi (Dirichlet) tessellation. Wilson and James 2021 provided a model which showed how such a tessellation could arise from regions built around competing centres and organised by morphogen gradients. They showed that images taken from the rat cortex also had Voronoi structure. (Petkov et al., 2006) demonstrated that regions in the macaque auditory cortex that responded to particular frequencies were arranged in a tessellation with three primary regions with surrounded by eight

secondary ones. This structure was not Voronoi but was approximately rectangle, with an inner rectangle of three regions surrounded by eight outer ones. Krubitzer et al. 2009 showed that different functional regions in the mammalian cortex had the adjacency characteristic of a tessellation, though again not a Voronoi structure.

It is noteworthy that the examples given above apply to the somatosensory cortex. Many authors, going back to the pioneering work of Ramon y Cajal, have presented evidence that this part of the cortex is organised into vertical structures called columns which span all six layers of the cortex. These units repeat and it has been shown that they respond to different stimuli within the same overall sensory field, for example (Hubel and Wiesel, 1959), (Hubel and Wiesel, 1962), (Hubel and Wiesel, 1963), showed that columns in the cat V1 visual cortex responded selectively to stimuli with a particular orientation, and passing tangentially over the cortex the orientations of the columns varied. It has been proposed that these columns have a functional purpose, however many of the considerations discussed above in terms of cortical maps apply here also. Reviewing the literature, (Purves et al., 1992) proposed that rather than being due to function the columnar structure is an incidental consequence of the rules of synapse formation. The functional areas described as tessellations appear to be aggregations of columns responding to different aspects of the sensory input processed by the whole area.

It is possible to see why this organisation might arise, particularly in the sensory cortex where input to the cortex comes from particular organs with specific neuronal pathways from the sensory organ through the lower regions of the brain to the cortex. In this context, the pattern of the rat and mouse whiskers can be observed in the brain stem as barrellettes and in the thalamus. Since cortical area is a precious resource, regions that tessellate will utilise this space more efficiently than those that do not. As evidence for this, if sensory inputs are cut out, for example by excising the whiskers of a rat or by covering the eye of a kitten the tessellation rearranges so that other inputs are assigned to the non-utilised cortical area. If extra input is applied as in (Constantine-Paton and Law, 1978) who grafted a third eye onto a frog, input from the eye structured the optical tectum (amphibians do not have a cortex) and formed stripes similar to mammalian ocular dominance columns.

1.6 The role of simulation in understanding biology

In any form of investigation, experimental or numerical, which is designed to help towards understanding how organisms and their subsystems develop and function in the full complexity of their environment, drastic simplifications need to be made. In experimental work it may be necessary to put an animal in a scanner, or to study its behaviour in an artificially structured environment. The experimental situation must be simplified to the extent that simple measurements or answers to “yes-no” questions can be deduced from the experiment. Francis Bacon expressed this brutally when he claimed that it is necessary to “put Nature on the rack in order that she confess her secrets”, given that Bacon acted as a prosecutor for Elizabeth I one can see how he might have arrived at this analogy, but then in the 16th century experiments did not have to seek approval from ethics committees. There are aspects of scientific investigation that do not need such control and structure, field work in ethology being an example, but they are relatively restricted compared to the total scientific investigation of living things.

The development of mathematical methods in biology has allowed us to conduct investigations in a universe of mathematical objects that is far removed from the universe inhabited by living things. Early examples are the development of the Hodgkin-Huxley model of neuronal spiking. Such mathematical models rely heavily on experimental work both to formulate the model and to validate its conclusions. The fact that such mathematical models can help in understanding nature is a profound question, “the unreasonable effectiveness of mathematics in the natural sciences” as Eugene Wigner expressed it. However mathematical systems cannot be solved exactly (analytically) unless they are very simple. With the advent of digital computers and the exponential explosion in their computational capability has come another method of investigating biology by computation. This can be by using methods of numerical mathematics to solve systems of equations that have no exact or closed solutions, or increasingly by directly creating computational structures whose interactions and dynamics are claimed to mimic those of living organisms.

This introduces a potential tension between scientists who study biology via experimentation and those who use computation. In order to develop efficient computational models they may be structured and

controlled by numerical parameters where the experimentalist is increasingly unable to recognise the biological factors they understand in the computational system. The increasing use of computation based on methods of artificial intelligence exacerbates this further, since the modelers who set up the AI system may not themselves understand how it makes predictions.

We also need to draw a distinction between models that can reproduce known behaviour and those that can actually make predictions that can be tested via experiment or observation. It has been discovered that by tweaking parameters and inputs, even very simple mathematical models can produce a wide array of behaviour, a classic example is the logistic equation. So, if a numerical model is developed that can reproduce some observed structure or behaviour, how confident can we be that it is telling us something about the biology it is claiming to represent? Maybe a very different model could reproduce the same result. Also, we need to look at any solutions of the model that are not observed, why might they not be observed if they are outputs of the model just as the observed ones? This can lead to a fruitful interaction between computational modelling and experiment because it may be that these effects have not been observed simply because they have not been looked for, thus stimulating further experimental enquiry.

One very important idea that has developed in the mathematical world is the concept of universality. Namely that different mathematical systems may produce the same behaviour even though their terms and structures are not the same. This is explored in more detail in the next chapter. The underlying mathematical constructs that underpin such concepts can be of more profound relevance to understanding the phenomena being studied than the details of the models. An example of this is a symmetry group. Living organisms often have symmetries, bilateral in terms of humans, rotational in terms of organisms with multiple protrusions, e.g jelly fish, hydra, cephalopods. Symmetry is a concept that can be immediately observed in living systems and is also a deep mathematical concept that can link together widely differing systems. Symmetry groups will form an important background to the investigations in this thesis. This concept leads to look at the properties of classes of solutions rather than individual solutions. In the same way symmetry properties can apply across a whole species even though each individual deviates slightly from the abstraction applied to the species as a whole.

1.7 Aim and scope of the project

The aim of this project is to understand how the geometry of regions in which dynamical pattern forming processes occur influences the evolution of patterns. This aim is of importance in computational biology because organisms develop from a spherical blastoderm by a series of complex geometric transformations, each one of which influences the development of later structures. This occurs in four dimensions, three of space and one of time. The focus in this project is the development of dynamics in the mammalian cortex which is a relatively flat structure consisting of multiple layers. These layers may have complex convolutions in 3D space, as is the case with mammals with a folded cortex, or as sheets with a simpler relation to the surrounding space, as is the case with mammals whose brains have a laminar structure.

In this project we neglect the effects of three dimensional folding and model our domains as sheets. A particular focus is on domains that are subdivided into subregions that fit together. The mathematical idealisation of such domains is a tessellation and there is evidence that tessellated structures are widely found in brains and in the cortex in particular. The fundamental hypothesis that is explored in this project is that the structure of tessellations produces profound effects in the dynamics occurring within in them. Domains in tessellations have two extra properties that isolated shapes do not. Firstly we can investigate the effect of adjacency, adjacent shapes in tessellations can share edges which in general shapes in the tessellation do not. Secondly, the structure of the tessellation produces a statistical distribution of shapes which is a property of the overall tessellation itself rather than of the shapes individually.

It is not the claim of this work that shape, individually or in tessellations, is the sole or even the major driver of the effects of developing geometry on the dynamical unfolding of the morphology of the brain or of biological structures more generally. However, the methods of analysis we develop for studying the dynamics in an ensemble of structures are potentially of relevance in studying the overall morphological unfolding in the development of organisms. In this respect we follow recent thinking on the features of biological dynamics that distinguish it from dynamics in non-living systems. Montévil and Mossio (Montévil and Mossio, 2015) discuss this uniqueness in terms “closure of constraints”. A con-

straint is envisaged as an influence on a dynamical process that is not itself changed by the process, an enzyme in a chemical reaction is an example. The concept of closure is that the constraints themselves are all produced by dynamical processes within the total dynamical system at different length and time scales. So in the example of the enzyme, this might be produced by a process evolving on a much slower time scale than the reaction being studied so that the enzyme concentration appears to be unchanging with respect to the immediate process. The property of closure is that all constraints are produced within the total system there is no need for external input.

This concept is a stage beyond the concept of self-organisation. For example, spatial structures can spontaneously form in chemical reactions, such as the well-studied Belousov-Zhabotinski reaction, however to keep the reaction going, fresh supplies of the reactants have to be introduced from outside to keep the structures going. In a system with constraint closures, we would consider a total dynamical system that also produced the reactants in another part of the overall dynamics. Although the organism may need to ingest substances from outside itself, it does so autonomously. (Kauffman, 2019) describes this as “work-task closure”.

In terms of this project a tessellation is considered as a constraint on the dynamical processes operating in the domains of the tessellation. We also restrict the dynamical processes we study to those of pattern formation on a two dimensional surface as an idealisation of a sheet of tissue. Thus we only consider a subsystem of the developing organ, which is itself a sub-system of the total developing organism. Nonetheless, it will be demonstrated that there is sufficient complexity and novelty in studying the effects of tessellations as constraints to provide important tools and insights into the study of the morphological development of organisms.

1.8 Research question

The overall research question in this work is: how can we evaluate the effects on pattern formation caused by the shape of the domain in which the patterns form and dynamical constraints on the process? In biological development in general and in cortical development in particular, rapid growth within a tightly

bounded volume and structural changes from an initial spherical blastoderm produce a variety of shapes and superstructures of shapes within which further pattern formation occurs. Despite having been proposed 70 years ago, Turing's original conception of pattern formation is still stimulating new avenues of research as, for example, presented at recent special meeting of the Royal Society (Krause et al., 2021b), (Krause et al., 2021a). One extension is the study of pattern formation on curved manifolds, e.g. (Varea et al., 1999), (Krause et al., 2018), where diffusion is represented by Laplace-Beltrami operator which is a generalisation of the Laplacian operator used in flat manifolds. Pattern formation in multi-domain models is another extension. An example is the study of bulk-surface models where the dynamics is different in a layer near the boundary compared to the interior of the domain, (Gomez et al., 2021). This has relevance to the study of pattern formation in cells where such different dynamics may be expected due to the differentiation of the cell membrane from the cell body. Pattern forming mechanisms can exhibit novel behaviour when they occur on growing domains, e.g. (Crampin et al., 1999), (Seirin Lee et al., 2011).

The avenue of research which is closest to that presented in the present work is the study of the Turing mechanism on networks, where there can be dynamics within nodes and between nodes. Turing's original paper contained an example of pattern formation on a ring of cells and (Othmer and Scriven, 1971) re-ignited interest in the idea since when the literature has expanded greatly, e.g. (Asllani et al., 2014), (Muolo et al., 2019). The present work focusses on pattern formation in irregular shapes, especially when organised in tessellations. This differs from the above research on pattern formation in two major respects. The first is that tessellations have geometrical as well as topological structure. The second is that in research on networks there is some physical influence connecting the nodes, for example diffusion of substances, whereas in the present work there is no physical transfer between the regions of the tessellations, all effects that are produced by the structure are produced by the geometry of the tessellation alone.

Pattern formation in tessellations brings two research questions, Firstly, how does the statistics of the variety and size of shapes comprising the tessellation affect the patterns that form? Secondly, are there any correlations between the patterns in adjoining regions, even though the walls of the tessellation

prevent any physical communication?

The first question is addressed in chapter 3 in investigating pattern formation in tessellations based on images of the rat barrel cortex. In chapter 4 the second question is addressed in a more general class of tessellation. Both these refer to a particular process of neuron formation in an empty region, in chapter 5 the methods and results are tested in a different type of pattern formation, the development of feature maps in the cortex, specifically the orientation preference columns of the mammalian V1 and V2 cortex.

1.9 Contributions

A preliminary version of the work discussed in Chapter 4 was presented as a poster at the UK Neural Computation Conference, Nottingham July 1-3 2019.

The work presented in Chapter 4 was published in PLOS Computational Biology as *Biological action at a distance: correlated pattern formation in adjacent tessellation domains without communication*, J.M Brooke, S.S. James, J-A Jimenez-Rodriguez and S.P. Wilson, PLOS Computational Biology, 1553-734X, pages e1009963.

I gave a presentation entitled *Pattern formation in the developing brain* at the meeting *Celebrating Alan Turing's work in mathematical biology*, University of Sheffield, September 29 2021. I presented the background to the work of the Self Organisation Lab.

It is intended to submit the work presented in Chapters 6 and 7 to journals in the near future.

1.10 Structure of the thesis

The rest of this thesis is structured as follows

Chapter 2 Simulating biological pattern formation.

Chapter 3 Cortical domain size alone cannot explain within-domain patterning.

Chapter 4 Correlated pattern formation in adjacent tessellation domains.

Chapter 5 Constraints on topological feature map self organisation.

Chapter 6 The effects of geometry and dynamics on biological pattern formation.

Bibliography

Chapters 3, 4 and 5 are structured as papers that have been, or are intended to be, submitted to journals. They thus contain their own introduction and discuss the background literature for each of the papers separately in each chapter. Chapter 2 is generic and describes the background and methods that underpin all of the work discussed in the thesis.

In terms of defending the proposed research hypothesis, Chapter 3 shows that the structure of a tessellation and the influences mediated by the tessellation have a profound impact on the statistics of the ensemble of patterns, beyond what could be predicted from investigations within single domains. Chapter 4 demonstrates a novel effect, namely that patterns in neighbouring domains of a tessellation can be aligned to a degree that is much higher than chance and that precise statistical metrics to quantify this effect can be developed and demonstrated, both on the results of simulations and of observations of patterns directly observed from the rodent cortex. Chapter 5 demonstrates the influence of the overall shape and boundary conditions of a region on the statistics of topological defects within the region. This is investigated in terms of the pinwheel patterns observed in the visualization of the orientation preferences of neurons in the visual cortex of mammals that demonstrate such pinwheel patterns.

1.11 Community contributions

The code developed in this project is available via the GitHub pages of the ABRG group at the University of Sheffield at <https://github.com/ABRG-Models/tessellate>. Along with the code are videos of the evolution of the solutions described in the thesis. It is intended to integrate features of the code into the morphologica library <https://ABRG-Models/morphologica>, which is being used by researchers working in developing computational and visualization code in C++.

Chapter 2

Simulating biological pattern formation

2.1 Pattern Formation

In this section we describe the mathematical and numerical underpinning of the research to be presented in chapters 3, 4 and 5. As described in chapter 1 we are interested in how pattern forming processes can be shaped by the particular shapes and superstructures of shapes found in the cortex and thus to derive methods and results that can further understanding of how organisms co-opt physical processes to meet their needs.

Arguably the most fundamental and influential theory of how physical processes and produce patterns that are characteristic of biological organisms is Turing's model of morphogenesis via reaction diffusion processes (Turing, 1952). In the basic model, Turing imagined two different chemicals A and B, such that A excited production of both A and B and B likewise inhibited both. If a fluid with A and B perfectly mixed is subject to a perturbation such that the concentration of A (say) is increased at a given point this will stimulate production of both A and B. Turing supposed that A and B diffused at different rates, with B faster. In this case around the peak in A will occur a ring of B which will suppress both A and B. Therefore in the central region A will dominate and in the ring surrounding it B will dominate. If the ratio of the diffusion constants is in a certain range, then a perturbation of a specific wavelength will be

amplified and spatial homogeneity will be broken. Turing's work was so far ahead of its time that for a long period it was not utilised. Moreover the analysis is linear in the sense that it can show that certain perturbations have a positive growth rate but it cannot predict how or if the patterns will be stabilised. This requires nonlinear stabilising terms which make analysis by analytical methods difficult. By the 1970s methods for solving partial differential equations using nonlinear terms and in domains closer to biological structures led to methods of modelling pattern formation by what are called "reaction - diffusion" equations. A very influential model was introduced by (Gierer and Meinhardt, 1972). Given the rapid increase in computing power more complex and more realistic dynamics could be modelled and there has been a growing body of literature on such equations, which is still a vibrant research topic, see e.g. the proceedings of a recent Royal Society meeting on the topic (Krause et al., 2021b).

Objections to Turing's model have been that it seems to require chemicals to behave in very prescribed manner and there is no evidence of such coordination in biological situations. However as mathematical understanding of the behaviour of nonlinear partial differential equations has grown it has been realised that the dynamics Turing was proposing does not depend on the details of the necessarily very simple systems he analyzed, but equations with a mix of terms that produce local nonlinear dynamics can react with diffusive processes to produce a very rich variety of phenomena and that different physical mechanisms operating under this broader framework can produce similar behaviour.

2.2 Dynamics of pattern-forming mechanisms

We first of all review the linear theory of pattern forming instability in systems with diffusion. The basic Turing model and its extensions consider only diffusion and terms representing local reactions (e.g. chemical reactions), these are called reaction-diffusion systems. In the simplest cases the stabilising nonlinearities are in the reaction terms and the diffusion terms are linear. One such system examined later in this work is the Schnakenberg system (Schnackenberg, 1979) which has nonlinearities which are simple and of low order but the system is still capable of more complex behaviour than forming static patterns.

It is also possible to have no linearities in the spatial terms of the equation. In chapters 3 and 4 we examine the behaviour of the Keller-Segel equations (Keller and Segel, 1971) which were originally designed to term involving a spatial operator which is nonlinear and acts oppositely to diffusion, it tends to concentrate the fields in the equations. This system, originally designed to model the growth of bacterial colonies was adapted by (Ermentrout et al., 2009) to model pattern formation via the growth of neurons in the cortex.

This model considers two spatial fields, one representing density of neurons and the other the concentration of a chemoattractant that promotes the growth of neurons. The chemoattractant is produced by the concentration of neurons, thus the two dynamical equations for the development of the concentration of neurons and chemoattractant are coupled. The equations are,

$$\begin{aligned} \frac{\partial n(\vec{x}, t)}{\partial t} &= a - bn(\vec{x}, t) + D_n \nabla^2 n(\vec{x}, t) - \chi \nabla \cdot (n(\vec{x}, t) \nabla c(\vec{x}, t)) \\ \frac{\partial c(\vec{x}, t)}{\partial t} &= f(n(\vec{x}, t)) - \mu c(\vec{x}, t) + D_c \nabla^2 c(\vec{x}, t) \end{aligned} \quad (2.1)$$

Here x is to be understood as a two dimensional vector giving the position on the cortex, and $n(x, t)$ and $c(x, t)$ are the concentrations of neurons and chemoattractant at a given point in time and space. In the first equation a represents the rate of production of neurons and b is the rate of pruning. D_n is a parameter representing the strength of diffusion of the concentration of neurons, controlling the size of the second diffusion term. χ controls the strength of the final term which represents the interaction between the gradients of neuronal concentration and concentration of chemoattractant, a mechanism called chemotaxis. This is a nonlinear term which involves spatial gradients, making the system more complex than a pure reaction-diffusion system.

This nonlinearity makes the equations much more difficult to analyse, but correspondingly makes the range of behaviour of the solutions more dynamic and interesting. In the second equation $f(n(x, t))$ represents the production of chemoattractant in terms of the concentration of the neurons which are conceived as stimulating the production of chemoattractant. The second term represents the decay of the chemoattractant the strength of decay is controlled by the parameter μ and D_c controls the strength of

spatial diffusion of c in the final term on the right.

We now present a standard way of analysing the breaking of spatial homogeneity via these equations a method that involves linearising the system and using a standard trial function, also called an ansatz, which allows the spatial partial differential operators to be represented by algebraic terms and thus reduces a system of differential equations to algebraic equations. The method is called linear instability analysis. It has been applied to many different systems with reaction and diffusion terms (Murray, 1984), (Murray, 1989). The presentation given here is adapted from (Ermentrout et al., 2009). As with the classical Turing analysis we consider the breaking of homogeneity in a system that has a stable spatially homogeneous state, by trial functions representing perturbations to this state. To narrow the range of parameters we set $a = b = 1, \mu = 1, f(n) = \beta \frac{n^2}{(1+n^2)}$ following (Ermentrout et al., 2009). We are predominantly interested in the effects of the spatial terms and select the form of the nonlinearity $f(n)$ so that it saturates for large n . With these values we can find a steady state homogeneous solution to (2.1) by setting the time and spatial derivatives of 2.1 to zero. This yields $n = 1, c = \beta/2$.

To perform a stability analysis of this steady state homogeneous solution we linearise the equations by considering small perturbations of the form $n(x, t) = 1 + N(x, t), c(x, t) = \beta/2 + C(x, t)$, so (2.1) becomes:

$$\begin{aligned} \frac{\partial N(\vec{x})}{\partial t} &= -N(\vec{x}) + D_n \nabla^2 N(\vec{x}) - \chi \nabla^2 C(\vec{x}) \\ \frac{\partial C(\vec{x})}{\partial t} &= f'(1)N(\vec{x}) - C(\vec{x}) + D_c \nabla^2 C(\vec{x}) \end{aligned} \quad (2.2)$$

where $f'(1)$ is the derivative of $f(n)$ evaluated at $n = 1$. A standard method of analysing such linear PDEs, see e.g. (Murray, 1993) chapter 14, is by using trial functions $e^{\lambda t} \vec{u}(\vec{x})$ which separate the time dependent part $e^{\lambda t}$ of the solution from the spatially dependent part $\vec{u}(\vec{x})$. Given that the spatial structure of the linearized equations (2.2) depends only on the Laplacian operators it is natural to expand $\vec{u}(\vec{x})$ as a linear sum of eigenmodes of the eigenvalue equation for the Laplacian,

$$\nabla^2 \vec{u}_k = -k^2 \vec{u}_k \quad (2.3)$$

Where k is the eigenvector and \vec{u}_k is the eigenmode. If the eigenmode has a norm of 1 it is of form $e^{i\vec{k}\cdot\vec{x}}$ and k is $|\vec{k}|$. For a fixed \vec{k} the solution of (2.3) represents a stationary plane wave with wave number k and the solution space is a set of waves with wave vectors \vec{k} all of whom have the same scalar wave number k , if the solutions are transformed to Fourier space they lie on a circle radius k .

We can represent $S := (N, C)^T$ in the differential equation (2.2) as

$$\begin{pmatrix} \tilde{N}(k) \Re e^{\lambda t + i\vec{k}\cdot\vec{x}} \\ \tilde{C}(k) \Re e^{\lambda t + i\vec{k}\cdot\vec{x}} \end{pmatrix}$$

where $\tilde{N}(k), \tilde{C}(k)$ are the amplitudes of the solutions corresponding to k and the exponentials represent their spatial and temporal behaviour (we use only the real part of the exponential). This represents a spatial wave with wave number k , growing or decaying exponentially at a rate determined by λ . Substituting this trial solution in to (2.2) reduces the differential equation to an algebraic equation of form

$$\lambda \bar{I} \vec{S}^* = \bar{M}(k) \vec{S}^* \quad (2.4)$$

where \bar{I} is the 2×2 identity matrix, \bar{M} is given by

$$\bar{M}(k) = \begin{pmatrix} -1 - D_n k^2 & D_n k^2 \\ f' & -1 - D_c k^2 \end{pmatrix} \quad (2.5)$$

and $\vec{S}^* = (\tilde{N}(k), \tilde{C}(k))^T$, since the exponential components of \vec{S}^* cancel on both sides of the equation.

A Turing instability is produced when a spatially inhomogeneous instability occurs in a system where there is a stable spatially homogeneous state and in the present case this state is stationary in time also. The linearisation (2.2) represents perturbations to the steady state $S = (1, f(1))^T$ of (2.1). However we need to check if this linearisation is stable in the case where the system is spatially homogeneous. We can do this by setting $D_n = D_c = 0$ in the expression for $\bar{M}(k)$. The eigenproblem for this reduced

form of (2.4) gives the condition for λ .

$$(\lambda + 1)^2 = 0 \quad (2.6)$$

which has the degenerate double root $\lambda = -1$ so (2.2) is stable to spatially homogeneous perturbations. Thus if we can find a value for k that gives a eigenvalue λ with a positive real part as a solution of the full system (2.4) then we will have a Turing instability and the eigenmode will give the amplitudes $(\tilde{N}(k), \tilde{C}(k))$ that can be substituted into \vec{S} to give a growing spatially inhomogeneous instability of the linearised equations of (2.1).

There is a result in linear algebra that a necessary and sufficient condition that the real part of the eigenvalues of a 2×2 matrix be negative is that the trace of the matrix is negative and the determinant is positive. Clearly if we restrict D_n, D_c to be positive, the trace of \bar{M} is negative, so if the determinant is positive then the eigenvalues have negative real parts. Thus, for growing solutions \bar{M} to be possible the determinant must be non-positive and the expression for the determinant of M is

$$\Delta_M := 1 + D_c D_n k^4 - k^2 [f'(1)\chi - (D_n + D_c)] \quad (2.7)$$

This is a quadratic equation in k^2 and by differentiating with respect to k^2 we find that the minimum of Δ_M occurs at k_c where

$$k_c^2 = \frac{\chi f'(1) - (D_n + D_c)}{2D_c D_n} \quad (2.8)$$

We can substitute this minimum into (2.7) to eliminate k and after some algebraic manipulation we obtain a quadratic expression for Δ_M ,

$$\Delta_M = \frac{1}{4D_c D_n} [D_c^2 - 2(D_n + \chi f'(1))D_c + D_n^2 - 2\chi f'(1)D_n + (\chi f'(1))^2] \quad (2.9)$$

For instability we require the determinant to be non-positive and for exponentially growing solutions we require it to be negative. Thus finding a value of k where it is zero marks the onset of instability. We have three parameters that can affect the value of the determinant, we choose D_c to be the control parameter for this condition and find a condition expressing it in terms of the other two parameters. Observing (2.9)

we can see that if we set the determinant to be zero, the roots of the equation for D_c will give critical values D_c^* for which the determinant is zero,

$$D_c^* = D_n + \chi f'(1) \pm 2\sqrt{\chi f'(1)D_n} \quad (2.10)$$

From the structure of (2.9) we can see that Δ_M will be negative if D_c is less than the root with the minus sign before the final term on the right, or greater than the root with the plus sign. However there is another condition that must be satisfied for a wave like solution to appear, namely k_c^2 in (2.8) must be positive. It can be seen that this requires the numerator to be positive and this is only possible for the solution of (2.10) with the negative square root. Even with the negative square root we still have to satisfy a further restriction for the numerator to be positive,

$$\sqrt{\chi f'(1)D_n} - D_n > 0, \quad (2.11)$$

that is

$$\chi f'(1) > D_n. \quad (2.12)$$

We can use this condition to further simplify parameter space, by setting χ in terms of D_n . If we follow (2.12) and set $\chi = D_n/f'(1)$ then on substituting into (2.10) we obtain $D_c^* = 0$ which is too restrictive since we would not be able to find a positive D_c that would give a negative Δ_M .

Following (Ermentrout et al., 2009) we create more leeway by setting $\chi = D_n$ giving,

$$D_c^* = [f'(1) + 1 - 2\sqrt{f'(1)}]D_n \quad (2.13)$$

For $D_c > D_c^*$ perturbations to the homogeneous state decay, for $D_c < D_c^*$ they grow and we get pattern formation. If $f'(1) > 1$ we can find a positive value of $D_c < D_c^*$. In the discussion of (2.1) we set $f(n) = \beta \frac{n^2}{(1+n^2)}$ so $f'(n) = \beta(\frac{2n}{1+n^2} - \frac{2n^3}{(1+n^2)^2})$ and at the steady state value $n = 1$ this gives $f'(1) = \frac{\beta}{2}$, so we must have $\beta > 2$. With these extra restrictions of parameter space, if we substitute D_c^* from (2.13)

and $\chi = D_n$ in (2.8) we obtain the wavenumber at the critical value,

$$k_c^2 = \frac{\sqrt{f'(1)} - 1}{D_n(f'(1) + 1 + 2\sqrt{f'(1)})} \quad (2.14)$$

Large k corresponds to patterns with very fine spatial structure, while small k corresponds to coarse structures and the wavelength at instability is given by the parameters of the linearised equation (2.2). In this context the inverse dependence of k on $\sqrt{D_n}$ should be noted. This is to be expected on dimensional grounds since $1/\sqrt{D_n}$ has dimension $1/L$ if we take a constant time scale so the effective dimension of D_n is L^2 rather than the full dimensions of L^2/T . Thus it can be seen that its dimension is the same as k , (inverse of the wavelength). If we follow (Ermentrout et al., 2009) and choose $\beta = 5$ we will obtain the steady state homogeneous solution $S = (1, 2.5)$ and the critical wave number at instability obtained from (2.14) is $k_c \approx 0.087/\sqrt{D_n}$ and the critical value of $D_c^* \approx 0.34D_n$, both results given to two significant figures of accuracy. Accordingly, in the numerical solutions presented in chapters 3, 4 the parameter space to be investigated is simplified by the choice $D_c = 0.3D_n$ and $\chi \geq D_n$ thus ensuring we are investigating the nonlinear fate of a Turing instability.

As k increases beyond the critical value a continuous range of k give perturbations with a positive growth rate. However this only applies if we are solving (2.2) on an infinite domain. If we solve in a finite domain and apply no-flux conditions at the domain boundary then the gradients of the field normal to the boundary are zero,

$$\frac{\partial N}{\partial n} = 0, \quad \frac{\partial C}{\partial n} = 0. \quad (2.15)$$

Only waves that can fit this condition on the boundary of the domain can be observed. Later in this work we will need to solve (2.1) on a disk shaped domain. Given this geometry it is convenient to work in circular polar coordinates. In this coordinate system Laplace's equation, $\nabla^2 = 0$, can be factored into angular and radial equations and we can consider trial functions of the form,

$$v(r, \theta) = R(r)\Theta(\theta) \quad (2.16)$$

where r, θ are the polar coordinates and $v(r)$ stands for either $N(r)$ or $C(r)$. We now solve Laplace's equation in order to obtain a set of functions that satisfy the boundary conditions. This is done by separation of variables (Sneddon, 1966) and we obtain two ordinary differential equations connected by a coupling constant m .

$$\begin{aligned} r^2 R'' + rR' + (r^2 - m^2) &= 0 \\ \Theta'' + m^2 \Theta &= 0 \end{aligned} \tag{2.17}$$

The solutions to the second equation are harmonic functions, $\cos(m\theta), \sin(m\theta)$. Each value of m gives a different form of the equation for R . This equation is called Bessel's equation after the 19th century astronomer who first stated it. For each integer m the solution to Bessel's equation is a Bessel function of the first kind $J_m(r)$. Thus solutions to Laplace's equation in circular polar coordinates are of the form $J_m(r)e^{im\theta}$ and for these solutions to meet the no flux boundary condition for a given radius of r^* we must have that

$$\left. \frac{\partial J_m}{\partial r} \right|_{r^*} = 0 \tag{2.18}$$

i.e. that $J_m(r^*)$ is an extremum. Since the only spatial derivatives in the linearized equation (2.2) occur in terms that have the form of the Laplacian, the functions that fit the no flux boundary condition (2.15) for Laplace's equation will fit the no flux boundary conditions for (2.2) also and the solutions of 2.2 will have the spatial form determined by 2.17. The full equations (2.1) have a nonlinear form for the chemotaxis term (third on the RHS), so they may differ from the spatial form of the linear solutions, their form can only be determined by numerical simulation.

Thus when the domain is finite in size and has no flux boundary conditions, only a limited range of patterns and wavelengths will be selected. In the linear analysis this is how shape affects the solutions. If the domain is differently shaped then a different set of functions will fit the boundary conditions. For example, if the domain has a boundary given by an ellipse, the functions that satisfy Laplace's equation and the no flux boundary conditions are called the Mathieu functions (Abramowitz and Stegun, 1970) chapter 20.

2.3 Nonlinear effects

First of all consider the initial breaking of homogeneous spatial symmetry. According to the above analysis if then we choose a perturbation with a wavelength that will be the fastest growing mode this will grow exponentially and will eventually dominate the solution. However, such an exponentially growing solution will break the conditions of the previous analysis and nonlinear effects will become important. There are two sources of nonlinearity in (2.1). First consider those from the terms without spatial derivatives. These were used to determine the values of the spatially homogeneous, time steady solution $n = 1, c = f(1)/\mu$. However the time dependent equation for the nonlinear reaction terms

$$\begin{aligned}\frac{\partial n(x, t)}{\partial t} &= a - bn(x, t) \\ \frac{\partial c(x, t)}{\partial t} &= f(n(x, t)) - \mu c(x, t)\end{aligned}\tag{2.19}$$

can also have time dependent solutions, thus the spatial symmetry breaking can occur from a time varying, say an oscillating homogeneous state. If we have breaking of homogeneity also so that the Laplacian terms are non-zero we can get solutions that are travelling waves rather than the time invariant wave patterns analysed above. A second form of nonlinearity comes from the chemotaxis operator $\chi \nabla n \nabla c$. This can only be written in the form $\chi \nabla^2 c$ when $n \approx 1$. With its full nonlinear form it becomes a powerful concentration term. It represents concentration, going against the gradient of c , in the equation for n , but when n moves away from its spatially homogeneous value it sculpts the gradient of the cheomoattractant, thus a positive feedback loop can form between the concentrations of n and c resulting in a highly inhomogeneous distribution of both with areas of high concentration forming a small portion of the domain, most of which by contrast is empty.

The linear theory described above can be extended into the nonlinear régime by weakly nonlinear analysis (Manneville, 1990). Here the solution is written as a sum of functions with spatial and temporal structure. The nonlinearities will now couple the set of equations governing the evolution of each component, producing terms of quadratic or higher order. In Chapter 5 such an analysis is shown, but for a different set of equations to 2.1. Constraints of the system, such as symmetries, can restrict the terms that need to

be considered and the condition that the nonlinearity be weak can restrict the order of terms considered. This can give systems that are sufficiently simple that they can be investigated by analytic methods and rigorous statements can be made about the evolution and form of the solutions. However as the nonlinearities become stronger this approach fails because many terms of higher order can no longer be ignored and the system is no longer analytically tractable.

One method of solving systems in the strongly nonlinear regime is to expand the solution in series of basis functions as before but truncated at a much higher order and solve the resulting system numerically on a computer. The order must be truncated at some level, which will be determined by the amount of computing power available. By comparing results at different resolutions an estimate can be made of how well the solutions are converging as the order increases. This method is called Galerkin approximation. In cases where the solutions vary reasonably smoothly in space and time the Galerkin approximation works, in systems that have discontinuities, e.g. shocks and fronts, other methods must be used.

A completely different approach to the nonlinear problem is to discretize the governing equations in space and time on some mesh, which can be regular or irregular, and use this discretization to turn the problem from an infinite dimensional system to a finite dimensional one, replacing continuous operators by discrete matrices and to solve the discrete problem by the methods of linear algebra. The various methods of discretization give rise to different methods of solution finite difference, finite volume, finite element, boundary elements, etc. The methods used in this thesis are a mixture of finite difference (for time derivatives) and finite volume (for spatial derivatives).

The problems we investigate relate to spatial pattern formation and we restrict to patterns that do not also have time dependent behaviour such as travelling waves or oscillating patterns. Our interest is in the eventual time independent solution. In choosing numerical methods to evolve the patterns we can one approach is to write the governing equations as with time derivatives set to zero and solve the spatial structure as an optimisation problem. The PDEs developed are called elliptical PDEs, we discuss this in Chapter 6. An alternative approach is to write the system with the time derivative terms left in and evolve it from an initial condition until it becomes temporally stable (time derivatives evolve to zero).

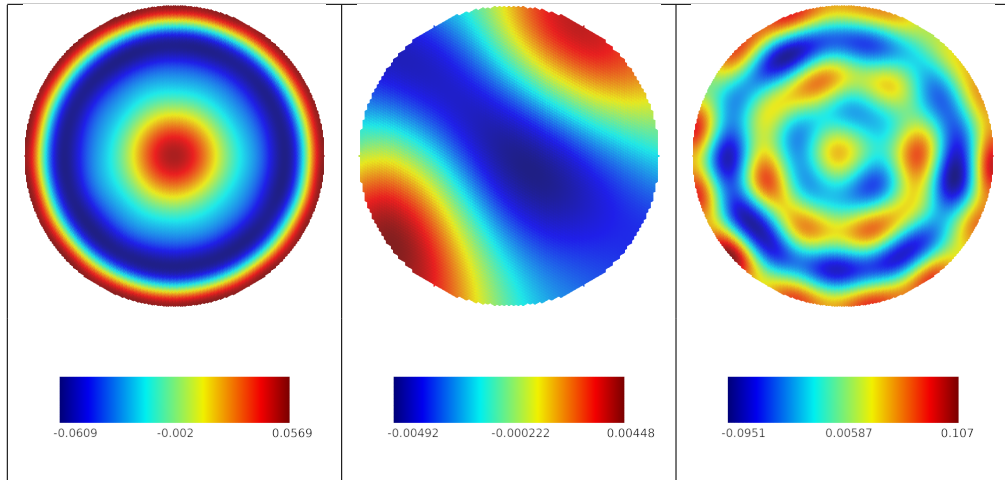


Figure 2.1. Patterns obtained from two differing initial conditions at $Dn = 8, Dc = 2$, on the left from $m = 0$ perturbation, in the middle from a perturbation that is random in space, on the right from a mixture of initial conditions. In this figure, as in all figures in this chapter the colour coding indicates that the maximum field is red, the minimum field is blue and yellow is the median. The field values are perturbations from the steady state solution $n = 1$. The field plotted is n from equation (2.1)

For this to happen the time steady state must be stable. However in nonlinear systems there can be differing solutions that are stable at the same parameter values which are selected by choosing different initial conditions. This is called multi-stability and its existence indicates the care that needs to be taken in describing how a solution was obtained, not only the equations, the parameters and the boundary conditions need to be described, but also the initial conditions.

2.3.1 Importance of initial conditions

The situation in biological structure and pattern formation often does not fit the framework of a previous existing equilibrium that is perturbed. The development can be so rapid and dynamic that static equilibria are never formed. Rather one state provides input into new dynamics. Such dynamics is described as “far from equilibrium” (Prigogine and Stengers, 1984) and principles such as self-organisation from a state which is noisy or chaotic become important.

The importance of initial conditions can be seen in figure 2.1. The top radially symmetric solution was integrated from an initial condition that was radially symmetric, i.e. it had no angular structure. The

middle panel shows the solution generated from an initial field that was uniform random noise. The lower panel shows a solution on the cusp between the other two. It was obtained by starting with a very low amplitude noisy perturbation to the radially symmetric initial field and increasing the strength of the perturbation until the cusp point was reached.

2.3.2 Random initial perturbation

Suppose we are solving equation 2.1 by a numerical method based on discretization of the spatial domain. We set random fields for n and c so that each grid point has a random value that is in a particular range, for example $[0, 1]$. The Laplacian terms are determined by the size of the gradients of gradients (e.g. $\frac{\partial^2}{\partial x^2}$) which will be everywhere very large because there will be large differences between grid points that are close together on the grid scale. There will thus be a period when the evolution is dominated by diffusion at a grid scale. Owing to the averaging property of the Laplacian, regions of field which are relatively homogeneous on the grid scale will become detectable. They can be expected to display heterogeneous spatial structure on much larger length scales corresponding the width of the domain. This initial grid-scale dominated diffusion phase is very rapid. As the length scales become much longer than the grid point distances the numerical method will produce fields that are influenced by the boundary conditions and therefore their evolution is shaped by the geometry of the domain. In figure 2.2 we show the evolution of the field from initially random at the grid scale according to these two phases. In the first phase the scale of the field goes from grid scale to a scale that is recognisibly of the order of the domain, this is shown in the top plots of figure 2.2. In the second phase, shown in the bottom plots, the field organises to attain a configuration that has a definite symmetry with respect to the shape of the region boundary, in this case a bilateral symmetry. The characteristic time scale of the first part of the evolution is approximately 8 times as rapid as the time scale of the second. It can be seen that the symmetry is imperfect, the solution will evolve to have a symmetry closer to perfect but this occurs on a much slower timescale, from the structure of the equations it is likely that it approaches the final configuration exponentially slowly and long term runs seem to confirm this. In practice integrations are terminated after the average of the absolute value of the difference between fields time interval T apart falls below

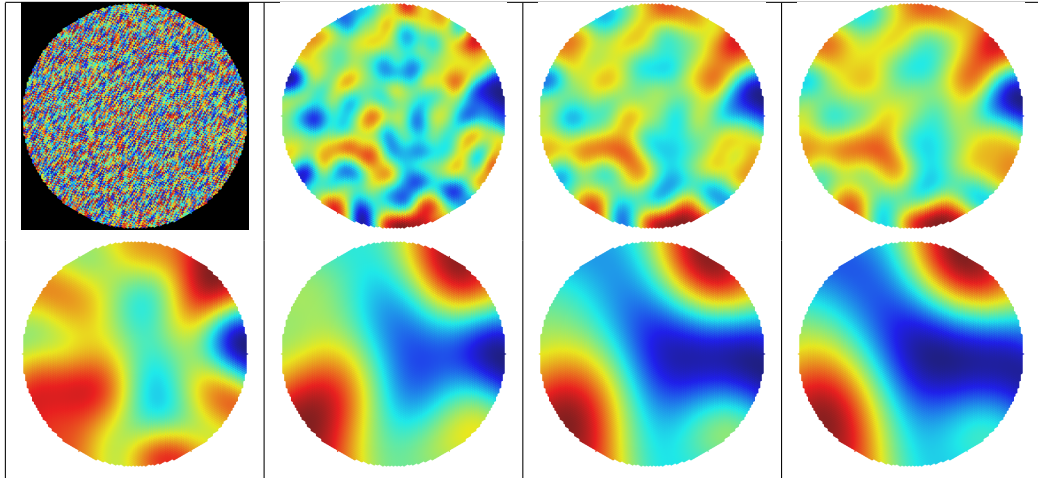


Figure 2.2. Snapshots showing how an ordered field arises from an initial random distribution. Top row: rapid phase of time evolution from a completely random field. The patterns were obtained by observing the solution every 0.24 time units. Bottom row: evolution to a solution that has a clear symmetry with respect to the boundary of the shape. This phase of the evolution was about 8 times slower the snapshots were obtained by observing the solution every 1.6 time units. The control parameters were $D_n = 10, D_c = 3$.

a given tolerance.

We examine the solution evolving in figure 2.2, which has bilateral symmetry with an axis of symmetry that has a clearly defined angle relative to the vertical axis of the image. Now although this solution has grown deterministically from a random distribution and although if we were to feed in exactly the same random distribution at the same scale we would get the same result, if we change the seed and drew a different perturbation from a uniform distribution we may get a different orientation. If our distribution were genuinely random and we continued the process ad infinitum we would expect to get a uniform distribution of symmetry axes. If we represent the direction of the bilateral symmetry axis as a unit vector then these unit vectors will lie on a circle. It should be noted that this space is not the domain of the fields shown in figure 2.2 which is a disk.

Suppose we have an ensemble of random fields evolving on a grid that covers a disk that is the domain of the solution fields where the value of each grid point was drawn from a uniform random distribution. If the ensemble of random fields was sufficiently large (strictly was infinite) and the parameters of the

governing equations were such as to evolve to final configurations that had bilateral symmetry, then we would expect that the unit vectors representing directions of the symmetry axes would be uniformly distributed on the unit circle S^1 . If the distribution of the unit vectors representing the symmetry axes for the ensemble of solutions arising from the ensemble of initial conditions was non-uniformly distributed on S^1 , this would indicate that in the solution fields on the disk there were preferred directions for the axes of symmetry. Since the solutions evolve on a disk which has no preferred directions, we would conclude that the ensemble of initial fields introduced this preference and therefore was insufficiently random. However any grid that can be used for solving the equations on a computer with finite memory would be finite and this in itself could induce biases into the set of eventual directions. However if we consider the limit where the distance between the grid points tended to zero we would expect the distribution of the axis of symmetry vectors to approach uniform distribution on the unit circle. Thus the process of integration gives a mapping

$$H \rightarrow S^1 \tag{2.20}$$

where H is space of all randomly distributed fields. Now consider the process of bootstrapping under the control of (2.1). If we imagine the scale of the discretization tending to zero then on this scale the distance to the boundary will tend to infinity, as opposed to a scale comparable to the size of the domain where the distance to the boundary will be finite. Since in the initial stage of field development the scale is the scale of the discretization, initial structure formation will not be affected by the boundary shape. As the length scale of the field increases via the effects of diffusion the interior field starts to become affected by the boundary shape and the second phase of field evolution leads to an ensemble of solutions whose symmetry group is S^1 . There are two awkward infinities here which are not realised in any numerical discretization, infinite resolution and infinite integration time. However this discussion is a prelude to results presented in later chapters where it is shown that even very small perturbations which provide a structural bias to an initial uniformly randomly distributed initial field can have major effects on the observed solutions.

Referring to figure 2.2 we can consider refining the mapping by considering an intermediate space C ,

$$H \rightarrow C \rightarrow S^1 \quad (2.21)$$

C is a space of fields like those in the upper row, these could be defined as having a typical length scale that is greater than some given fraction of the domain width. One advantage of conceptualising the development of solutions with a given symmetry group, here S^1 from C rather than H is that the randomness of H is defined at the level of grid resolution which is not an intrinsic property of the domain as the fractional length scale is. In biological development it may be that input comes in throughout pattern formation, we examine an example of this is chapter 3, this input will have its own spatial patterns. In most of the results presented in this work we subsume all such influences under the initial field. If we can show that solutions are sensitive to the individuality of the initial field then we have evidence that it is worth the effort of trying to model the influences mentioned above. If the pattern formation is robust to such perturbations then such modelling is of lesser importance.

2.3.3 Hexagonal coordinate system

The equations (2.1) are nonlinear equations, they have no analytic solutions and must be solved numerically by discretizing in space and time and replacing differential equations with coupled difference equations. However the existence of gradients which can be large, particularly as the patterns are developing, means that we have to be careful about how this discretization is handled. The solution adopted here is to discretize on a hexagonal rather than the usual rectangular grid. A hexagonal grid has the property that all points are equidistant from each other and it will be shown that this enables the Laplacian and chemotaxis terms of equation (2.1) to be discretized in an elegant and robust manner.

The hexagonal grid and coordinates are shown in figure 2.3. The points on which the equations are solved are the centre points of each hexagon. There are three coordinates represented by three angles at 120 degrees to each other and denoted as red (r), blue (b) and green (g). Since this is a two dimensional surface each one of the coordinates can be expressed in terms of the others, we choose to work with red

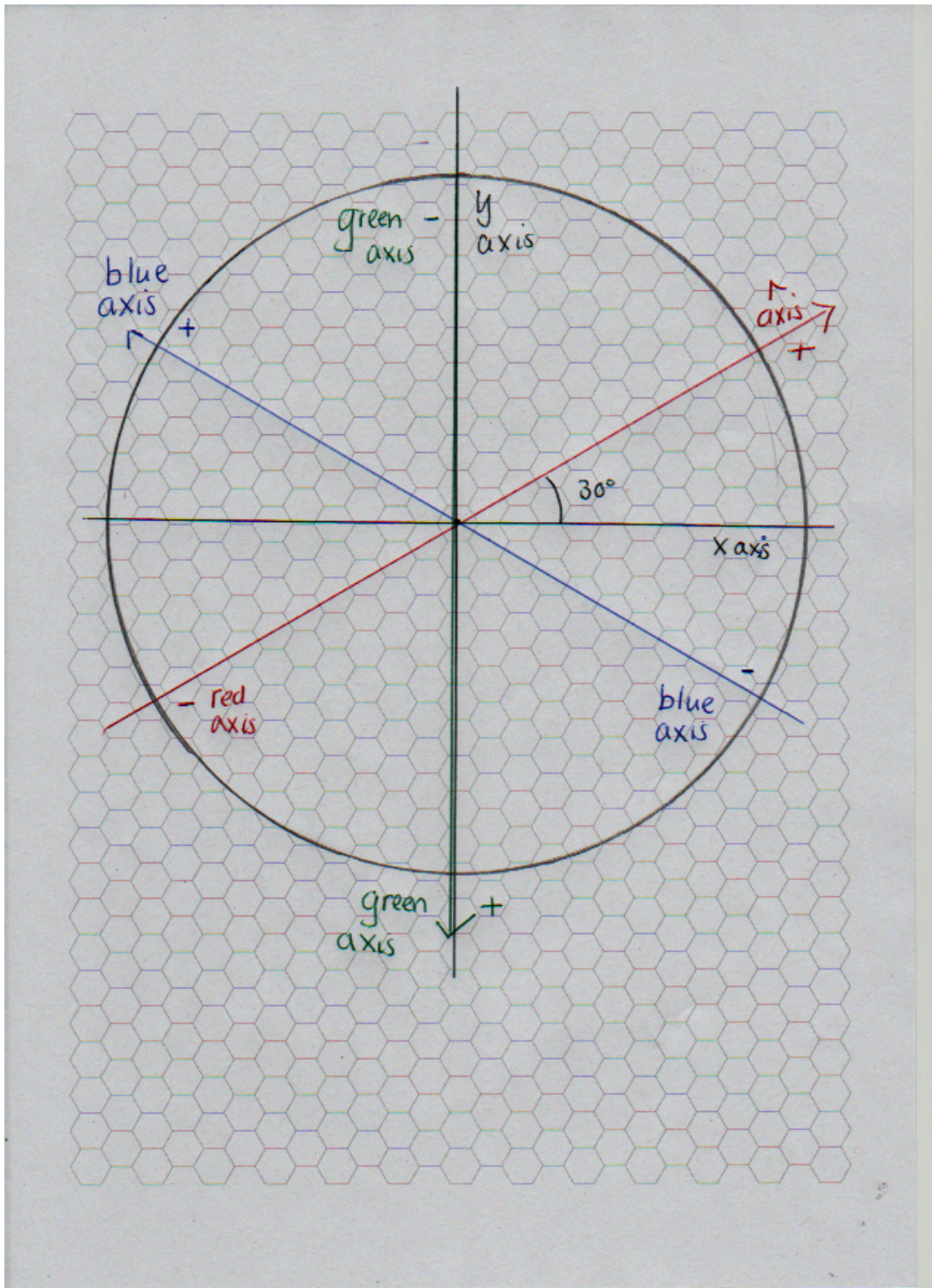


Figure 2.3. Hexagonal coordinate system. There are three axes, red (r), blue (b) and green (g) at 120 degrees to each other. The Cartesian x and y axes are also shown, they are oriented so that the x axis is at a 30 degree angle clockwise to the red axis.

and blue and ignore green. To orient the hexagonal grid with respect to the x and y axes of the normal Cartesian coordinates we choose these axes to be as in figure 2.3. This allows us to use trigonometric relations based on the angles between the axes to express the relationship of the coordinate systems

$$\begin{aligned}x &= \sqrt{3}(r + b)/(2s) \\ y &= \frac{r + b}{2s}\end{aligned}\tag{2.22}$$

where s is a scale factor representing how closely packed the hexagons are relative to a given characteristic length which defines the size of the region of integration.

2.3.4 Numerical methods on hexagonal grids

In reaction-diffusion systems and their extension by terms such as chemotaxis we need to discretize the Laplacian operator ∇^2 and also in its nonlinear form, e.g. $\nabla \cdot (n \nabla c)$. In a Cartesian coordinate system these terms can be discretized in the x and y directions, so

$$\nabla \cdot (n \nabla c) = \frac{\partial n}{\partial x} \frac{\partial c}{\partial x} + \frac{\partial n}{\partial y} \frac{\partial c}{\partial y} + n \left(\frac{\partial^2 c}{\partial x^2} + \frac{\partial^2 c}{\partial y^2} \right).\tag{2.23}$$

It can be seen that if n has no spatial variation this expression defaults to the Laplacian. In Cartesian coordinates it is straightforward to find expressions that express this term in terms of finite differences as approximations of derivatives (Ames, 1977). However the r, b hexagonal coordinates are not orthogonal in a 2 dimensional space with the Euclidean metric. Therefore the derivative expressions in terms of hexagonal coordinates would be more complex, as are the expressions in polar coordinates. In fact it is only in Cartesian coordinates that these expressions have simple forms in terms of the components of the derivatives.

Little has been written about numerical analysis on hexagonal grids. However, (Lee et al., 2014) present an elegant method for discretizing these terms which utilises the nice property of a hexagonal grid that all the neighbouring points are the same distance from the central point, and this is true everywhere in the grid except on the boundary which will be considered separately. The method is called the *finite volume*

method and it uses Gauss's divergence theorem as follows. We wish to assign to the central point in the hexagonal grid the average value of the Poisson term on this point's hexagon, see figure 2.4

$$(\nabla \cdot (n\nabla c))_j = \frac{1}{|\Omega_j|} \int_{\Omega_j} \nabla \cdot (n\nabla c) dA \quad (2.24)$$

where Ω_j is the hexagon corresponding to grid point j and dA is the element of area. We now use Gauss's theorem to remove one level of the ∇ operator and to instead average over the boundary $\partial\Omega$ rather than the interior

$$\frac{1}{|\Omega_j|} \int_{\Omega_j} \nabla \cdot (n\nabla c) dA = \frac{1}{|\partial\Omega_j|} \oint_{\partial\Omega_j} n \frac{\partial c}{\partial \vec{x}^\perp} d\gamma \quad (2.25)$$

where $\frac{\partial c}{\partial \vec{x}^\perp}$ is the component of ∇c normal to the boundary, dA is the element of area and $d\gamma$ is the line element on the boundary. Both are scalar quantities.

We use as a distance unit $\Delta s = 1/s$ where s is the scale factor and Δs is the distance between the centres of neighbouring hexagons. The domain of integration is a hexagon but we use the values of the field at the grid points that form the boundary of the hexagon and the grid point at the centre to discretize the derivatives in the continuous formulation (2.25). The value of n on each edge is given by the average of its values at the vertices which are its endpoints (figure 2.4). The gradient $\frac{\partial c}{\partial \vec{x}^\perp}$ is given by $(c_i - c_0)/\Delta s$, where c_i are the values at the grid points that form the vertices of the hexagon. This simple form for the finite volume approximation comes from the property of the hexagonal grid that all neighbouring grid points are separated by the same distance. The area of the hexagonal grid $|\Omega|$ is obtained by elementary trigonometry (figure 2.4) as $2/(\sqrt{3}s^2)$ and the term $\frac{\partial c}{\partial \vec{x}^\perp} d\gamma$ is approximated by $(c_i - c_0)/\sqrt{3}$. Taking this all together we arrive at the approximation for

$$\nabla \cdot (n\nabla c) \approx \frac{1}{\sqrt{3}\Delta s^2} \sum_{i=1}^6 (n_{i+1} + n_i)(c_i - c_0) \quad (2.26)$$

where it is understood that the index i is taken as $i \pmod{6}$. The time derivatives are approximated by finite differences using a Runge-Kutta 4th order scheme, see for example (Iserles, 2009). Since this is an explicit method the time step is limited by the size of the grid discretization $\Delta t \leq \frac{K}{\Delta s^2}$, where K is

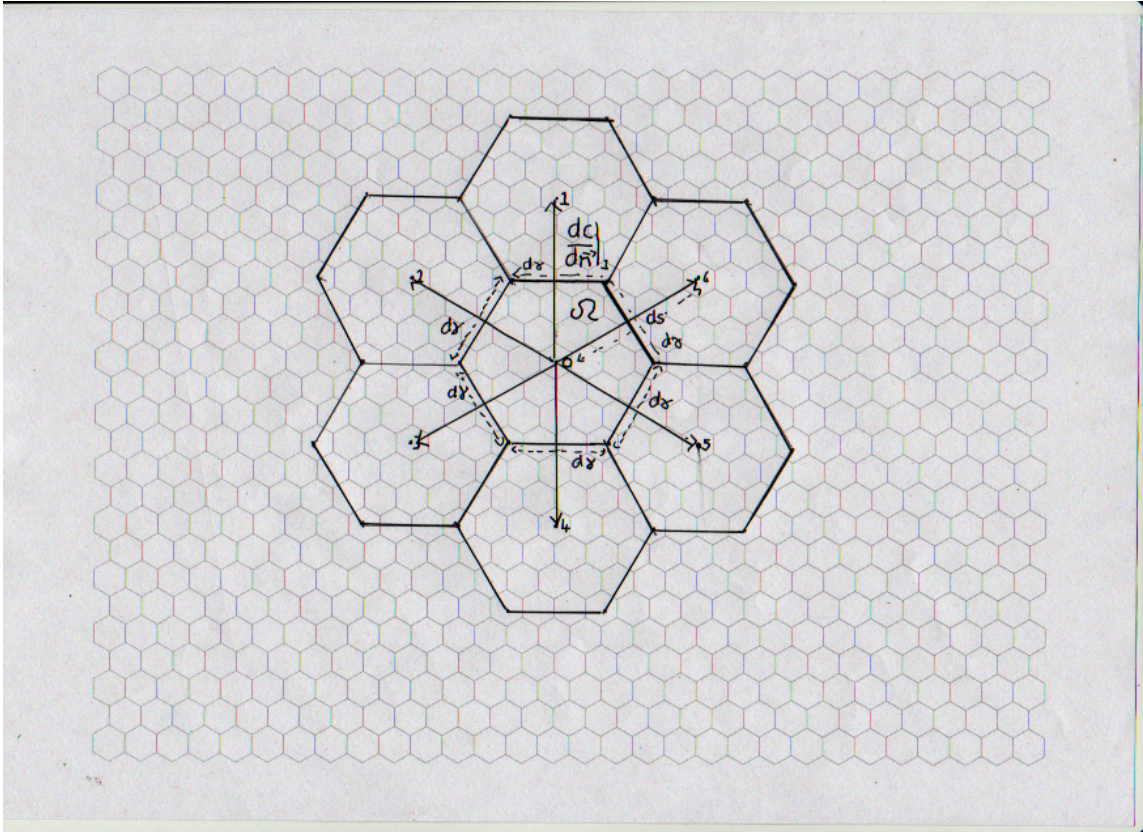


Figure 2.4. Geometry of the finite volume method. The central hexagon with centre point 0 is surrounded by six equidistant neighbours 1-6. Also shown are the normal derivatives $\frac{\partial c}{\partial \bar{n}}$, (written $\frac{\partial c}{\partial \bar{x}^\perp}$ in the text) the boundary elements $d\gamma$ and the area of the hexagon Ω . See text for further details.

some constant given by the structure of the terms. To deal with the no flux boundary conditions, if any of the hexagons in figure 2.4 have their centres outside the boundary of the barrel then we give them same value of c, n as the value of the central hexagon. In this way the normal derivative $\frac{\partial c}{\partial \bar{n}}$ will be zero and no flux can cross this boundary.

2.4 Influence of domain shape on pattern formation

If the shapes of the domains in which pattern formation occurs have a causal effect on the patterns, as for example by the form of the boundary conditions, then we can consider if the structure of the shape affects the patterns. One very important property of a shape is the symmetry group which leaves

the shape invariant. We have considered solutions governed by the circle group S^1 but we shall also consider solving in domains where the boundary is a polygon. For regular polygons, their symmetry groups are finite groups.

An equilateral triangle has symmetry group D_3 which is made up of combinations of rotations by $2\pi/3$ and reflections in a perpendicular bisector M . This gives a group whose size $|D_3| = 6$. The elements of the group are I, R, R^2, M, MR, RM where I is the identity transformation that leaves the triangle unchanged and the other elements are obtained from the generators R, M by group multiplication. By a similar analysis it can be seen that the square is invariant under the symmetry group D_4 which has $|D_4| = 8$ and elements $I, R, R^2, R^3, M, MR^2, D, DR^2$ where the generators are R , rotation by $\pi/2$, M is reflection in the perpendicular bisector of opposite sides and D is reflection in a diagonal.

These symmetries only apply for regular polygons where all the sides are equal. If we relax this constraint on triangles and squares and allow one side to be a different length from the other in the triangle and the pairs of opposite sides to be equal in the square we get an isosceles triangle and a rectangle respectively. The symmetry groups are now reduced, for the isosceles triangle we have I, M and for the rectangle I, M, M', R where the reflections are about the bisectors of opposite sides and R is rotation by π .

We can further relax the constraint so that all sides become unequal and then the symmetry groups of irregular triangles and rectangles is then reduced to I . This analysis can be carried out for other polygons, the groups of the regular polygons D_5, D_6, \dots reducing to I for the irregular versions.

As well as the properties of individual shapes we can look at collective properties when they fit together or tessellate. This is important in biology because constraints of space often require such fitting. If shapes can be fitted together to cover the whole plane this is called a tessellation. If the tessellation is produced from a single shape it is monotessellation. We can cover the planes with monotessellations of regular polygons of sides 3, 4, 6 but not 5. If the shapes are irregular we can cover the plane with a single type of shape.

However tessellations can be formed in other ways. If there is competition for space, e.g. in animal territories in ecology, or cells in packed tissues then a form of tessellation called a Voronoi tessellation

can be formed. In this the regions are created around seed points so that for a given region p and a collection of seed points C the Voronoi region assigned to p is defined as consisting of all points x_p for which $\|x_p - p\| < \|x_p - q\|, q \in C, q \neq p$. This only applies to points inside the region, points on the boundary are equidistant from two different seed points, p, q and the boundary edge can be labelled by this pair pq .

The structure of Voronoi tessellations depends on the spatial distribution of their seed points. Some of the tessellations of regular polygons are Voronoi tessellations where the seed points have the regularity of the shapes. If they are spaced regularly and at distances apart equal to the centre-to-centre distance of the regular shapes then tessellations of regular triangles and hexagons are Voronoi tessellations but tessellations of squares are not. We can also distribute the points randomly in which case we obtain random Voronoi tessellations.

2.5 Metrics to evaluate the effects of domain shape

The angular and radial structure of patterns in regular shapes can be evaluated with reference to the symmetries of the shape which can be precisely defined. With irregular shapes no such mathematical definition of symmetry is available. To evaluate the research questions in this work we need to develop metrics which can be applied to the fields produced by numerical simulation in collections of irregular shapes but which can allow comparisons with the known theory of linear instabilities. To effect on the patterns is examined extensively in chapter 3. For the purposes of the research presented in later chapters we require 4 metrics. Firstly we need to measure the angular and radial structure so that the solutions can be compared with those derived from the linear theory, in particular the Bessel modes. If we examine the linearised equation (2.2) we can see that it is symmetric with respect to the transition $N \rightarrow -N, C \rightarrow -C$. Concentrations of neurons cannot be negative but N, C are the perturbations from a spatially homogeneous state, so the symmetries express that solutions can be inverted like a photographic negative. As the perturbations grow symmetry this symmetry leads to solutions where most of the region is above or below the homogeneous value, physically we can regard these as representing

solutions where most of the region is full of neurons or most of it is empty. We call this metric *occupancy*. Finally, visual inspection of the patterns seems to indicate that there is some fitting of the patterns across the edges, either continuity or else where the sign of the pattern is reversed across the edge. We define a fourth metric, *correlation* to measure if this is a real effect or a product of the human tendency to preferentially focus on patterns in visual input.

These four metrics were defined as follows. The first metric is angular complexity A_c of a scalar field $\nu(r, \theta)$ over a domain $D \subset R^2$. We express the field in polar coordinates, the centre of this coordinate system is the centroid of the domain D . In terms of (2.1), ν could be n or c , generally in this work it is n but the spatial structure of the two fields are the same, so this is merely for convenience and does not affect the value of A_c . Informally, we derive A_c by averaging $\nu(r, \theta)$ over a number M of angular sectors of an annulus which is inside the domain D . This is easy to do when D is circular, when it is polygonal, and especially if the polygon is irregular, the annulus has to be within the maximal circle which can be inscribed within the polygon. The procedure can be defined formally as follows

1. Define a vector $F : M \rightarrow R^2$, where N the set $\mathbb{I} \pmod{M}$, by $F(i) = \frac{\int_{r_0}^{r_1} \int_{\theta_i}^{\theta_{i+1}} \nu d\theta dr}{\int_{r_0}^{r_1} \int_{\theta_i}^{\theta_{i+1}} d\theta dr}$
2. $A_c = C(F(i))/2, i \in \mathbb{I} \pmod{M}$, where C is a function applied to $F(i)$ to count the number of "discretized extrema" of $F(i)$.
3. A "discretized extremum" is defined as a value i , such that $(F(i+1) - F(i))(F(i) - F(i-1)) \leq 0$

Here \mathbb{I} is the field of the integers factored by modulo M because the angular coordinate θ is periodic. Thus a requirement that $A_c \in I$ provides a parity check on the method.

The pseudocode for procedure (1) is given in algorithm 1.

For procedure 3 we use algorithm 2.

The second metric, radial complexity R_c is defined as for A_c and uses the same algorithms but without the use of modular arithmetic since the radial component in polar coordinates is not periodic. The actual code for algorithm 1 is given in `region.h` and that for algorithm 2 is given in `analysis.h` on the Github site which is given in section 1.11 of the Introduction.

Algorithm 1 To produce a vector indexed by angular sector of a field n over a domain D

```

1: procedure SECTORIZE( $M, r_0, r_1, n, D$ )    ▷  $M$ : number of sectors,  $r_0$ : start radius,  $r_1$ : end radius
2:    $\theta_+ \leftarrow 2\pi/M$                     ▷ Angular width of the sector
3:   for  $i \leftarrow 0, M - 1$  do              ▷ Loop over sectors
4:      $V \leftarrow 0$                           ▷ Area of sector
5:      $S \leftarrow 0$                           ▷ Sum of  $n$  over sector
6:      $\theta_s \leftarrow i \times \theta_+$       ▷ Start of sector
7:      $\theta_e \leftarrow (i + 1) \times \theta_+$  ▷ End of sector
8:     for  $h \in D$  do                        ▷  $h$  is an index over  $D$ 
9:       if  $r_0 < r(h) \leq r_1$  then        ▷  $r(h)$  is the radial coordinate at index  $h$ 
10:        if  $\theta_s < \theta(h) \leq \theta_e$  then ▷  $\theta(h)$  is the angular coordinate at index  $h$ 
11:           $V \leftarrow V + 1$ 
12:           $S \leftarrow S + n(h)$             ▷  $n(h)$  is the field value at index  $h$ 
13:        end if
14:      end if
15:    end for
16:     $F(i) \leftarrow S/V$                     ▷ Construct vector  $F(i)$  to hold average of  $n(h)$  in sector  $i$ 
17:  end for
18:  return  $F$                                 ▷ Return  $F$  indexed by sector
19: end procedure

```

Algorithm 2 To find the extremum values of a vector

```

1: procedure FINDEXTREMA( $v$ )                ▷  $v$  is a vector derived from the previous procedure
2:    $s_o \leftarrow 0$                           ▷ Slope before vector index
3:    $s_n \leftarrow 0$                           ▷ Slope after vector index
4:    $s_o \leftarrow v[1] - v[0]$                 ▷ starting slope
5:    $M \leftarrow |v|$                           ▷  $M$  is set to length of  $v$ 
6:    $c \leftarrow 0$                               ▷ counter set to zero
7:   for  $i \leftarrow 1, M - 1$  do
8:      $s_n \leftarrow v[i \bmod M] - v[(i - 1) \bmod M]$ 
9:     if  $s_n s_o < 0$  then                  ▷ Extremum detected
10:       $c \leftarrow c + 1$ 
11:    end if
12:     $s_o \leftarrow s_n$                     ▷ Update slope before moving to next index
13:  end for
14:  return  $c$                                 ▷ Return number of extrema encountered
15: end procedure

```

The third metric is occupancy O_c . This measures the degree of non-homogeneity of the distribution of the field. It is defined as

$$O_c = \frac{S^+}{S^0} \quad (2.27)$$

where S^+ is the area where the field values are above the mean value of the field across the whole region. S^0 is the total area of the region. We do not give pseudocode for determining O_c because the mathematical definition is simple and the coding is likewise.

The fourth metric is correlation P_c and measures the degree to which patterns that are in neighbouring regions on a tessellation are correlated.

$$P_c(\vec{x}_1, \vec{x}_2) = \frac{\vec{x}_1 \cdot \vec{x}_2}{\|\vec{x}_1\| \|\vec{x}_2\|} \quad (2.28)$$

where \vec{x}_1 and \vec{x}_2 are vectors that represent the patterns across two different edges. The numerator is the dot product of these vectors and the denominator is the product of their Euclidean norms. P_c varies between $-1, +1$ for perfect anti-correlation or correlation respectively. The use of P_c is discussed in depth in chapter 4.

The choice of P_c requires some discussion. In comparing patterns in a tessellation we could take properties that applied across the domain as a whole, such as the Fourier spectra of the pattern. Since each region is adjacent to several others it would be difficult to evaluate the causality of any pattern alignment. However each edge in the tessellation connects to just two regions. By representing the field values just inside the boundary as a vector, we can normalise the vectors so they are all of unit norm. All of edge pattern vectors are then on a hypersphere and there is a considerable body of work on statistical distributions on hyperspheres, e.g. (Anderson, 2009). This theory is utilised in the analysis of chapter 4.

Chapter 3

Cortical domain size alone cannot explain within-domain patterning

3.1 Introduction

The rodent primary somatosensory cortex contains structures, described as barrels, which reproduce the pattern of the animals whiskers on the contralateral side (Welker and Woolsey, 1974). The structure of these barrels varies between species, and in particular they vary with the size of the animal's brain. In animals with small brains, e.g. mouse, the barrels are very clearly defined and are hollow with the stomata of the neurons almost exclusively in the walls. Larger animals, such as rabbits also have a structured map from the whiskers to the cortex, but the barrels lack clear sides and hollows (Woolsey et al., 1975). Intermediate between these two cases, the larger barrels of the rat posteromedial barrel subfield (PMBSF) have an interior that does have stomata in the interior. The smaller barrels of the rat anterolateral barrel subfield (ALBSF) are like those of the mouse. Land and Erickson 2005 analysed the interior patterns of the stomata in the rat PMBSF revealed by CO staining. These patterns divided the barrel into smaller regions which they named "subbarrel domains". They also observed that they all conformed to one of four stereotyped patterns. In the mouse the interior of the barrel provides a region

where the projections of the cortical neurons can make contact with processes from thalamocortical (TC) neurons since the processes of the cortical neurons are observed to be facing into the hollow of the barrel, which provides maximal connection with the TC axon terminals. The cortical dendrites have a maximal length of $100 \mu\text{m}$. In barrels with a diameter greater than this, the barrel interior will no longer maximally sample the TC axonal projections. Land and Erickson proposed the interesting hypothesis that by dividing into subdomains each subdomain is within this limit, and maximal coverage of the TC axons is preserved. If too great a cortical area is devoted to an individual whisker then there is no longer any advantage to the hollow barrel structures. Thus the rat PMBSF barrels are a bridging case between this two types of organisation. (Louderback et al., 2006) showed that the subbarrel domains were rich in the neurotransmitter VGLUT2 and the VGLUT2-rich domains coincided with the subbarrel domains revealed by CO staining. Thus the domains were areas where synaptic connections were very active, thereby strengthening the original hypothesis that the function of the subbarrels was to connect to the TC axons.

In the top panel of figure 3.1 we show those four basic patterns revealed by CO staining of a section of the PMBSF of a rat barrel cortex. (Ermentrout et al., 2009) proposed a dynamical mechanism for subbarrel pattern formation that was also driven by size and provided a complement to the functional explanation of (Land and Erickson, 2005). They drew attention to the similarity of these patterns to the lower order Bessel functions that represent the eigenfunctions of the Laplacian operator in a circular domain. The requirement for the patterns to fit into a circular domain of a given size, for example to meet no flux boundary conditions, leads to the prediction that as the size of the domain increases patterns of increasing complexity will be selected. Bessel functions can be classified by their angular and radial complexity, i.e. the number of extrema encountered going in: 1. an angular direction around the circle, 2. in the radial direction from the centre to the boundary, see e.g. (Abramowitz and Stegun, 1970) chapter 9. The Bessel mode is a number pair (A_c, R_c) with A_c angular and R_c radial complexity. In the lower panel of figure 3.1 this theory, which is common to many different forms of pattern forming equations is shown. In circular geometry the Laplacian can be separated into radial and angular components, and if the equations can be linearised so that the Laplacian is the only term with spatial derivatives the partial differential equations

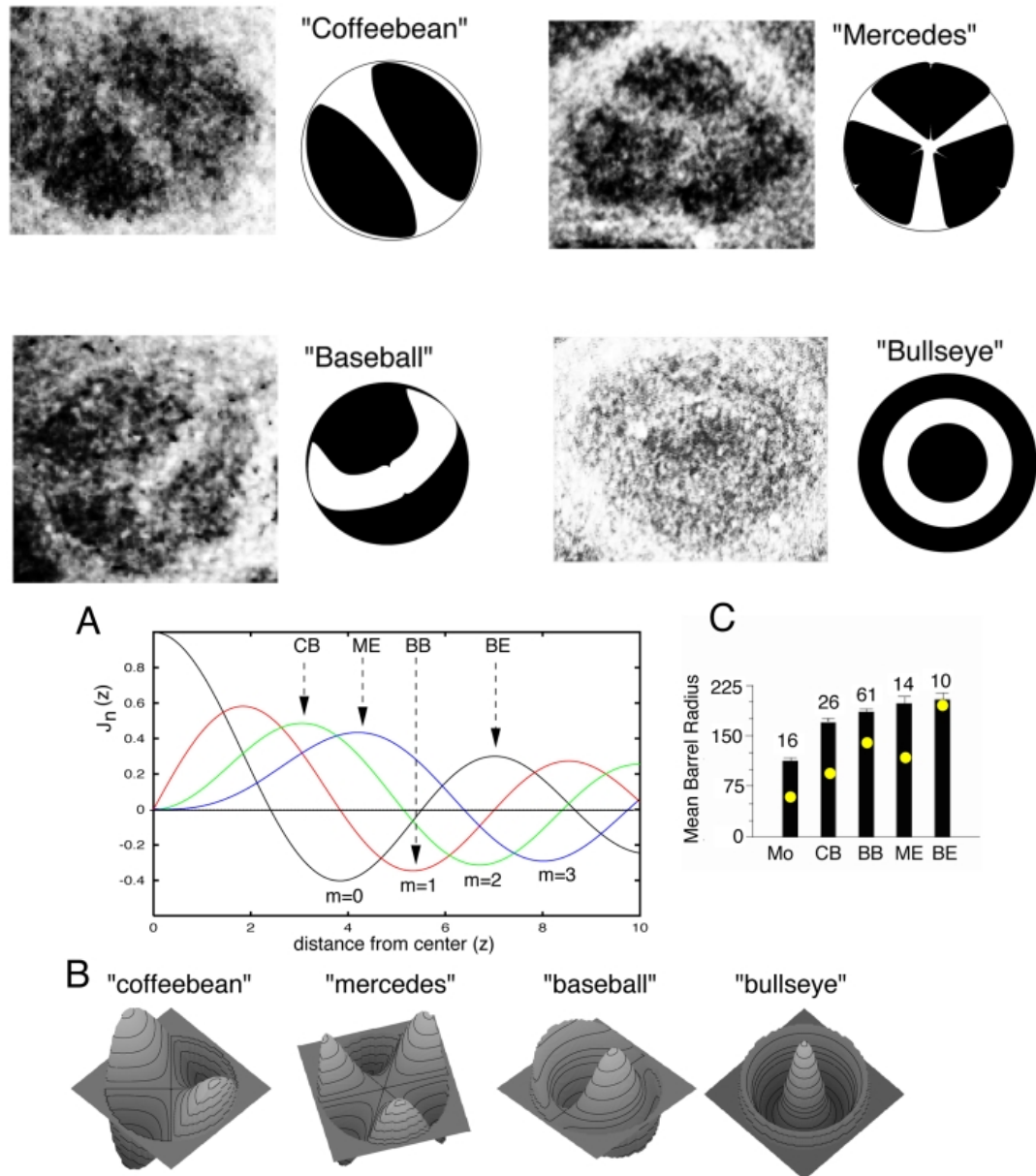


Figure 3.1. The four patterns observed in the PMBSF area of the rat barrel cortex. Top panel: CO stains of four barrels showing each of the patterns with a cartoon of the pattern shown beside it. Bottom panel: an explanation of the patterns in terms of the theory of Bessel functions. Subpanel A. the first four Bessel functions plotted against the radius of the circular domain in which they are embedded. Each function is labelled by its angular mode m which indicates the number of maxima (or minima) of the pattern in the circle. Solutions of pattern forming equations with no-flux boundary conditions on the boundary of the circle must have zero derivative in the radial direction, hence they must be extrema of each of one of the Bessel functions. In subpanel B are shown 3D contour plots of each of the four patterns with Bessel modes (2,1) for coffeebean CB, (3,1) for mercedes Me, (1,2) for baseball BB, (0,2) for bullseye Be. The label (m, n) refers to the angular mode and the number of the extremum along that mode. Thus CB is the first extremum for angular mode 2, Me the first extremum for angular mode 3, BB the second extremum for angular mode 1, Be is the second extremum for angular mode 0. The third subpanel shows bars representing the average barrel radius for all of the barrels observed with that pattern. The yellow dot in each bar shows the barrel radius predicted from the curves in A. The numbers on top of each bar are the number of barrels observed with that particular pattern. Figure reproduced from (Ermentrout et al., 2009)

separate into a set of ordinary differential equations for the radial and angular components (Morse and Feshbach, 1953) Ch. 5. The angular component obeys the harmonic equation whose solutions are the trigonometric functions, the radial component obeys the Bessel equation with one equation for each degree of trigonometrical function, the first four Bessel functions are shown in figure 3.1 subpanel A. By recombining modes $\Theta(\theta)R(r)$ where θ, r are the usual circular polar coordinates, we can obtain solutions shown in subpanel B.

The theory of Bessel functions (Sneddon, 1966) indicates that as size increases the patterns should be selected in the following order.

$$(0, 0) \quad (1, 1) \quad (2, 1) \quad (0, 1) \quad (3, 1) \quad (1, 2) \quad (2, 2) \quad (0, 2)$$

The four patterns identified by (Land and Erickson, 2005) and shown in figure 3.1 belong in this sequence, and it can be seen that this order is the order in which the extrema of the Bessel functions of modes 0-3 are encountered as the radius is increased. . This is a simple and elegant explanation and using results from the theory of bifurcations under constraints of symmetry (Golubitsky and Stewart, 2002), it can be shown that the Bessel functions should appear in the solutions of a wide class of equations that produce patterns via Laplacian operators, ranging from reaction diffusion to Hebbian learning. However this fails to explain the following:

1. The sizes of the host barrels are too close together. According to the theory of Bessel functions the ratio of size between the Coffee Bean and the Bullseye is 1.0:5.1 and from the numerical simulations in the paper the range is 1.0:6.3 However the ratio of the observed sizes of barrels hosting these patterns is 1.0:1.4, this can be seen in figure 3.1 subpanel C. Even allowing for some observational imprecision this gap seems too big.
2. Certain modes are not seen. For example the $(1, 1)$ mode should appear in the smaller barrels of the rat PMBSF and the larger barrels of the ALBSF. It can be seen from subpanel A of figure 3.1 that only four of the possible extrema are selected in the explanation of the patterns, what is different about the others?

3. The Mercedes and the Baseball are in the wrong order according to the Bessel function theory and this is also confirmed in the results of the numerical simulations.

In this paper we show that these three anomalies can be explained by considering the following three factors which are relevant to pattern generation on a tessellation derived from images of the barrel cortex.

1. Occupancy: (Land and Erickson, 2005) report that the bridges that form the patterns occupy only $15 \pm 7 \%$ of the barrels. We show that this means that some modes, in particular $(1, 1)$, would not be observed.
2. Shape: the barrels are of different shape and this allows different patterns to form in barrels of the same area.
3. Multi-stability: nonlinear terms in the models allow different solutions to appear even in domains of the same shape and size according to small variations in initial conditions. This again can explain a spread of patterns within a narrow range of host domain sizes.

In addition we aim to try to explain the frequency distribution of the observed modes shown in figure 3.1 subpanel C from the properties of the tessellation.

Our approach is to analyse the behaviour of the solutions to the pattern-forming equations used in (Ermentrout et al., 2009) using metrics described in chapter 2. These can enable the above issues to be evaluated without the need for visual inspection and subjective interpretation of the patterns. We use these metrics to develop the statistical distribution of various solutions over a range of parameter values so that they can be compared to the known observational results. We then discuss the significance of these results and how far they might be generalised outside the modelling framework used in the original papers and in our work also.

3.2 Results

3.2.1 Observational and simulation data

In table 3.1 we summarise the previous results we address. The first column shows the five basic types identified from the papers previously discussed. In the second column is shown the predicted ratios of circle areas (with the barrels represented by circles). These ratios are derived from the length values at which the Bessel modes representing the patterns have extrema and thus “fit” the circle. The extrema values are taken from the tables in (Abramowitz and Stegun, 1970) and are then squared to give the area ratios. The third column comes from the D_n values of previous simulations, which we confirm in section 3.2.2 below. In the fourth column are shown the mean sizes of the barrels in which the patterns are actually observed. The fifth column shows the relative frequency of the patterns observed.

In (Land and Erickson, 2005) the process by which the patterns were identified is described. The patterns were recorded from 114 barrels taken from 40 complete or partial PMBSF barrel subfields. Only those where staining showed a heterogeneous barrel domain and which could be identified as belonging to a particular row and arc were recorded and analysed. This was 25% of the total observed. Thus the 114 forming the basis of the analysis are a highly selected sample.

The problem is very clear: both from the Bessel function theory and the simulation results the size ratios of the domains in which the patterns are predicted to be observed are much more widely spaced than the actual observations. This cannot be put down to incomplete simulation modelling because the Bessel function theory is clear, patterns are selected as they fit into the region (no-flux boundary conditions produce a hard constraint here). The differing patterns could not all meet this constraint in the very narrow range of areas observed. It is also an issue that so many BB patterns are observed relative to Mercedes pattern given that the areas of the domains they fit are very close together. Following (Ermentrout et al., 2009) we use the following equations to generate the patterns on a planar surface

$$\begin{aligned} \frac{\partial n(\mathbf{x}, t)}{\partial t} &= 1 - n(\mathbf{x}, t) + D_n \nabla^2 n(\mathbf{x}, t) - \chi \nabla \cdot (n(\mathbf{x}, t) \nabla c(\mathbf{x}, t)) + \eta(\mathbf{x}, t) \\ \frac{\partial c(\mathbf{x}, t)}{\partial t} &= f(n(\mathbf{x}, t)) - c(\mathbf{x}, t) + D_c \nabla^2 c(\mathbf{x}, t) \end{aligned} \quad (3.1)$$

Type	Theory	Sim	Obs	Freq
Mo	1.00	1.00	1.00	13%
CB	2.97	2.00	1.22	26%
Me	6.25	4.30	1.63	14%
BB	8.67	6.00	1.49	48%
Be	15.1	12.5	1.70	8%

Table 3.1. The ratios of the sizes of the barrels predicted or observed to fit the patterns 1 Mo, 2 CB, 3 Me, 4 BB, 5 Be. The second column shows the ratio of areas predicted from Bessel function theory, third column shows the ratio of results from simulation with the D_n at which each pattern appears taken as a proxy for area. The fourth column shows the average size of the barrels in which each pattern is observed in the real barrel cortex. The fifth column shows the frequency of each observed pattern. All ratios are relative to the Mo barrels which have no pattern. For the simulation column the ratios were relative to the value of D_n at which the first pattern appeared, thus the simulation ratios are likely to an underestimation of the spread. Data from (Ermentrout et al., 2009)

where n represents the density of the cortical neuronal stomata and c is a attractant for these neurons, D_n and D_c are diffusion constants, and the ‘chemotaxis’ term χ specifies an antidiffusion or concentration term. We use $f(n) = \gamma \frac{n^2}{(1+n^2)}$ with $\gamma = 5$ to represent the production of attractant by the neurons. We augment the original system with $\eta(\mathbf{x}, t)$ as a placeholder for a term coming from outside the system. For most of the calculations we present $\eta = 0$ so the equations are an autonomous system. We use this system as a minimal framework for examining the questions we wish to explore. Since occupancy is an important part of our analysis we require a concentration term which is nonlinear, that can explain why the observed patterns are “narrow”. This is the third term on the RHS of the evolution equation for n , parameterized by χ . If we couple the diffusion terms by $D_n = 0.3 * D_c$, we can use D_n as a proxy for area of the barrels, this can be seen on dimensional grounds, the dimensions of the diffusion constant are L^2/T , where L, T are typical length and time scales. If the time scale is fixed while the length scale can vary then the diffusion constant has $D_n \propto L^2$ and therefore D_n can be a proxy for the area of the domain, provided also that it does not vary across the domain. In the original work these equations were solved on a circular domain where the Bessel functions represent the spatial structure of the the solutions of the linearized equations, they are the eigenfunctions of the Laplacian operator ∇^2 .

3.2.2 Solutions on circular domains

To validate our numerical code we solved on circular domains and using the same choice for the typical length scale and the same no flux boundary conditions as in (Ermentrout et al., 2009). We confirmed that we could produce the 8 solutions up to the (0,2) solution (Be) in the order predicted by Bessel function theory. These solutions are shown in figure 3.2. In solving the nonlinear equations we obtain solutions intermediate to the Bessel modes for parameter values in between the two, so the (0,1) mode (a simple bullseye) becomes elongated along three axes until these perturbations stretch to the edge when it appears as an Me. Also, there is nonlinear mixing of higher modes, so the BB (1,2) also appears with (4,2) in our solution at $D_n = 50$, there is a weaker extra angular variation along with the primary pattern. This can be seen in the figures in then original paper also, for example the BB (1,2) solution there is mixed with (3,2), as secondary angular maxima and minima. These considerations will be important when we consider solutions on less regular domains in a tessellation.

3.2.3 Solving on a tessellation

Here we solve the equations on various types of tessellation, following the observation that the barrels of the rat and mouse cortex closely approximate a Voronoi tessellation, (Senft and Woolsey, 1991), (James et al., 2020). The tessellation provides two key elements of our investigation, the structure of the tessellation gives a spread of barrel areas and shapes which can be derived from observation.

We used three types of tessellation to explore the issues of occupancy, shape and multi stability

1. A uniform tessellation of squares
2. A Voronoi tessellation based on centres that are randomly placed in a unit circle.
3. A Voronoi tessellation based on centres and a boundary measured from an actual image of a rat PMBSF

We show tessellations 2 and 3 in figure 3.3 with the solution patterns for $D_n = 3.007, \chi = 4.723$. As well as solving on the domains of the actual Voronoi tessellation we also solve on domains whose sharp

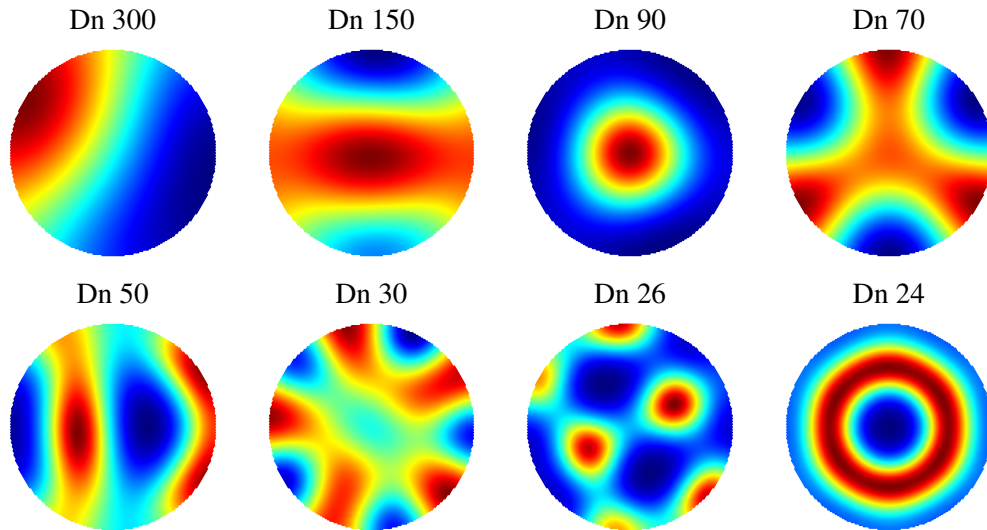


Figure 3.2. Solutions of 3.1 on a circular domain with no-flux boundary conditions. The colour coding is red for the maximum and blue for the minimum of the field normalised separately for each domain. Green is the median value. For all solutions we set $\chi = D_n, D_c = 0.3D_n$ and the values of D_n are 300, 150, 90, 70, 50, 30, 26, 24. All solutions were evolved from random initial conditions. The field shown is n from (3.1). The deviations are of order 10^{-4} of the homogeneous value of $n = 1$, the occupancy O_c , the ratio of the area with values above the mean to the total area is ≈ 0.5 which is characteristic of very weakly nonlinear solutions. For $\chi < D_n$ all nonhomogeneous solutions decay to the homogeneous state. The patterns correspond to the basic Bessel modes discussed in the Introduction, with the addition that the mode at $D_n = 30$ is a mode with higher A_c with mode numbers (5, 2). The patterns observed in the rat barrels are at $D_n = 150$ (CB), $D_n = 70$ (Me), $D_n = 50$ (BB) and $D_n = 24$ (Be). However, on grounds of size alone, if those named patterns are observed it is not clear why the other four are not.

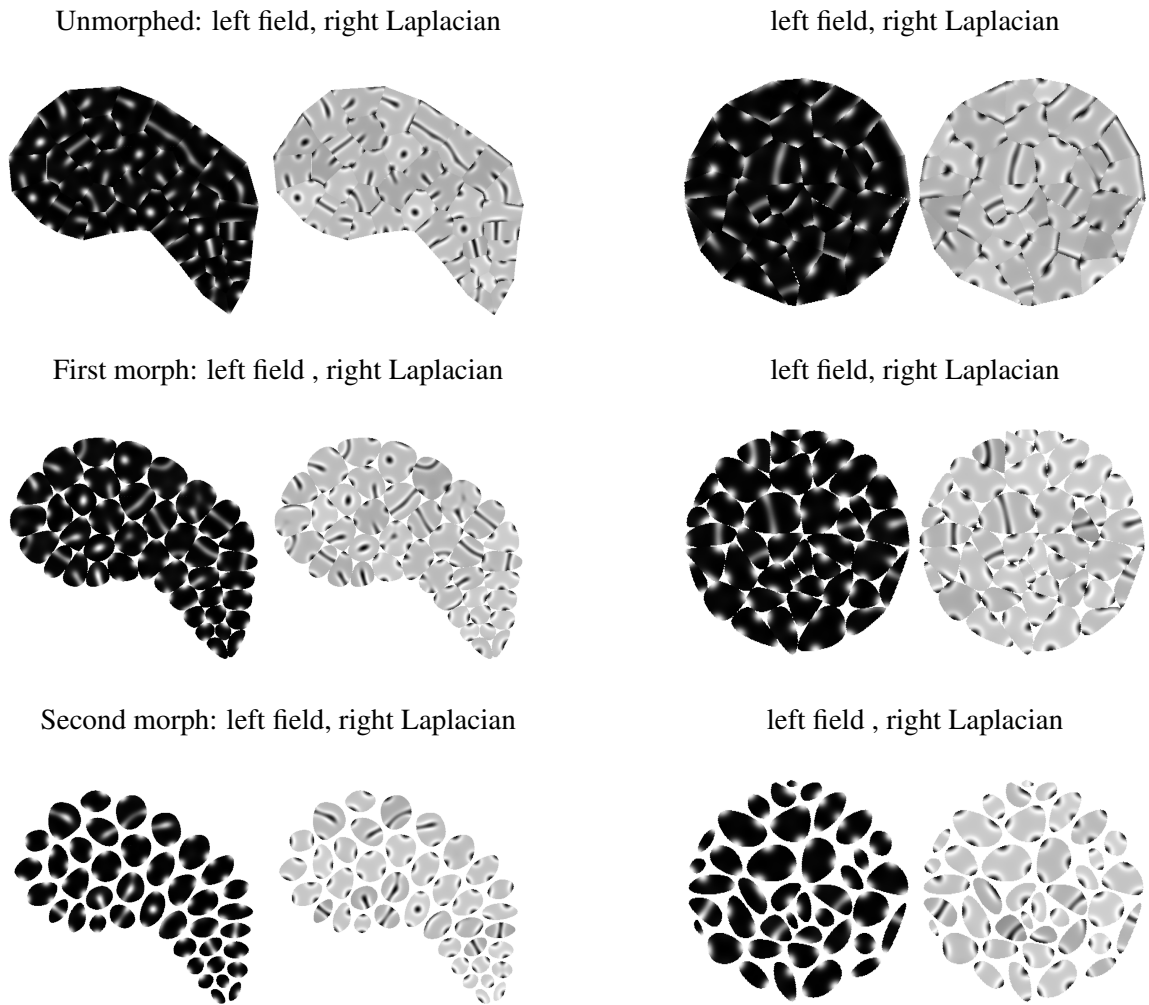


Figure 3.3. Field patterns for a two tessellations, now shown in grayscale to aid comparison with the images shown in figure 3.1. In the leftmost column a Voronoi tessellation based on seedpoints taken from an image of the rat barrel cortex, in the rightmost, a Voronoi tessellation based on seed points distributed randomly within a circle. All patterns were obtained by solving equation (3.1) with $D_n = 3.004$, $\chi = 4.723$. In the left field plot for each tessellation we plot n and in the right $\nabla^2 n$. These are the negative of each other, this configuration comes from the effect of the diffusion and chemotaxis terms in the equations, these are both based on the Laplacian. In the top row are the solutions in the actual Voronoi tessellations, in the middle row the solutions on a tessellation with one level of morphing, in the bottom row one with two levels of morphing. For the morphed solutions the values of D_n , χ , D_c were adjusted by the ratio morphed area divided by the square root of the original area for each domain. Since the diffusion and chemotaxis parameters scale with the inverse of the square root of the domain area, each domain is the same area and pattern differences are due to shape. The patterns for the rat tessellation and the random tessellation appear to be broadly the same.

corners are removed by replacing the corners by Bezier curves that run from midpoint of the edges that form the corner. We can apply this rounding process, which we call morphing, recursively and we also show solutions after 2 applications of morphing. We show these in figure 3.3 below with the solution patterns for $D_n = 4.007, \chi = 4.723$, we explain this figure more fully after considering the parameter sweep shown in figures 3.4, 3.5 and 3.6.

In choosing how to subdivide our tessellations we took the total dimensions of the rat PMBSF image and calculated the average area of the domains. We use all of the domains in our simulations, not just the first four arcs, because we are investigating why patterns are not seen in the smaller barrels, as well as why they do appear in the larger ones. We then ensured that this average size applied to the domains of the square and random Voronoi tessellations. We then conducted parameter sweeps over ranges of D_n and χ from equation (3.1) to examine how the solutions varied with each. As noted above D_n is a proxy for area, but we cannot deduce any meaning to the absolute value since the original scale was chosen arbitrarily. However, as noted in the Introduction, we are interested in the ratio of areas at which different patterns appear and the absolute value of D_n is not necessary for this. We use the four metrics defined in chapter 2 section 2.5 to evaluate the solutions. We checked the procedures for angular complexity, A_c , and radial complexity, R_c , by applying them to the solutions of figure 3.2 where the modes are known from theory. We were able to confirm our measures for all the modes, subject to the caveat that we also pick up higher modes, so that the BB registers as (4, 2) as well as the basic (1, 2) mode. The key point is that we were able to identify this as the first mode where the radial complexity increases from 1 to 2 and we saw this consistently in the higher order radial modes, notably at $D_n = 26$ and $D_n = 24$.

In each of figures 3.4, 3.5 and 3.6 we see 4 plots for parameter sweeps over the three types of tessellation. We vary D_c and χ and keep $D_c = 0.3D_n$. We choose values between where patterns first start to appear (the (1, 1) mode) and going to values where the patterns become of such complexity that they do not represent any of the first seven modes, which are our subject of interest. The D_n values are different from the results in the circle which is taken as the unit circle, since the tessellations represent smaller domains hermetically sealed by the no-flux boundary conditions, bifurcations of patterns will occur at lower values of D_n . χ is scaled in 8 increasing steps as a fraction of D_n , so $\chi = \xi D_n$ where ξ varies

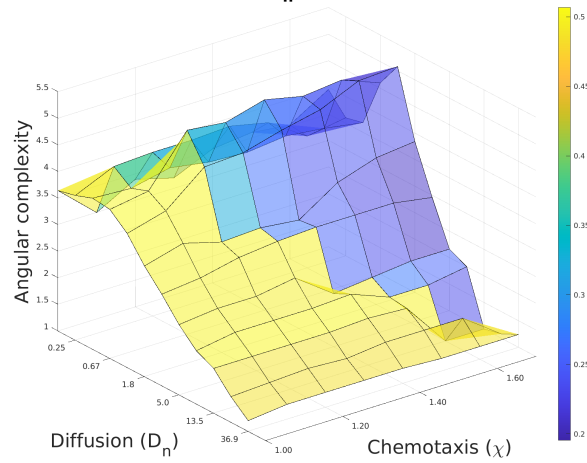
from 1 to 2. It is shown in the original paper that if $\xi < 1$, the pattern-breaking solution decays to zero and we confirmed this numerically.

The plots in figure 3.4 show a surface representing A_c varying with D_n and with χ , overlaid on this is colouring showing occupancy, for the three types of tessellation. We do not show a surface for R_c but it presents qualitatively the same picture. Figure 3.5 shows line plots for A_c and R_c against D_n with separate plots with low and high χ . The first striking observation is that both A_c and R_c increase more or less linearly until we reach $A_c > 3.5$ and with a similar pattern for R_c but at relatively smaller D_n values, although for the square tessellation R_c shows an initial steady value near to 1 then starts to increase. Since the plots are log-linear the expansion along a slanted line represents a power law $A_c = kD_n^\alpha$. This is not what is expected from the linear theory because there should actually be a drop in A_c as we go from Me to BB and a corresponding jump in R_c . It could be that the variation of sizes given by the rat barrel and random Voronoi tessellations could mask this but it does not explain that the uniform square tessellation gives essentially the same result. We can see that this result applies to both low and high χ . Figure 3.6 shows that occupancy remains constant with respect to changes in D_n . There is a drop at the start of the range for high χ but after that constancy is maintained. Solutions with low occupancy are significantly nonlinear. The very weak pattern breaking from the spatially homogeneous case characteristic of the solution where $D_n = \chi$ shows as an occupancy very near to 0.5, the solution is a weak perturbation to the homogeneous case with as many field values above as below the mean. When we approach the observed low value of $O_c < 0.3$, the solutions are far from the spatially homogeneous case and are mostly close to the lower values with only thin patterns showing above the mean. This is a major symmetry breaking from the spatially homogeneous solution. With weak nonlinearity if we look at the patterns with the mean subtracted they occur in pairs, with each pair being the negative of the other (positive values swapped for negative).

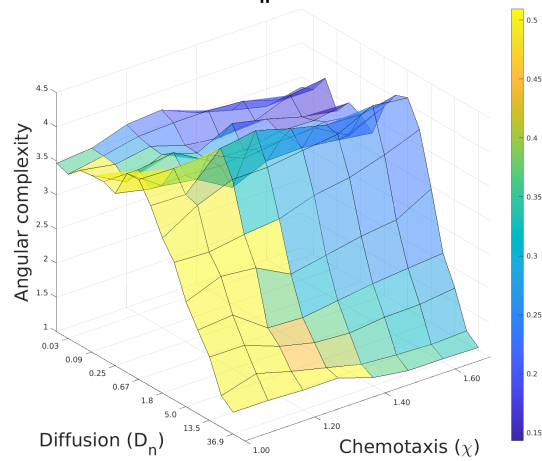
3.2.4 Patterns on a square tessellation

In order to obtain a deeper understanding of the pattern formation process in the strongly nonlinear régime (low O_c) we performed a series of simulation experiments with the patterns on the square tes-

Square tessellation
Angular complexity vs (χ, D_n) , color shows occupancy, M1



Rat PMBSF tessellation
Angular complexity vs (χ, D_n) , color shows occupancy, M1



Random Tessellation
Angular complexity vs (χ, D_n) , color shows occupancy, M1

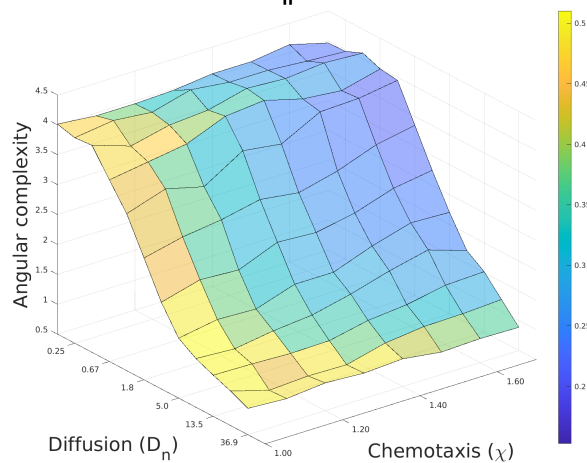


Figure 3.4. Parameter sweeps over the ranges of D_n and χ for the solutions of 3.1 on three different tessellations with 32 different random initial fields for each region of the tessellation. Data points show the average over 32 integrations of angular complexity $\langle A_c \rangle$ against D_n and χ . The surface is coloured with the average values for O_c . Results shown for: top, tessellation of squares, middle, tessellation of rat PMBSF, bottom, random tessellation. All results on tessellations at level 1 of morphing.

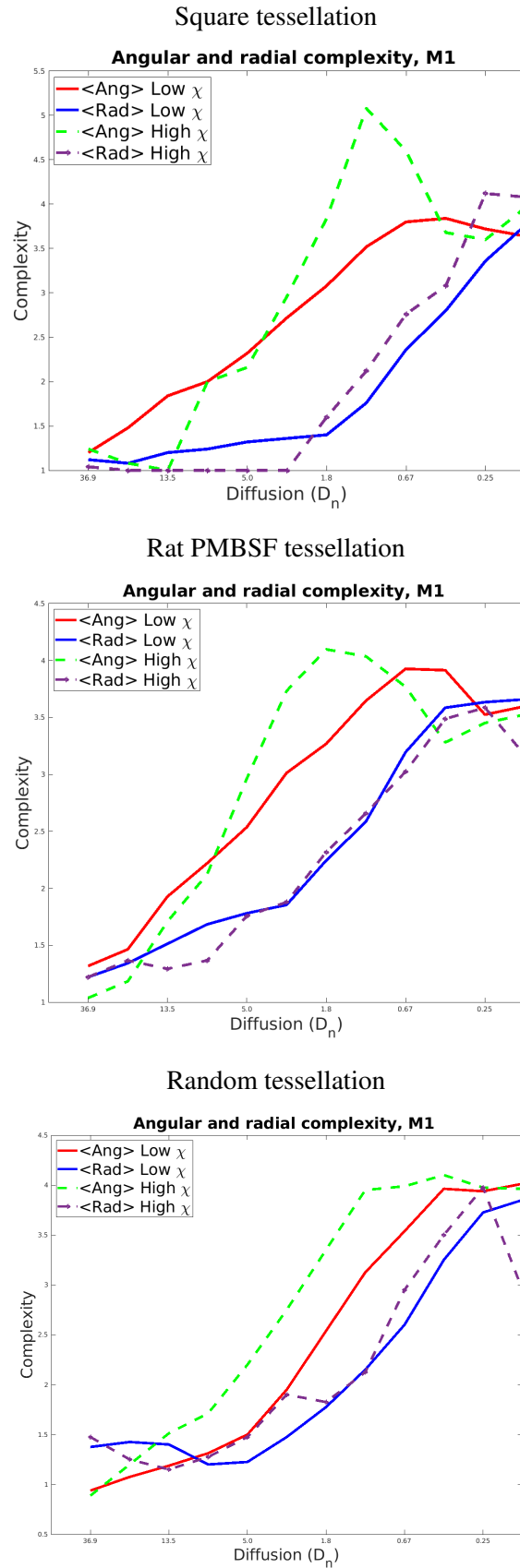


Figure 3.5. Parameter sweeps over the ranges of D_n and χ for the solutions of 3.1 on three different tessellations with 32 different random initial fields.. Red solid and green dotted curves shows averaged angular complexity $\langle A_c \rangle$ against D_n for the lowest and highest values of χ . Blue solid and olive dotted curves show averaged $\langle R_c \rangle$ against D_n for the highest and lowest values of χ . All results on tessellations at level 1 of morphing.

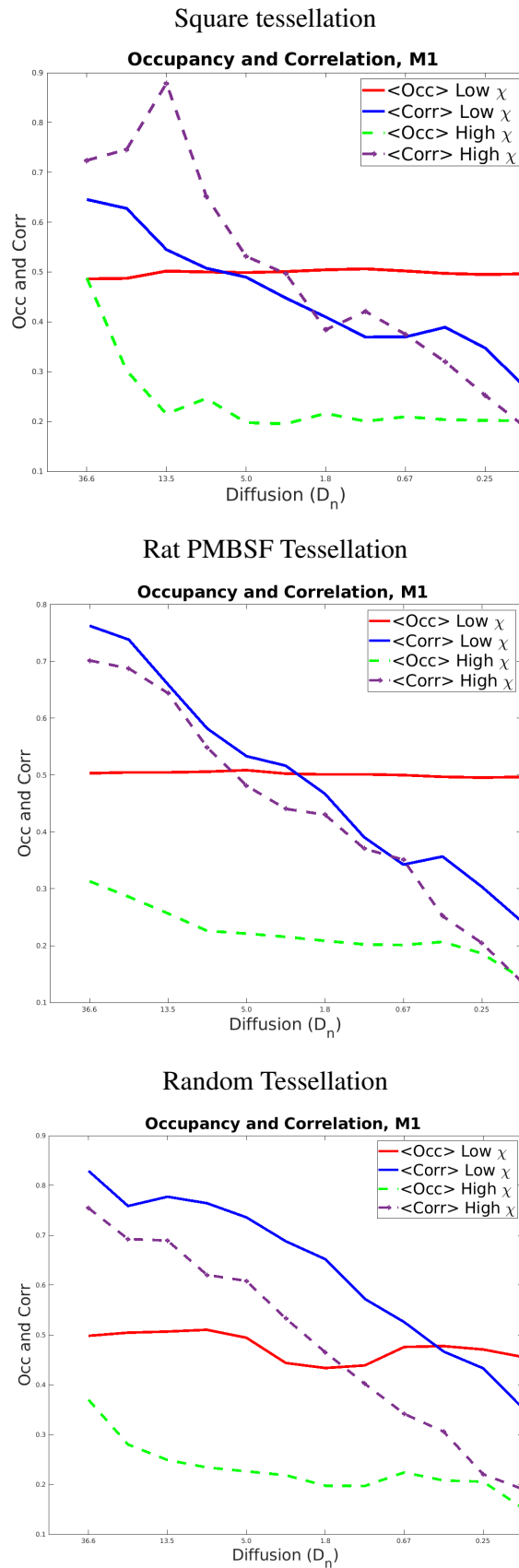


Figure 3.6. Parameter sweeps over the ranges of D_n and χ for the solutions of 3.1 on three different tessellations with 32 different random initial fields for each region of the tessellation. Red solid and green dotted curves show averaged occupancy $\langle O_c \rangle$ against D_n for the highest and lowest values of χ . Blue solid and olive dotted show averaged correlation $\langle P_c \rangle$ against D_n for high and low values of χ . All results on tessellations at level 1 of morphing.

sellation. Here the domains are all the same size and shape, so predictions from the weakly nonlinear theory would predict that all of the patterns would be the same, though they might have different orientations. We looked for parameter values where $O_c < 0.25$ and the patterns were centred around the region between the BB and Me, since this is the centre of the distribution in the reported results. The parameter values were $Dn = 2.0$, $\chi = 3.3$, $Dc = 0.9$, and the boundary conditions were no-flux.

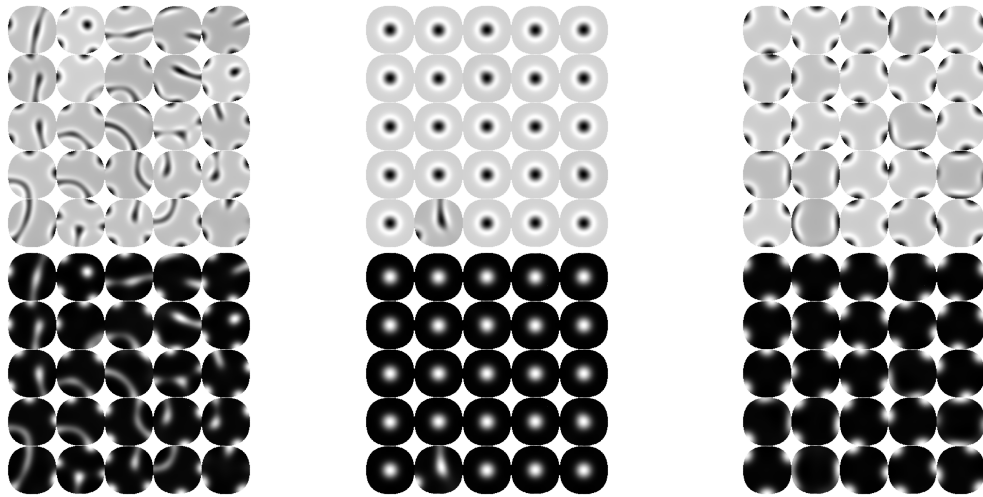
We ran three simulations with different initial conditions. In simulation 1 we seeded each region with a field of form $k \exp -r^2 + \eta(r, \theta)$ where r, θ are polar coordinates relative to the centroid of each region, $\eta(r, \theta)$ is a random variable drawn from a uniform distribution on the range $[0,1]$. The field is thus a mixture of purely random values and a Gaussian centred on the origin. By varying k we can control the strength of this signal. In these experiments we fixed $k = 1$. In simulation 2 we used the same initial conditions with the exception that we used an exponential function to set the initial field on the boundary to be zero. In simulation 3 we also used an exponential but this time the field went to the values of the spatially homogeneous solution $n = 1, c = 2.5$ at the boundary. Thus the field was constant but not zero at the boundary. The results are shown in figure 3.7

The results are remarkable, the final fields are completely different in each case. The initial conditions are of critical importance, in the strongly nonlinear régime the system has memory. Even if the parameters and the size of the regions are the same, very different patterns can appear according to the initial conditions.

3.2.5 Properties of solutions on the rat cortex tessellation

Table 3.1 shows the known data on subbarrel patterns in the rat barrel cortex. We examine in more detail the fields produced by integrating (3.1) at the optimal parameter values we found for reproducing the observational data, this was $Dn = 3.0, \chi = 4.7$. Examining the evolution of the fields at all three of the morphing levels we observed that with χ set to give $O_c \leq 0.25$ we could observe two main classes of solutions: those where the patterns were confined to the walls of the domain (Type 1) and those where thin bridges or circular blobs could be seen within the barrel (Type 2). To understand the difference

Laplacian uniformly random Laplacian zero at boundary Laplacian constant on boundary



Field uniformly random

Field zero at boundary

Field constant on boundary

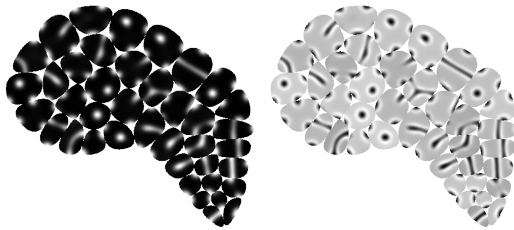
Figure 3.7. Three numerical simulations to test the effect of different initial conditions, shown left to right. All solutions evolve on square tessellations subject to one degree of morphing. On the bottom of each plot is shown the field values for n , at the top the Laplacian of n . They are the negative of each other showing that in regions where the field is high and positive the Laplacian is high and negative. The patterns for each are the same which is a mark of a converged solution, in the time varying evolution towards the time steady solutions this is not the case. Left panel: initial conditions allow the field to vary right up to the boundary in both radial and angular directions, middle panel: initial field is constrained by a exponential to go to zero at the boundary, right panel: initial field is constrained to go to the constant values that represent the spatially homogeneous solution. It can be seen that the patterns in the left and right columns are different in each subdomain, though they are grouped into a small number of classes with the individual patterns of each class being related by rotations. The patterns in the centre are all the same (with one exception) they show a simple bullseye pattern which is invariant under rotation. Only the patterns in the left column can be related to the four patterns of figure 3.1, several examples of the BB pattern can be seen. In the right hand column the patterns all have $A_c = 3$ the same as Me, but they are confined to the boundary and so would not be observed.

between these we examine the Me image in figure 3.2. The above mean red regions are connected with the centre, the three below mean regions are disconnected. However an equally valid solution would have a connected blue region and three disconnected red ones. Now we can imagine what happens as $O_c \rightarrow 0$. The first case will tend towards a Type 2 solution (three thin rays connecting the centre), the second solution will tend towards three small red blobs on the boundary with the central region blue, a Type 1 solution.

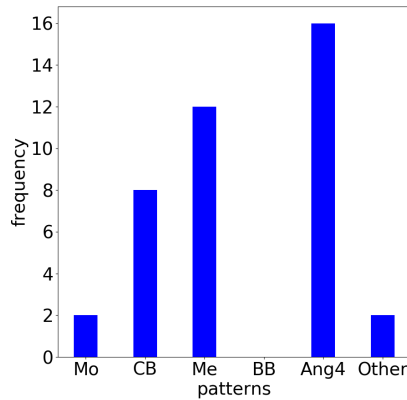
Both types of solution can be seen in figure 3.8 where we have switched to grayscale to assist comparison with the patterns in figure 3.1. With equations 3.1 and $\eta = 0$ we observed that the Type 2 solutions were just as common as the Type 1 in the early stages of the solution but as the solution evolves the thin “bridges” retract to the boundaries and become solutions of Type 1. We then set $\eta = ge^{-kr^2}$ to model a central signal coming from outside the region which will attract neuron growth. The hypothesis was that this can stabilise the Type 2 patterns. We found by numerical experimentation that setting $g = 0.1, k = 1.0$ gives a signal that affects but does not swamp the fields (e.g the fields become a Gaussian bump with no angular structure). Comparing the two final solutions in figure 3.8 we can see the effects of this stabilisation, there are approximately equal numbers of Type 1 and Type 2 solutions in the eventual solutions with η as prescribed. We also show bar plots of the A_c, R_c types of the solution. We grouped the solutions into 6 classes: M_0 with $A_c \leq 1, R_c \leq 1$, CB with $A_c = 2, R_c = 1$, Me with $A_c = 3, R_c > 0$, BB with $A_c = 1, R_c > 0$, $Ang4$ with $A_c = 4, R_c > 0$, and used $Other$ for patterns not caught by this classification. The justification for these names and ranges is presented in Methods below. Note that any Type 2 solutions that lose some of their extensions from the centre can resemble the definition of a CB , namely to divide the region into two unequal parts. This process can also lead to a single ray from the centre to the periphery, examples of both of these can be seen in figure 3.8.

In all of these integrations on the rat tessellation we have not seen any Be patterns. To encourage patterns with $A_c = 0$ we set $n = 0, c = 0$ on the boundary as the initial condition by multiplying the field by e^{-Su^2} where u is the distance of the hexes in the grid from the boundary. In the tests on the square tessellation this produced single bullseyes, see figure 3.7. In figure 3.9 we show the fields at timesteps 1.5×10^4 and 7.0×10^4 for $D_n = 1.82, \chi = 2.86$ on the first level of morphing, this being a region where

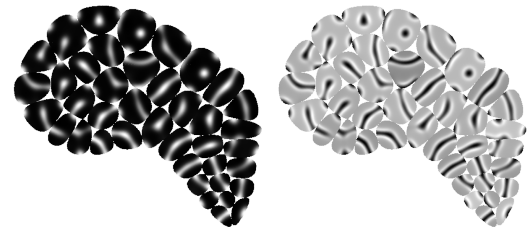
$\eta = 0$, left: field, right: Laplacian



$\eta = 0$ pattern frequency



$\eta = 0.1e^{-r^2}$, left: field, right: Laplacian



$\eta = 0.1e^{-r^2}$ pattern frequency

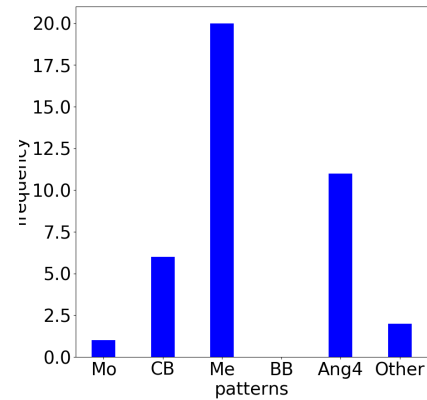


Figure 3.8. The final fields generated by the solutions of equation 3.1 at parameters $D_n = 3.0, \chi = 4.7, D_c = 0.3D_n$. The parameters were chosen to give the best fit to the observations, in terms of patterns and occupancy $O_c = 0.26$. In the left column are shown the fields and frequency plots for the solutions with $\eta = 0$, the right column shows the solutions for $\eta = 0.1 \exp -r^2$. The definition of Mo, CB, Me and BB are given in the text, these are designed to match the four patterns of figure 3.1 however some of the patterns with a given A_c, R_c only appear as blobs on the boundary, others with the same complexity appear as bridges to the centre. The class *Ang4* is any pattern with $A_c = 4$, all other patterns are recorded *other*. See Materials and Methods for further explanation. Comparing the left and the right plots and histograms it can be seen that the central signal allows more patterns to project to the centre, however not all the possible rays do so. Thus most of the patterns have the Me angular complexity of 3 but have "lost" one or more of their rays and so can appear as BB or CB by visual inspection.

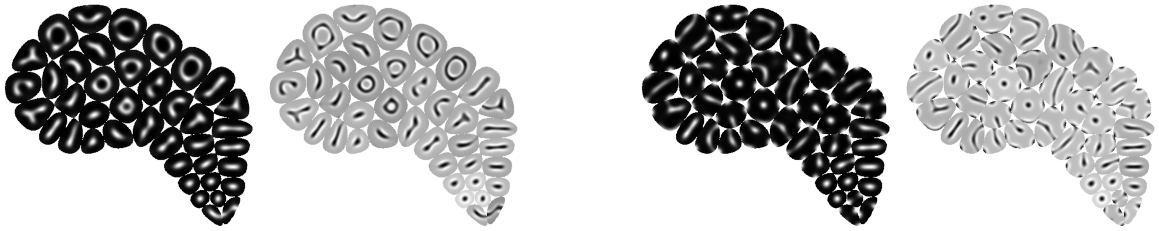


Figure 3.9. Solutions of equation 3.1 at parameters $D_n = 1.82, \chi = 2.86, D_c = 0.3D_n$ on a rat tessellation with the first level of morphing. The fields were set to zero at the boundary by a exponential function. On the left we show the fields after 1.5×10^4 timesteps and several Be type solutions can be seen. On the right we show the solutions after 7.0×10^4 time steps and it can be seen that all the Be solutions have disappeared but several examples of the simpler (0,1) bullseye can be seen. At these parameter values the solutions converge by 2×10^5 timesteps, in the sense that no further change in the fields can be detected in the plots

we might expect Be patterns. It can be seen that in the early plot several subregions have Be patterns but these have disappeared in the later plot. For these parameters solutions convene to the extent that no visible change can be seen in the field by 2.0×10^5 timesteps, thus by a third of the time to convergence the Be patterns have become unstable. It can be seen that there are many examples of the simpler (0,1) bullseye pattern.

We now compare our results with those in (Land and Erickson, 2005), (Ermentrout et al., 2009) by adopting exactly the same procedure for counting patterns. This is described in the former paper as "We studied every barrel in which 1) CO staining appeared to be nonuniform and 2) there was sufficient context that the barrel could be identified as belonging to a particular row and arc. We excluded barrels that were indistinct ...or barrels that consisted of a single CO domain." We produced our simulation data by running ten simulations based on the same tessellation as shown in figure 3.8 but with different initial conditions for each run. The distributions for each run were different, the patterns in each barrel were different on each run. This confirms the sensitive dependence on initial conditions. We did this for integrations of (3.1) firstly with $\eta = 0$ which we call "No Signal" and secondly with $\eta = 0.1e^{-r^2}$ which we call "Signal". For the No Signal results 68 out of 200 results fitted the criteria for being counted. In the rest there was a single domain, either because the pattern had retreated to the walls or because

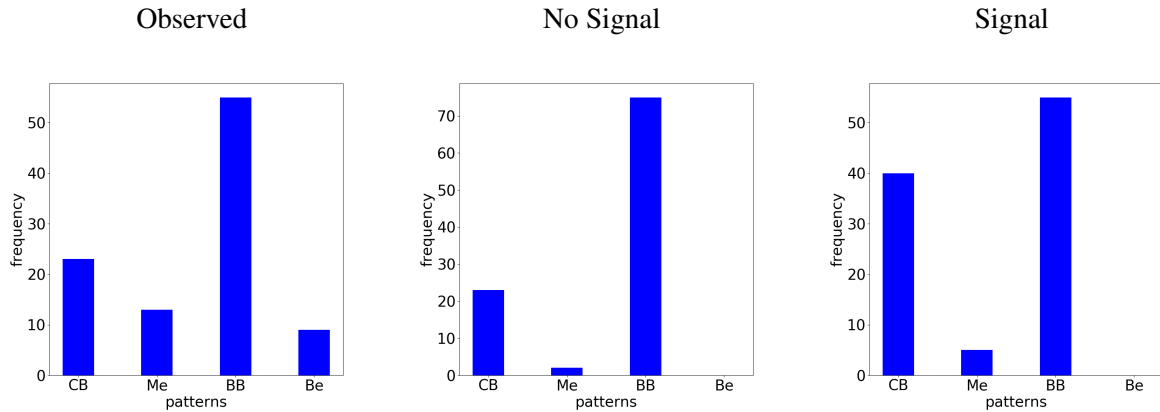


Figure 3.10. Comparison of the distribution of patterns obtained from integrating equation 3.1 at parameters $D_n = 3.0$, $\chi = 4.7$, $D_c = 0.3D_n$ with the experimental results of (Land and Erickson, 2005), (Ermentrout et al., 2009). The results from the simulations were counted by exactly the same procedure as described in those papers. In the left column is shown the frequency plots for the simulations with $\eta = 0$ called the No Signal results, the middle column simulation results for $\eta = 0.1e^{-r^2}$, called the Signal results. The right column shows the experimental results. The horizontal axis shows the four patterns CB, Me, BB, Be in the order of appearance with increasing barrel size as predicted by linear theory. It can be seen that with No Signal the BB pattern dominates. There are very few Me and no Be. With a signal a higher frequency of CB appears and the frequency of Me is increased but no Be. The signal pattern appears closest to the experimental results in terms of the increasing frequency of Me. We confirmed the observation in the experimental papers it is hard to classify between slightly curved BB and CB. The low frequency of Me and the non appearance of Be provide a possible hint that the dynamics of the interaction with the subcortical regions may be important in altering the dynamics occurring purely within the barrel.

only a single ray connected the spur to the centre. For the Signal results 136 out of 200 results fitted the criteria illustrating the role of the signal in stabilising the rays from the centre to the walls. As in the original papers we only counted from rows A-E and arcs 1-4. They do not report if subbarrel patterns were seen in any of the other barrels in the PMBSF, rows C-E arcs 5-9 so we excluded any patterns seen in these. The original papers state that only 25% of the barrels examined fitted the criteria but we have no breakdown of how much of this was due to indistinctness and how much that there was no subbarrel pattern. Their total sample was 113 barrels from 40 complete or partial barrel fields.

The frequencies of the four patterns are shown in figure 3.10.

3.3 Discussion

The major subject of investigation in this paper is to determine the limits of the explanatory power of the hypothesis that patterns observed in the tessellation of the rat cortex can be explained as eigenfunctions of the Laplacian operator in domains of finite size. Implicit in this is the prediction that the primary explanatory parameter for producing different patterns is the size of the domain. We have identified three problems with this hypothesis in the Introduction and now address each in turn to discuss how the results of section 3.2 can provide insight and pointers for their solution.

The observed sizes of the host barrels are too close together. Referring to table 3.1, the ratio between the mean sizes of barrels showing the mouse Mo absence of pattern and the most complex pattern Be is 1:1.7. According to Bessel function and simulation results the ratios should be 1:15 and 1:12.5 respectively. Now if we take the ratio of the largest to the smallest barrel from the tessellation of the rat cortex shown in Figures 3.3 and 3.8 we find a ratio of 1:6. If we restrict to the barrels in arcs 0-4 and rows A-E we get a size ratio of 1:3. This latter is large enough for both CB, Me, and BB patterns to appear in these barrels, we would expect the patterns to appear in subregions of the appropriate size. In (Land and Erickson, 2005) Figure 6 B and C are shown the distributions of the patterns in rows A-E (6b) and arcs 1-4. There is a definite trend across the rows, the dominant mode in A is CB a and the dominant mode in E is BB, results in the other rows are more complex but broadly fit this trend. However there is also a comparable distribution in size between the barrels in different arcs and the differences in the distribution of patterns between arcs seem to reverse the size prediction. Arc 1 barrels overall are larger than those of arc 4, but the frequency of CB is half that of BB in arc 1 but only 1 : 7 in arc4. Moreover the barrels in E5, E6 and E7 are comparable in size to barrels in arc A so they should patterns also, but no patterns are reported outside of rows A to E.

Certain modes are not seen. The parameter sweeps shown in figures 3.4, 3.5, 3.6 show a wide region of parameter space where both A_c and R_c increase. This is particular marked in the rat and random tessellations, where over a wide range the increase in A_c follows a power law. The results for R_c are similar but show a kink as the solutions leave the $R_c = 1$ basic value. This is very pronounced in the

results of the square tessellations. Indeed one would expect this for A_c results also. However the results of figure 3.7 show that the patterns are very sensitive to initial conditions. A square has a D_4 symmetry group with 8 symmetries. Thus a CB may align along diagonals at the same parameter value that an Me can align to the midpoints of the sides, achieving a more nearly equal length scale. The radial complexity R_c may have less flexibility in this respect. Given the spread of areas in the rat tessellation (1 : 8) and random tessellation, if the Be mode is seen all the 8 modes that come before it in terms of the radius at which an extremum of the radial component of the Laplacian operator occurs on the boundary.

We can explain some of this by examining figure 3.6. The occupancy O_c is constant across a wide range of D_n values. In the contour plots of figure 3.4 it can be seen that the boundary between occupancy where the fraction of the barrel that is occupied compared to unoccupied is equal and an O_c where less than a quarter of the barrel is occupied is sharp. In figure 3.3 we show that there can exist two types of solution for a particular combination of A_c, R_c , when the occupancy is low. We can either have A_c blobs on the boundary, or else A_c rays from the centroid of the region. For the latter, we require $R_c > 1$ since with $R_c = 1$, if there is a maximum at the boundary there will be a minimum at the centre. For a ray we need a maximum of neural density at the centre as well as at the periphery, however we will still have a minimum in between so the ray is likely to break in the middle.

This can explain the results shown in figure 3.8. The field on the left evolved with $\eta = 0$ initially resembles that on the right. However with increasing time the rays break and shrink to the boundary. The minimum in the middle seems to annihilate the maximum at the centre. The ray shrinks to boundary as a blob on the boundary. Given that the septum of the barrel cortex is of variable width it would be very hard to see such boundary oriented solutions, especially when O_c is low. A video on the thesis website, shows several examples of rays shrinking to the boundary. Following this analysis, if a process were to maintain the maximum at the centre the ray could be stabilised. This is what is done in the solutions shown in the right hand column of figure 3.8 by making η a constant signal of chemoattractant c in equations 3.1 by setting η to be a Gaussian blob at the centre of the the subdomain. Low occupancy can explain why the $A_c = 1, R_c = 1$ solution is not seen. With $O_c = 0.5$ it represents solutions where one half of the subdomain is occupied, and one half not. As $O_c \rightarrow 0$ the occupied part shrinks to be a

blob on the wall of the subdomain. Such a mode would be very hard to detect.

The Mercedes and the Baseball are in the wrong order according to Bessel function theory. The definition of BB and Be given in (Land and Erickson, 2005) is that they "... contain a small CO-dark subbarrel that is partially or completely surrounded by a larger one ...". The BB pattern corresponds to partial surround where the subbarrels have part of their boundary as the boundary of the whole barrel. As noted above, solutions with rays from the centre to the boundary are potentially unstable. Thus in Me solutions if one of the rays disappears we will be left with a pattern that fits the BB description. In this interpretation, BB can arise from solutions with three or more rays that have lost rays in the course of their evolution. It can also be seen from figure 3.8 that in some subdomains this process has gone so far as to leave only a single ray, which of course cannot subdivide the subdomain into two regions. Such patterns have not been reported from images of the rat cortex, however they can be seen clearly in the subdomain patterns on a giraffe's skin (see figure 4.1b in chapter 4).

The above analysis can explain most of the observations shown in Table 3.1. The dominance of BB patterns arises from the fragility of Type 2 solutions when O_c is low (< 0.25). On this reasoning many of the BB patterns are patterns with $A_c \geq 3$ which have been subject to symmetry breaking secondary bifurcations that cause some of the rays to shrink to the boundary. However it cannot explain that Be $(0, 2)$ solutions are observed but $(0, 1)$ solutions are not. In figure 3.9 we show that Be solutions for initial conditions where the field drops to zero on the boundary via an exponential function, but these Be solutions are not stable. (Land and Erickson, 2005) propose that the patterns are an expression of some process that keeps the size of the subregions similar to those of a mouse barrel. The $(0, 2)$ solution can do this at low occupancy but the $(0, 1)$ solution would need a centre that went a considerable way to the periphery and this would violate the low occupancy requirement. We note the considerable effect that a simple signal based on a Gaussian bump at the centre has on the solutions (c.f figure 3.8) which is a very simplistic modelling of interaction with the axons projecting from the thalamus, so it is possible that more realistic modelling of this interaction could explain the observation of relatively infrequent Be modes.

We also compared our results with those reported in (Land and Erickson, 2005) by using exactly the same procedure described there. Since a very similar number and distribution were reported in (Ermentrout et al., 2009) we assume that the same procedure was followed there. We present our results for the No Signal and Signal versions of (3.1) and present them together with the original results in figure 3.10. We can reproduce the result that the overwhelmingly predominant modes are the CB and BB. As remarked by the original authors it can be difficult to distinguish these, the main distinguishing mark of the BB pattern is that it is curved and divides the region into two unequal areas. However without quantifying these two features it is a matter of subjective judgement into which class a pattern forms. In terms of the other two patterns, with the No Signal solutions the percentage of Me was 1% and with the signal this increased to 5%. No Be were seen in the simulations, therefore combined percentage of the CB and BB was 99% and 95% respectively. In the observational results they accounted for 79% of the total with Me accounting for 13% and Be for 8%. The explanation for this preponderance of CB and BB suggested by our results is in terms of stability rather than barrel size. At the parameter values of these results more modes and modes of greater angular complexity are excited but they are Type 1 solutions that are only visible on the boundary. Given the thickness and irregularity of the septa they would be difficult to detect.

Type 2 solutions are unstable to a perturbation where one or more of the rays showing their angular structure become unstable and shrink to the boundary. This seems to be a consequence of the low occupancy reported, of $15 \pm 7\%$. It can be seen that rays that go from the boundary to the centre will occupy a greater percentage of the barrel than those that are small protrusions on the boundary. Thus as the angular complexity increases, to keep within the occupancy limit requires that the rays become thinner and thus more liable to this ray shrinking instability. Evidence for this is that giving a central source of chemoattractant c in the n equation gives a greater percentage of Me. It also gives a greater number of patterns away from the boundaries, for No Signal 132 out of 200 barrels show Type 1 solutions, for Signal 64 out of 200 are Type 1, thus the majority are Type 2. We might ask why BB are more numerous than CB. Looking at the plots it can be seen that a relatively short curve near to the boundary and starting and ending at points that subtend an angle much less than π at centroid, whereas

the CB must pass through the centre and so will be longer in general than BB.

Thus we can explain a considerable amount of the observations with our dynamical model that takes account of low occupancy. We can also see that even a very simple signal outside of the model confined to the barrel can produce a major effect on the solutions. This leaves open the possibility that a more sophisticated modelling of the interaction between neuron formation within the barrel and the axonal projections coming from the thalamus, a major task for this model would be to explain the stability of Be solutions. Thus we see that although the model used in the original papers and extended here is too simplistic, if its results are examined in a systematic manner with a clearly defined protocol it can point the way towards extending to models with greater explanatory power. Another important avenue to examine in terms of further experimental observation is to see if it really is the case that subbarrel patterns are only observed in arcs 1 to 4. Both on the arguments of size and stability we should see patterns in other barrels of the PMBSF. Clear confirmation that these do not exist would be very challenging to explain from the models developed here. This could either mean that these models have very little to do with pattern formation in the PMBSF or else that there is something different about the way that arcs 1-4 develop.

There has been very little published on the subbarrel patterns after the initial observation and explanation. It is to be hoped that the investigation presented here shows that understanding their formation can lead to important new observation and theory of barrel formation and of the links between neuronal development in the layers of the cortex and their interaction with the growth and signals coming from subcortical layers.

3.4 Materials and Methods

Solutions to equations (Eq. 3.1) were obtained numerically on a discretized hexagonal lattice of grid points using the finite volume method described by (Lee et al., 2014), and a fourth-order Runge-Kutta solver was used to advance the solutions to a steady state (parameter values were chosen so that all solutions were eventually constant in time, i.e., patterns were stationary). Simulations were written

in C++ with the help of the support library *morphologica* (James and Wilson, 2021) (see also James et al. (2020)). We verified that all simulation results reported were insensitive to the choice of spatial discretization (i.e., to the lattice density). For the integrations on a single circular domain a hexagon-to-hexagon distance of 0.016 on a domain whose spatial scale was normalized to be 1.0 was found to be sufficient. For the solutions on the tessellations we decreased the hex-to-hex distance to 0.008 while keeping the length scale to be 1.0. For both single and tessellation runs we performed comparative integrations at twice the resolution. The differences were small and had no effect on the conclusions to be drawn from the results.

No flux boundary conditions were applied at the edges of the domains, for integration on circular domains this was simple. For the results on tessellations we set the no-flux conditions on all boundaries. Some are outer boundaries imposed by the total domain being tessellated, others were internal boundaries derived from the Voronoi tessellation, the no flux boundary conditions were same for all boundaries. The normal gradient of the field was set to zero by a ghost point method, where the values at the centres of the ghost hexagons were set to the value at the centre of the boundary hexagon. This was not done for hexagons adjacent to the central hexagon but on the interior of the boundary. Thus, the *tangential* gradients at the boundary were not constrained. Solutions were considered to have converged when the mean of the absolute differences in field values sampled at intervals of 1000 timesteps fell below $\sim 10^{-10}$. However, for some parameter values, the solutions developed a very small oscillation as they approached convergence. We believe this is a numerical effect and terminated the solutions when this occurred. These oscillations were of the order of 10^{-8} of the mean value of the field.

There are some issues in evaluating the A_c and R_c measures for the shapes in the tessellations. For all shapes, circular or regular or irregular polygons, we evaluated A_c by dividing the shape into a number of sectors each of which subtends an equal angle at the centroid. We calculated the average value of the field in each sector and evaluated the extrema of the resulting 1-dimensional vector. For R_c we evaluated the average values in a series of concentric rings and evaluated the extrema as before. For polygonal domains we evaluated the maximal circumscribed circle and used this to defined the angular and radial sectors. In the outer parts of the sectors this circle will intersect only isolated regions of the polygon but

we determined that with sufficient resolution in terms of number of hexes in the region we can get stable values of A_c, R_c , we tried experimenting with differing numbers of sectors to check that the results were not sensitive to this. There have to be sufficient sectors to resolve the angular and radial complexity, but not so many that the averages in the sectors become subject to fluctuations due to low numbers of hexes in a sector. We found that at the resolutions given above, 24 angular and 12 radial sectors gave stable results. O_c is straightforward to calculate and we have consider the issues in determining P_c in chapter 4.

When we use A_c and R_c to classify the patterns we note the results from section 3.2.2 that nonlinear solutions mix higher modes along with the fundamental patterns, like overtones in the notes produced by musical instruments. We included in the Mo (no pattern) the (1,1) mode since it would appear as an empty subregion as explained above. The CB mode was defined strictly as (2,1). Me was defined as as a mode with $A_c = 3$ and $R_c > 0$ so we included overtones. BB is defined strictly as (1,2), since it was the most common mode we wanted to determine if it was easy to excite in its simplest state. Ang4 were all the modes with $A_c = 4$, these cluster closely around the parameter values where Be is found in the circular domains. The class other was a catch all for all other modes. We consider that A_c, R_c are the fundamental measures in understanding the behaviour of the system 3.1, they are grounded in the theory of the symmetry group of these equations. However, in attempting to evaluate our results against observations classified in stereotypical patterns some form of decisions about classification need to be made. The bullseye solutions are difficult to determine from our methods, since there will be some fluctuation between sectors so that an $A_c = 0$ will not be found via these methods. In this case we broke our rule of automated mode detection and looked for such solutions by visual inspection. In actually determining patterns from observations, it might be better to train neural net classifiers, however this would remove the link to the theory of the symmetries of the solutions and make it more difficult to evaluate models. It would be possible to attempt to determine A_c, R_c from digitised images, e.g. by spectral analysis, but methods for coping with noise would need to be developed.

Chapter 4

Correlated pattern formation in adjacent tessellation domains

4.1 Preamble

This chapter is from a paper (Brooke et al., 2022). Since it is written to be read as a standalone paper some of the previous discussions in this thesis are repeated, as are equations and citations.

4.2 Introduction

Central to current theories of biological organisation is a distinction between constraint and process. A constraint exerts a causal influence on a dynamical process and is not itself influenced by that process, at the spatial or temporal scale at which those dynamics take place. This definition permits a description of biological function in terms of constraint closure, i.e., the reciprocal interaction of constraints between processes operating at different timescales (Montévil and Mossio, 2015; Montévil et al., 2016; Mossio et al., 2016) (see also (Maturana and Varela, 1980; Wilson and Prescott, 2021)). A step towards falsifying such high-level descriptions of biological organisation is to formulate predictions at the level of specific biological systems, in which those predictions may be tested directly. To this end, our objective here is

to operationalize the definition of constraint as causal influence on dynamical process.

The distinction between constraint and process is made explicit in the reaction-diffusion modelling framework (Turing, 1952), which has been successful in accounting for a wide range of biological (and other) phenomena, from the growth of teeth to the spread of tumors and the healing of skin (Murray, 1984,9). Reaction-diffusion models describe biological pattern formation in terms of local interactions amongst molecules or cells, which collectively amplify specific modes in an initially random distribution, with those modes determined by the relative size and shape of an enclosing boundary. Hence, the boundary shape is a constraint on the processes of short-range excitation and long-range inhibition from which pattern emerges.

Observing pattern contained by shape therefore suggests that the shape constrained pattern formation. But, alternatively, the enclosing shape may have emerged subsequently to, simultaneously with, or independently of, the formation of the pattern, and it is not obvious how to discriminate between these possibilities. One approach to establishing a causal influence of the boundary on the pattern is by *synthesis*. If the observed shape is imposed as a boundary condition for a reaction-diffusion model, and the evolution of that model gives rise to a similar pattern in simulation, we might infer a causal influence of the shape on the pattern. While compelling and important, such evidence is indirect, as computational modelling is limited to establishing existence proofs for the plausibility of hypotheses, rather than testing them directly. We seek therefore a complementary approach by *analysis* of the pattern, i.e., a direct means of testing between the hypothesis that the shape causally influenced the pattern and the null hypothesis.

To analyse an individual pattern in these terms, one could look for an alignment between the pattern and the boundary shape. For example, incrementing the diffusion constants from an initial choice that amplifies modes of the lowest spatial frequency will, on an elliptical domain, typically produce a sequence of patterns that is first aligned to the longer axis, and subsequently to the shorter axis. Indeed, for a well-defined boundary shape and a simple reaction-diffusion system generating a low spatial-frequency pattern, the alignment of an observed pattern to a hypothetical boundary constraint may be compared

with a set of eigenfunctions derived from the linearized equations (i.e., using Mathieu functions for an elliptical domain; (Abramowitz and Stegun, 1970)). But such methods break down for more complex boundary shapes, for higher-mode solutions, and for reaction-diffusion dynamics described by increasingly non-linear coupling terms.

In search of a more practical and robust method, the possibility we explore here is to exploit the fact that the shapes of adjacent biological domains are often related to one-another. That is, the processes that determine the shapes of adjacent domain boundaries may themselves be subject to common constraints, or indeed serve as constraints on one-another. Consider the following concrete example. In the plane tangential to the surface of the rodent cortex, the boundary shapes of large cellular aggregates called ‘barrels’ form a Voronoi tessellation across the primary somatosensory area (Senft and Woolsey, 1991) (see Fig. 4.1). The barrel boundaries are apparent from birth, and from the eighth postnatal day develop ‘subbarrel’ patterns reflecting variations in thalamocortical innervation density (Louderback et al., 2006) (Fig. 4.1). A reaction-diffusion model, specifically the Keller-Segel formalism with its additional non-linear chemotaxis term, has been used to successfully recreate subbarrel structure in simulation, as well as to explain an observed relationship between the size of the enclosing barrel boundary and the characteristic mode of the subbarrel pattern ((Ermentrout et al., 2009); see also (Keller and Segel, 1971)). A synthetic approach has also helped establish that the barrel boundary shapes could emerge to form a Voronoi tessellation based on reaction-diffusion dynamics constrained by the action of orthogonal gene expression gradients on the processes by which thalamocortical axons compete for cortical territory (James et al., 2020). Hence in this system, the barrel boundary shapes that constrain subbarrel pattern formation via reaction-diffusion are thought also to be related by the common (genetic) constraints under which those barrel boundary shapes emerge.

Within such systems, the geometrical relationship between the shapes of adjacent domain boundaries might be expected to align the patterns that form within those boundaries to a degree that is reflected by the correlation between patterns in either domain. Hence measuring the degree of correlation between adjacent patterns could serve as a proxy for the degree of alignment to the boundary, and thus form the basis of a robust test for the hypothesis that shape constrained pattern formation.

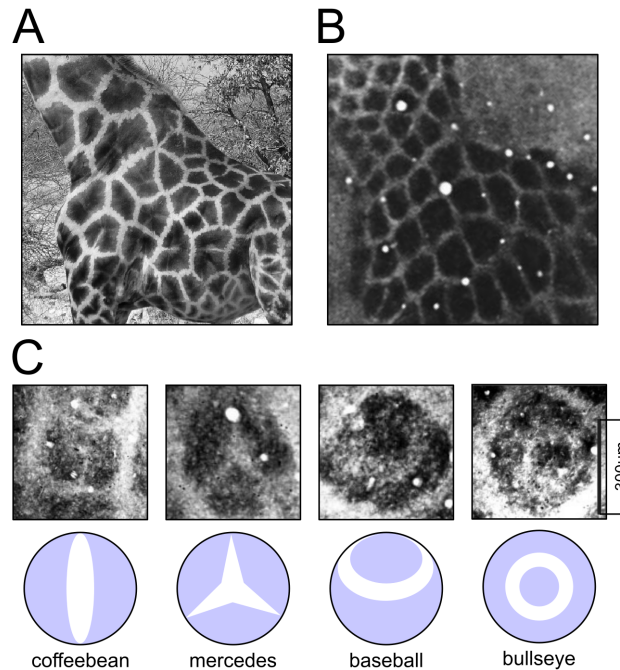


Figure 4.1. *Tessellating domains and sub-domain structure in biological systems.* At markedly different length scales, the skin of giraffes and the stained neocortices of rodents display similar arrangements of polygonal domains, many of which appear further divided into sub-structures. **A** Image of the skin of a giraffe (*Giraffa camelopardalis reticulata*), credited to O. Berger, and described by Koch & Meinhardt (1994; Koch and Meinhardt (1994)) as a Voronoi tessellation. The dark panels overlap with a vascular structure that is important for thermoregulation. **B** Image of a tangential section of the cytochrome oxidase stained primary somatosensory cortex of an adult laboratory rat (*Sprague-Dawley*), revealing a pattern of large cortical columns known as ‘barrels’, which have also been described formally as a Voronoi tessellation. **C** Sub-structures apparent in larger barrel columns have been described in terms of the four categories depicted below, which correspond to the stable patterns generated by a reaction-diffusion model parameterised to amplify modes of increasing spatial frequency. Images in **B** and **C** are from Land & Erickson (2005; Land and Erickson (2005)) and are shown at a common scale.

Given chemical, mechanical, and other physical sources of spatial coupling in biological systems, it seems unlikely that pattern formation ever occurs completely independently in proximal and adjacent biological domains. But, in principle, how much of a relationship between patterns that form within adjacent domains might we expect to observe under the assumption that no communication occurs across domain boundaries?

On face value, this question might seem misguided. If pattern formation amongst cells within a particular domain occurs without the direct exchange of information with cells of an adjacent domain, then

on what basis should we expect to measure any relationship at all between the patterns that form within adjacent domains? As we will show, strong correlations between patterns that self-organize independently in adjacent domains are in fact to be expected, if the shapes of those domains are geometrically related. Specifically, correlations are to be expected if the boundaries of adjacent domains abut, such that the domain shapes constitute a tessellation. Simulation experiments and analyses reported herein are designed to establish how relationships between domains on the basis of their shapes and common boundary lengths contribute to this somewhat paradoxical effect.

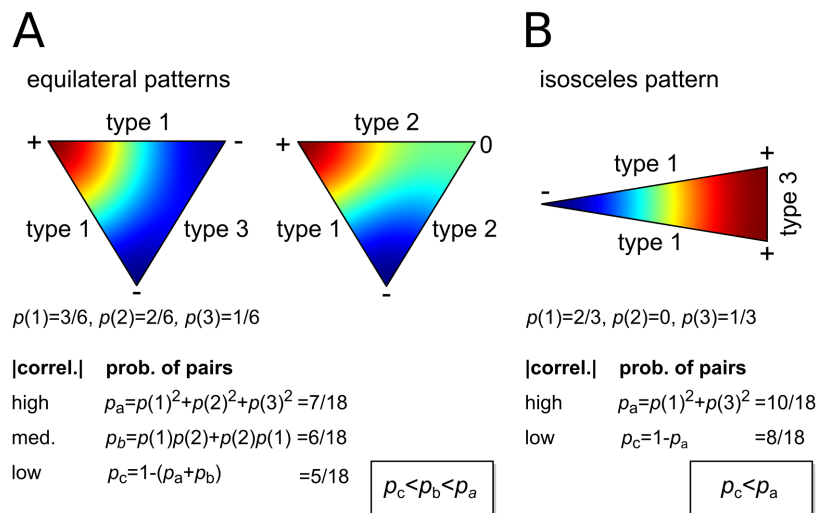


Figure 4.2. The distribution of pattern correlations along common edges of Tessellating triangles should be bimodal. Colour images show typical patterns generated by a reaction-diffusion model with a large diffusivity term, using a colour map in which red and blue mark extreme high and low concentration values, and green marks zero concentration. **A** Solved within the boundary of an equilateral triangle, two basic patterns emerge, with extreme concentrations in one corner and along the opposite edge (left) or at two corners (right). Along the edges, three pattern types are apparent. Type 1 varies between the two extremes, type 2 varies between one extreme and zero, and type 3 does not vary. The probability of type i is given below as $p(i)$. The table gives the probability that the absolute correlation between patterns sampled along two randomly chosen edges will be high (p_a), medium (p_b), or low (p_c). As $p_c < p_b < p_a$ the distribution of correlations should be bimodal. **B** Patterns that emerge within the boundary of an isosceles triangle will be of type 1 or 3 only, changing the distribution of correlations across random edge pairs while retaining an overall bimodal distribution ($p_c < p_a$). However, if pairs of edges are restricted to those which may be adjacent in a tessellation then only pairs of type 1 and pairs of type 3 are possible, and $p_a = 1$. Hence, in more general terms, the distribution of correlations between patterns measured along the edges of adjacent tessellation domains should be even more strongly bimodal.

4.3 Results

The key insight developed here is that patterns that self-organize independently in adjacent domains of a tessellation should nevertheless be correlated. Hence, by analysing the correlations between patterns measured in adjacent domains we can directly test the hypothesis that those observed patterns self-organized under constraints imposed by the borders within which they are observed to be enclosed. We will demonstrate the robustness of the (predicted) correlation effect by examining numerical solutions to reaction-diffusion equations that have been evaluated in domains that tessellate under a range of different geometrical constraints (Fig. 4.3). We will begin with an instructive toy example that will reveal the correlation effect most clearly. We will then show by analysis that the effect holds in a specific biological case (subbarrel patterning).

The patterns on which we will base our analyses can be generated on the two-dimensional plane \mathbf{x} by solving reaction-diffusion equations of the form

$$\begin{aligned}\frac{\partial n(\mathbf{x}, t)}{\partial t} &= 1 - n(\mathbf{x}, t) + D_n \nabla^2 n(\mathbf{x}, t) - \chi \nabla \cdot (n(\mathbf{x}, t) \nabla c(\mathbf{x}, t)) \\ \frac{\partial c(\mathbf{x}, t)}{\partial t} &= f(n(\mathbf{x}, t)) - c(\mathbf{x}, t) + D_c \nabla^2 c(\mathbf{x}, t)\end{aligned}\tag{4.1}$$

where n and c are two interacting species, D_n and D_c are diffusion constants, and the ‘chemotaxis’ term χ specifies the strength of the interaction between the two species. Following (Ermentrout et al., 2009) we will use $f(n) = \gamma \frac{n^2}{(1+n^2)}$ with $\gamma = 5$, and set $D_n \leq \chi$.

4.3.1 Bimodal pattern correlations amongst adjacent domains signal boundary constraints

Consider a reaction-diffusion system (e.g., Eq. 4.1) constrained by a boundary in the shape of an equilateral triangle (Fig. 4.2A). Solved for a choice of diffusion constants that yield patterns with the lowest spatial-frequencies, this system will generate one of two basic kinds of pattern (e.g., in the concentration of n and/or c). In the first, one of the extreme values of the reaction, positive or negative, will collect in one of the three corners of the triangle and values at the other extreme will be spread out across the opposite edge. Along that edge the values are essentially constant, and along the other two edges the

values vary from extreme high to extreme low. In the second kind of pattern, values at the two extremes will collect in two corners and values around zero will collect in the third. Along one edge the values vary from extreme high to extreme low and along the other two they vary from zero to either extreme. Values sampled along the edges will vary between the two extremes in $\frac{3}{6}$ of the edge types (type 1), they will vary from one extreme to zero for $\frac{2}{6}$ of the edge types (type 2), and they will not vary along the edge for $\frac{1}{6}$ of the edge types (type 3). Assuming (for simplicity) that the two kinds of pattern occur equally often, and that pairs of edges are drawn at random from a large enough sample, two of the same edge type will be drawn with a probability that tends toward $p_a \rightarrow \frac{1}{2^2} + \frac{1}{3^2} + \frac{1}{6^2} = \frac{7}{18}$ ('tends to' denoted by \rightarrow). A type 1 and type 2 edge will be paired with a probability of $p_b \rightarrow 2\frac{1}{6} = \frac{6}{18}$. And a type 3 edge will be paired with a type 1 or 2 for the remaining $p_c \rightarrow \frac{5}{18}$. Now consider that along the edge, the magnitude of the correlation between the values sampled will be high for p_a pairs, low for p_c pairs, and intermediate for p_b pairs. Given that $p_c < p_b < p_a$, that the magnitude of each correlation level increases with its probability of occurring, and that correlations and anti-correlations at each level are equiprobable given the symmetries within each kind of pattern, the distribution of correlations should be (overall) bimodal. Note that we describe the distribution as *overall* bimodal because smaller secondary peaks are expected to emerge around each distinct correlation level.

Consider next what happens when we substitute equilateral triangles with isosceles triangles (Fig. 4.2B). Reducing the number of axes of symmetry from three to one further constrains the kinds of patterns that are possible, causing (low spatial-frequency) solutions of the reaction-diffusion system to align with the perpendicular bisector of the base, and reducing the pattern along the edges to two types only. For example, if the base is the shorter side then $\frac{2}{3}$ of the edges will be of type 1 and $\frac{1}{3}$ will be of type 3. Pairs of the same type constitute $p_a \rightarrow \frac{10}{18}$ and pairs of different types constitute $p_c \rightarrow \frac{8}{18}$, so again $p_c < p_a$ and the distribution should again be (overall) bimodal. We note two important differences between the equilateral and isosceles cases. First, as pattern formation is more constrained by the isosceles boundary shape, and so the number of different kinds of patterns that are possible is reduced, the proportion of extreme correlations (and anti-correlations) has increased, from $p_a \rightarrow \frac{6}{18} = 0.333$ to $p_a \rightarrow \frac{10}{18} = 0.556$. Second, the number of secondary peaks in the distribution of correlations has reduced to just two, around

the positive and negative correlations corresponding to p_c .

Because the pattern in each triangle is independent, any equilateral triangle in a tessellation can be substituted or rotated so that a given edge is adjacent to any other. Hence we expect to sample from the same distribution of correlations whether we choose pairs at random, or limit our choices to those edges that are adjacent. This is not the case for the isosceles triangles, which only tessellate by arranging neighbours base-to-base or with the bases' perpendicular bisectors antiparallel. A base cannot be adjacent to a non-base, and hence the distribution of correlations obtained from sampling adjacent pairs will lose its secondary peaks to display only the highest correlations and anti-correlations. So correlations sampled from adjacent rather than randomly selected edge pairs should be even more strongly bimodal.

Further, imagine randomly displacing each vertex of the tessellation of equilateral triangles in order to construct an irregular tessellation of scalene triangles (Fig. 4.3C). As each vertex is common to three triangles, each displacement changes the constraints on pattern formation in three triangles, from an initial minimally constraining configuration, and as such, increases the overall bimodality of the distribution of correlations. The irregular tessellation permits no substitution of domains, and hence, as in the isosceles case, we expect the overall bimodality of the distribution of correlations to be greater when comparing patterns amongst adjacent edges compared to randomly chosen edges.

An overall bimodal distribution of correlations amongst values sampled along pairs of edges from adjacent domains is therefore to be expected for domains that tessellate either regularly or irregularly. This property indicates that the domain boundaries constrained pattern formation. As a final thought experiment, consider that a jigsaw puzzle, i.e., an image into which borders are subsequently cut, will display perfectly strong positive correlations across adjacent edges and no anti-correlations. But our considerations thus far suggest that strong correlations and anti-correlations should be equally likely when the tessellation boundaries constrain subsequent pattern formation. Thus it is really the presence of strong anti-correlations in the distribution that evidences a causal influence of domain shape on pattern formation.

4.3.2 Correlated pattern formation in adjacent domains of naturalistic tessellations

To test our reasoning we solved the reaction-diffusion system defined by Eq. 4.1 numerically, using a dense hexagonal lattice of grid points, in domains with boundary shapes that were either equilateral triangles (Fig. 4.3A), isosceles triangles (Fig. 4.3B), or scalene triangles (Fig. 4.3C), which in each case could be fit together to form a tessellation. Pattern formation was simulated independently in each triangular domain using no-flux boundary conditions ($D_n = \chi = 36$, $D_c = 0.3D_n$), and settled values of n were sampled along the edges of each boundary, one hexagonal grid point in from the edge. Pearson correlation coefficients were then calculated from samples taken either along the edges of domains that were adjacent on the tessellation, or from randomly chosen edge pairs. The distributions of correlation coefficients obtained from random and adjacent edges were compared in each case using a Kolmogorov-Smirnov test (see (Press et al., 2007)). For equilateral triangles this analysis revealed no significant difference, and for isosceles triangles ($p < 0.001$) and scalene triangles ($p < 0.001$) the difference was highly significant, as anticipated.

Considering pattern formation on tessellations of triangles is instructive, but to what extent do the considerations developed here apply to the kinds of tessellation observed in natural systems?

Examples of Voronoi tessellations are commonly found in the natural world (Thompson, 1917; Honda, 1978,9), including the packing of epithelial cells, the patterning of giraffe skins, and modular structures in the functional organization of the neocortex. The domains of a Voronoi tessellation enclose all points that are closer to a given ‘seed point’ than any other. As such, the polygonal structure of the tessellation is completely specified by a collection of seed points, with points along the polygonal boundaries equidistant to two seed points and points at the vertices equidistant from three. To test whether the predicted bimodal correlation is also to be expected in these naturally occurring tessellation structures, we generated random Voronoi tessellations from randomly chosen seed point coordinates, and solved the reaction-diffusion system (independently) within each domain. As shown in Fig. 4.3D, the distribution of correlations sampled from along adjacent edges is again clearly overall bimodal. Hence, the effect is not specific to the case of triangles, and is to be expected for irregular tessellations of polygons that have

a range of different numbers and arrangements of vertices.

The domains that comprise naturally occurring tessellations are often “Dirichletiform” ((Senft and Woolsey, 1991), p. 350), but may not be strictly polygonal, with rounded corners rather than definite angles at the vertices (Gómez-Gálvez et al., 2018). And it is known that patterns formed by reaction-diffusion systems tend to be strongly influenced by the presence of definite angular intersections at the vertices (Jung et al., 2017). Therefore, to establish whether bimodality is also predicted for such natural structures, we re-constructed the random Voronoi tessellation and rounded the corners of the domains by joining the midpoints of each edge with quadratic Bezier curves whose first derivatives fit continuously at the midpoint. We then reconstructed the edges that corresponded to those of the original polygon by recording the points where the radial segments joining the centroid of the original polygon to its vertices cut the new shape. The reaction-diffusion system was solved again on the resulting domains, and (rounded) edges in the same locations as for the analysis of the original (polygonal) tessellation were correlated for a direct comparison. As shown in Fig. 4.3E, the distribution of correlations along adjacent edges is again predicted to be bimodal. Hence, the effect is not specific to polygonal domains and indeed is to be expected in this more general case.

Kolmogorov-Smirnov tests revealed that the distributions of correlations sampled from adjacent versus random edge pairs were not significantly different when Voronoi domains were strictly polygonal or when the domain edges were rounded.

4.3.3 Measuring the effect of boundary constraints on pattern formation and alignment

In order to measure the degree to which the boundaries constrain pattern formation, we consider the known result (see e.g., (Anderson, 2009) Ch. 4) that the scalar products of vectors that are uniformly randomly distributed on a unit hypersphere of dimension $D - 1$ (i.e., embedded in a space of dimension D) follow the beta distribution, $\mu_B(u)$, on $u \in (0, 1)$,

$$\mu_B(u) = \frac{u^{\alpha-1}(1-u)^{\beta-1}}{B}(\alpha, \beta), \quad (4.2)$$

with $\alpha = \beta = (D - 1)/2$, and $B(\alpha, \beta)$ the standard beta function (Abramowitz and Stegun, 1970). It can be seen that the beta distribution diverges at $u = 0$ and at $u = 1$ if $D = 2$, i.e., when the vectors are uniformly distributed on the unit circle, but that it conforms to a uniform distribution for a sphere in 3 dimensions ($D = 3$). Note that these dimensions pertain to the abstract vector space of all normalised edge vectors, and hence the dimension can in principle be as large as the numerical discretization that the tessellation permits. However, the coherence of the vectors derived from the smoothness of the solutions of Eq. 4.1 ensures that they lie in subspaces of much lower dimension. We measured correlations using the Pearson correlation coefficient, which is equivalent to calculating the dot product of two unit vectors, and thus we can use simple algebra to map from the domain $[-1, +1]$ to $[0, 1]$. If the edge vectors are not ‘pinned’ to the tessellation we expect them to be able to ‘slip’ relative to each other so they become uniformly distributed on a circle, and consequently $\alpha \rightarrow 0.5$ (see *Methods* for a proof). Estimates of the corresponding symmetric ($\alpha = \beta$) beta distribution fits are shown with the histograms in Fig. 4.3, where $\alpha < 0.5$, from which we deduce that they are not uniformly distributed, exactly as expected if the influence of the tessellation on pattern formation were to preferentially select certain mutual orientations along adjacent edges. For completeness we note that replacing the coherent fields generated by reaction-diffusion with fields that have random values, and thus no spatial pattern, instead gives a distribution that approaches a normal distribution ($\alpha \rightarrow \infty$).

4.3.4 Correlations are not bimodally distributed if borders are imposed after pattern formation

So far we have considered only the lowest mode solutions produced by a reaction-diffusion system. To explore whether the results should hold for the more complicated patterns that may be produced by more complex pattern-forming systems, we conducted a sweep of the parameter space, varying the diffusion parameter D_n and the parameter in Eq. 4.1 that weights the contribution of the non-linear coupling term, χ , while keeping $D_c = 0.3D_n$ throughout (Fig. 4.4). For each parameter combination we solved the reaction-diffusion equations on ensembles of domains from randomly seeded Voronoi tessellations.

It was conceivable to us that a degree of correlation (and anti-correlation) may be expected due to chance

for patterns of low spatial frequency, even without the boundary shape constraining pattern formation. So we also solved each system of equations on an ensemble of *circles*, centred at locations derived from the original Voronoi tessellation seed points, but subjected to additional random displacement by vectors whose radii and polar angles were chosen from a uniform distribution, normalised so that the new centres remained inside the original polygons. The size of each circle was chosen so that it minimally overlapped with the corresponding polygon from the original tessellation. We then overlaid the original tessellation onto the ensemble of circles, extracted the field values along the overlaid edges, and obtained the distribution of correlations for each case as previously described. The purpose of this procedure was to remove any possible influence of domain shape while ensuring that the data subjected to analysis were sampled from regions that tessellated precisely.

First we consider the case where $D_n = \chi = 36$ for the constrained condition (Fig. 4.4B) and the control condition (Fig. 4.4C). Visual inspection of the alignment between the control patterns appeared similar to that between patterns formed under the constraints of the polygonal boundaries. However, histograms of the distribution of the correlations showed that they were quantitatively different. The value of α obtained in the boundary-constrained condition was well below the threshold value of 0.5, as expected. By contrast, the histogram obtained in the control condition (Fig. 4.4C) yields $0.5 < \alpha < 1.0$. Since the patterns that formed in this condition were not constrained by the tessellation, the increase in the degrees of freedom of their relative orientations produced a distribution that lost most of the bimodality and which thus approaches the uniform distribution.

Next we consider how the two distributions of adjacent-edge correlations vary across the full range of parameters. Following log transformations of D_n , χ , and α , data obtained from simulations run in the control and boundary-constrained conditions were linearly separable across the full range of parameter values tested (Fig. 4.4A). To confirm this we trained a perceptron to discriminate between control (target response $y = 0$) and boundary-constrained ($y = 1$) data. Training vectors $\mathbf{x} = [\ln(D_n), \ln(\chi), \ln(\alpha), 1]$ were presented in a random sequence and the perceptron weights w_i were updated following each presentation using the delta rule: $\Delta w_i = \epsilon(y - \sigma(u))\sigma'(u)x_i$, where $\sigma(u) = (1 + e^{-u})^{-1}$, $\sigma'(u) = \sigma(u)(1 - \sigma(u))$, and $\epsilon = 0.05$. The resulting weights ($\mathbf{w} = [0.01, -0.46, -3.26, 0.21]$) define a decision

boundary, where $u = \mathbf{x} \cdot \mathbf{w} = 0$, shown as a plane in Fig. 4.4A that clearly separates the data obtained from the two conditions.

In Fig. 4.5, the contour line corresponding to the analytical threshold ($\alpha = 0.5$) runs approximately diagonally across the region, and is effective at distinguishing the influence of the tessellation over more than two thirds of this large parameter space. Example fields and the associated estimates of α are shown for the four extreme corners of the parameter space in Fig. 4.5B. Two are within the region where the threshold can detect the effect of the tessellation on the solutions. Towards the top, where D_n is low, the fields become very concentrated and the nonlinear gradients in the region are so strong that the effects of the boundaries are not transmitted to the interior. However when D_n is larger, parameters that yield complex fields that reflect the amplification of several modes clearly support the hypothesis that the tessellation boundaries constrained pattern formation.

It is possible that amongst the domains of a biological tessellation the control parameters for self-organisation may show some variation. To determine the robustness of the reported effects we therefore re-ran simulations with parameters in the mid-range of the space that was tiled by our initial parameter sweep ($D_n = \chi = 6.0, D_c = 0.3D_n$) and then randomly perturbed these values in each domain by up to 10%. Compared to the unperturbed case, distributions of (adjacent) correlations were not statistically different (Kolmogorov-Smirnov test, $p = 0.997$). When the control parameters were perturbed by up to 50% in each domain, the correlations appeared to diverge a little, but not enough to reject the null hypothesis that they were drawn from the same distribution ($p = 0.31$). Moreover, the effects shown in Fig. 4.5 are not sensitive to the particular choice of pattern-forming system, as confirmed via a sweep through the relevant parameters of an alternative system that does not include a non-linear diffusion coupling term of the type that is parameterised by χ in Eq. 4.1 (see Fig 4.7; (Schnackenberg, 1979; Krause et al., 2021c)).

4.3.5 Emergence of bimodal correlations confirms that column boundaries constrain thalamocortical patterning in the developing barrel cortex

The emergence of subbarrel patterns of thalamocortical innervation density in the rodent somatosensory cortex has been successfully modelled using the Keller-Segel reaction-diffusion system (Keller and Segel, 1971), with the borders of individual barrels imposed as a boundary constraint on pattern formation (Ermentrout et al., 2009) (see *Introduction* and Fig. 4.1). The barrel borders form a Voronoi tessellation, though the edges are typically a little rounded (Senft and Woolsey, 1991). The barrel structure is present from birth and the subbarrel patterns are first apparent at around postnatal day 8, and become clearly defined by around postnatal day 10, in stains for serotonin transporter and other markers for synaptic activity (Louderback et al., 2006). If subbarrel patterns emerge via reaction-diffusion dynamics under the constraints of the barrel boundaries, our analysis predicts that we should see a bimodal distribution of correlations along the common edges of adjacent barrels.

To test this hypothesis, we analysed three images of serotonin transporter expression reported by Louderback and colleagues ((Louderback et al., 2006); their Figure 4). The results of the analysis are shown in Fig. 4.6. We developed a simple computer program to sample the average image pixel intensity in rectangular bins pointing outward-normal to the two parallel sides of a user defined rectangle. Using this tool we defined rectangles to coincide with line segments corresponding to the septal regions that separate the barrels, then for each segment sampled from fifty bins along the outer edge of two adjacent barrel regions, to a depth of twenty pixels ($\sim 85 \mu\text{m}$) into each of the barrels. Care was taken to ensure that the length of each line segment was as long as possible (to include as much of the border as possible), and that the width of each rectangle was as short as possible (to sample as close to the border of the barrels as possible), while not sampling from the septal region itself (to avoid introducing light/dark transitions into the sample that could cause spurious positive correlations). A small number of adjacent edges were excluded as their edges were not clearly parallel, but overall good coverage of the boundaries was achieved.

Examples of the variation in pixel intensity along sampling bins spanning parallel line segments of adja-

cent barrels are shown at the top of Fig. 4.6A, revealing clear correlations and anticorrelations at postnatal day 10. In real data like this, it is conceivable that the technique could pick up spurious correlations, for example if image artefacts appeared in the sample from both edges of a pair, but we note that visible artefacts (e.g., circular bubbles of light or dark related to the underlying vasculature) very rarely spanned the width of the septa and when they did were very rarely located in or around the septa. Moreover, as noted above, anticorrelations are not to be expected by chance.

Images obtained from rats at postnatal days 5, 8, and 10 were analysed. At postnatal day 5, prior to when subbarrel patterns are reported to emerge, we found the distribution of adjacent-pair correlations in serotonin expression to be unimodal, about a mean value of 0.18 ± 0.34 . At postnatal day 8, when subbarrel patterns are reported to become apparent, two distinct peaks at a correlation of approximately ± 0.5 were also apparent. At postnatal day 10, when subbarrel patterns are reported to be well defined, and were clearly visible in the image of serotonin expression, the distribution was clearly bimodal, with essentially all pairs showing non-zero correlations. Only the P10 distribution failed a test of unimodality (Hartigan's dip test; $p = 0.01$). Fitting the distribution of correlations using Eq. 4.2 yielded an estimate of $\alpha = 0.94$ and $\beta = 0.5$ at postnatal day 5 (P5), an estimate of $\alpha = 0.65$ and $\beta = 0.33$ at P8, and $\alpha = 0.50$ and $\beta = 0.36$ at P10. While the theory predicts that the distributions should be symmetric, i.e., $\alpha = \beta$, the larger estimates for α reflect a general shift in each distribution to the right due to additional sources of positive correlation to be expected when extracting a fairly small sample from image data, as previously noted. As α is the parameter more sensitive to the presence of anticorrelations, we interpret its decrease, by P10, to a value that strongly supports the hypothesis that the domain boundaries constrained pattern formation, as strong evidence that subbarrel patterns emerge postnatally under constraints imposed by the barrel boundary shapes.

Thus our analysis supports the model of subbarrel pattern formation as a product of reaction-diffusion dynamics constrained by the barrel boundary shapes (Ermentrout et al., 2009). Moreover, this result demonstrates how the definition of constraint as a causal influence on biological process can practically be operationalized in terms of the distribution of adjacent pairwise pattern correlations, for reaction-diffusion systems on tessellated domains.

4.4 Discussion

We have shown that because the shape of a domain boundary aligns pattern formation via reaction-diffusion, pattern formation within adjacent domains of a tessellation gives rise to an alignment between those patterns that can be measured as a strong (anti-)correlation between cells located on either side of a common boundary. Our simulation results demonstrate that the alignment of patterns in adjacent domains is predicted to be robust, with alignment occurring over a wide range of length scales, as set by the diffusion constants, and in reaction-diffusion systems both with and without non-linear coupling of the dynamic variables (Fig. 4.5 and Fig. 4.7). They also demonstrate that while rounding the vertices of the domains reduces the effect, it does not destroy it, and hence alignment is likely also to occur in biological domains where the boundary shapes may be less strictly polygonal (Fig. 4.3E). Our results show that the effect is not to be expected in tessellated domains whose boundaries did not constrain pattern formation (Fig. 4.4B). Hence they establish how bimodality in the distribution of correlations measured across adjacent edges of a tessellation (and specifically the presence of anti-correlations) can be used to test the hypothesis that the domain boundaries constrained pattern formation via reaction-diffusion. This hypothesis was confirmed by the analysis of patterns of cell density that are thought to be formed via reaction-diffusion dynamics in the rodent somatosensory cortex, as a specific example system (Fig. 4.6).

The alignment effect is paradoxical, and an interesting biological example of action at a distance, because the process of pattern formation within a given domain occurs entirely independently of pattern formation in any other, and thus it involves no communication between cells that are located in different domains. Yet the effect is quite understandable, in geometric terms, when we consider that the boundary conditions of a given domain implicitly contain information about the boundary conditions of other domains, in the knowledge (or under the assumption) that those domains tessellate, and hence are related by a common underlying causal structure; e.g., by the collection of seed points from which a Voronoi tessellation originates.

Ours is not the first demonstration that biological variables can become synchronised in spatially sepa-

rate populations that do not communicate directly. For example, it is well known that the similarity in weather patterns between two locations tends to decrease with the distance between them. And as such, population dynamics in two separate groups of conspecifics that do not interact will tend to be correlated if their habitats are nearby, due to the effects of a common weather pattern as a mediating ‘third’ variable. This is an example of the “Moran effect” (Moran, 1953; Royama, 1984, 2005; Blausius and Stone, 2000). The effect we have described is distinct in two ways. First, it arises from comparisons between the structures of patterns that vary in space and time (i.e., in systems described by partial differential equations), whereas the Moran effect describes temporal fluctuations only and is thus typically modelled using systems of ordinary differential equations. Secondly, the correlations studied here originate from the *constant* effect of the boundary conditions on pattern formation, rather than by the common influence of any time-varying quantity. We expect that both effects may yet be understood as instances of a more general class of phenomena by which spatial relationships between environmental variables (i.e., in terms of their proximity or boundary shapes) induce correlations between otherwise decoupled populations. To this end, future investigations may extend the analysis developed here to the study of systems whose solutions oscillate in both space and time.

Indeed, the potential importance of the effect established here for understanding biological organization comes into focus when we consider how such causal structures might interact at different timescales (Kauffman, 1993; Rall, 1996). Specifically, how might the alignment of patterns by their boundary constraints in turn constrain the slower processes that are involved in maintaining those boundary constraints? We can think of two broad answers, relating to the affordances of pattern alignment for material transport, and for information processing, though there may be several more.

In terms of material transport, if the pattern of concentration produced by a reaction-diffusion system corresponds to the density of cells or other physical obstacles, as it does in the example of neocortical patterning, then correlations along a common boundary edge create, in the regions of low concentration, channels through which other materials may flow. Uncorrelated patterns, such as those generated by our control simulations (Fig. 4.4B), are discontinuous at all borders and here create bottlenecks that restrict the flow of small materials and stop the flow of larger materials. In these terms, the anti-correlations

that come with pattern alignment are of course bottle tops, permitting no flow at all, but with anti-correlations come correlations and thus the opportunity for unrestricted flow of small and large materials via the emergent channels. If transport of materials through these emergent channels participates in the maintenance of the objects that constitute the borders, for example by supplying them with energy or clearing their waste products, then the alignment of patterns by the boundary constraints in turn becomes a (useful) constraint on those boundary constraints.

As an interesting example, the Voronoi-like tessellation of dark patches that gives the giraffe skin its distinctive patterning is geometrically related to an underlying vascular system. Particularly large arteries running between the patches supply a network of smaller arteries within the patches, which allow them to act as ‘thermal windows’ that efficiently radiate heat, and thus enable giraffes to thermoregulate in warm environments (Mitchell and Skinner, 2004). We note that giraffe panel substructures, not unlike subbarrel patterns in appearance, vary with the size of the panels, which in turn vary with the size of the animal in a manner predicted by reaction-diffusion modelling (Murray, 1989). This raises the intriguing possibility that a relationship between the structure of the vascular network and giraffe panel (and sub-panel) geometry may reflect a closure of constraints, co-opted for the thermal advantages it affords to these particularly large endotherms.

In terms of information processing, clustering of neurons to form tessellated patterns of cell density in and between brain nuclei constrains the transmission of signals between brain cells, and thus affords an opportunity for new information to be derived with reference to the underlying geometry, in turn enabling specific computations which facilitate survival (Wilson and Bednar, 2015; Bednar and Wilson, 2016; Sterling and Laughlin, 2015). The mammalian neocortex again provides a useful example. The arrangement of the barrels across the somatosensory cortex of rodents reflects the layout of the whiskers on their snouts, with cells of adjacent barrels responding most quickly and most strongly to deflection of adjacent whiskers. The relatively large size of the barrels, and the relatively slow velocities with which their efferents conduct action potentials, render downstream cells differentially sensitive to the relative timing of adjacent whisker deflections by virtue of their location with respect to barrel boundaries (Wilson et al., 2011). Neurons close to the borders respond selectively to coincident whisker deflections,

and neurons that are closer to barrel A are selective for deflections of whisker B that precede deflections of whisker A by larger time intervals (Shimegi et al., 2000). As such, the system can use the underlying geometry to compute the relative time interval between adjacent whisker deflections via place-coding (Jeffress, 1948; Izhikevich and Hoppensteadt, 2009).

Within the additional cellular clusters that are formed via subbarrel patterning, neurons are tuned to a common direction of whisker movement (Bruno et al., 2003), and somatotopically aligned maps of whisker movement direction subsequently emerge, such that deflection of whisker A towards B selectively activates neurons of barrel A that are closest to barrel B (Andermann and Moore, 2006). This particular alignment of information-processing maps is thought to occur by the specific constraints that the barrel and sub-barrel geometry imposes on the otherwise general-purpose processes of reaction-diffusion and Hebbian learning by which cortical maps self-organize (Wilson et al., 2010; Kremer et al., 2011). The relationship between these two patterns that is suggested by the present results provides a potential geometrical basis for the integration of sensory information. The alignment of within-barrel and between-barrel maps could render downstream cells sensitive to the coherence between single-whisker deflection directions and multi-whisker deflection intervals resulting from movement of tactile stimuli through the whisker field (Kida et al., 2005). The net effect could be a representation of the ‘tactile scene’ that affords new possibilities for hunting and obstacle avoidance (Jacob et al., 2008).

There are many other examples of tessellated patterns in the brain, including spots and stripes in primate primary visual areas, and barrel-like structures in the brainstem, thalamus, and extrasensory cortical areas in rodents, as well as in various cortical areas in moles, dolphins, manatees, platypus, monkeys, humans, and more (see (Manger et al., 1998) for an overview). The precise role that these patterned modular structures (fields, stripes, barrels, blobs) might play in cortical information processing is yet to be fully characterised (Purves et al., 1992; Wilson and Bednar, 2015; Bednar and Wilson, 2016). However, in purely geometric terms, strong relationships between the shapes of cortical modules and the functional maps that they support have been well established. For example, iso-orientation contours radiating from the pinwheel centers that characterise topological maps of orientation preferences in primate primary visual cortex intersect with the boundaries of ocular dominance stripes at right angles (Issa et al., 2008;

Xu et al., 2007). And numerous features of these functional maps have been successfully modelled in terms of reaction-diffusion dynamics (e.g., see (Swindale, 1996; Miikkulainen et al., 2005; Wolf, 2005b; Kaschube et al., 2010)). Hence, considering only neocortical patterning, it seems the opportunities for constraint closure in the brain via computational geometry are abundant.

Montévil et al. (Montévil et al., 2016) consider that reaction-diffusion dynamics introduce changes in the symmetries of a system that are *generic*, insofar as they derive from a restricted space of possibilities. By contrast, they consider organized biological wholes to be additionally defined by constraints that are *specific*, insofar as their dynamics depend on a history that spans ontogenetic and phylogenetic timescales. In these terms, they suggest that modelling focused on deriving generic symmetries, which includes reaction-diffusion modelling, will ultimately fail to capture the individual accumulation of idiosyncrasies that characterize biological wholes (see also (Kauffman, 2019,0)). While we agree with the importance of the history for understanding biological wholes, we do not agree that models formulated in terms of generic constraints are therefore fundamentally limited to describing only biological parts. The alignment of patterns between adjacent domains studied here constitutes a new (generic) symmetry that is invariant to the (specific) pattern that forms in either domain. Thus the local symmetry-breaking that generates patterns (i.e., Turing instability) also gives rise to symmetries that persist in the longer term (i.e., pattern alignment). As such, the opportunities that the alignment might afford to other processes (structural, transport, information-processing), persist at the same timescale at which the boundary conditions themselves persist. And if such processes can help to maintain the boundary conditions, for example by channeling an external supply to the cells that form the boundary, then the system achieves constraint closure, and hence the status of a biological whole (c.f. (Montévil and Mossio, 2015)). Indeed, the alignment between reaction-diffusion processes in tessellated domains, and the possibility for constraint closure that this affords, may prove to be a useful theoretical model through which to explore, by analysis *and* synthesis, the fundamentals of biological organization.

4.5 Materials and Methods

4.5.1 Numerical methods

Solutions to the reaction-diffusion equations (Eq. 4.1) were obtained numerically on a discretized hexagonal lattice of grid points using the finite volume method described by (Lee et al., 2014), and a fourth-order Runge-Kutta solver was used to advance the solutions to a steady state (parameter values were chosen so that all solutions were eventually constant in time, i.e., patterns were stationary). Simulations were written in C++ with the help of the support library *morphologica* (James and Wilson, 2021) (see also James et al. (2020)). We verified that all simulation results reported were insensitive to the choice of spatial discretization (i.e., to the lattice density). A hexagon-to-hexagon distance of $O(10^{-3})$ on a domain whose spatial scale was normalized to be $O(10^0)$ was found to be sufficient. At this scale, domains contained $O(10^2)$ hexagonal grid-points and edge vectors with length $O(10^1)$.

No-flux boundary conditions were applied at the edges of the domains derived from a given tessellation, by setting all the normal components of the spatial gradient terms in Eq. 4.1 to zero. Importantly, the *tangential* gradients at the boundary were not constrained, allowing the patterns on either side of the boundary to represent the pattern in the whole domain while patterns across adjacent boundary edges had no constraints that might be correlated. Solutions were considered to have converged when the mean of the absolute differences in field values sampled at intervals of 1000 timesteps fell below $\sim 10^{-10}$.

To compare the solutions along pairs of boundary vertices picked from two domains, the Pearson correlation coefficient was calculated. Vectors \mathbf{x}_1 and \mathbf{x}_2 each contained the solution values in the hexagonal grid points along (and one hexagon-to-hexagon distance inside) a boundary vertex from either domain. The boundary lines are shown in black in Figs. 4.3, 4.4, 4.5, and the samples \mathbf{x}_i were taken immediately adjacent to these boundary lines on either side. The field values of the solutions were always observed to vary smoothly along the edges and samples were thus not distorted by any boundary-related artefacts. These vectors were combined to compute the correlation coefficient, as $r(\mathbf{x}_1, \mathbf{x}_2) = \frac{\langle \mathbf{x}_1, \mathbf{x}_2 \rangle}{\|\mathbf{x}_1\| \|\mathbf{x}_2\|}$, where the numerator represents the Euclidean scalar product and the denominator gives the product of the Euclidean norms. This operation can be thought of as measuring the angle between two unit normal

vectors. As such, the distribution of the correlations may be considered a property of their distribution in a surrounding space – correlations lie on a hypersphere whose dimension is between 1 and $D - 1$, with D the dimension of the containing space.

When comparing randomly matched edge vectors, the length of the shorter vector was increased to match that of the longer vector by linear interpolation. For all such results, the distances between interpolation points, even for the shorter vectors, were far smaller than the wavelengths that were observed to be amplified by pattern formation. Interpolating along the shorter vector was therefore appropriate, and preferable to downsampling along the longer vector, to avoid discarding information.

Code for running the simulations reported in this paper is available at <https://github.com/ABRG-Models/Tessellations>.

4.5.2 Derivation of a test for the influence of boundary shape

Using $\alpha < 0.5$ as a threshold value for determining whether a set of patterns was constrained by the boundary shape can be justified analytically as follows. Consider a collection of edge patterns that are pinned to the vertices so that the maximal and minimal field values always appear at the two ends of each edge. The simplest (lowest mode) pattern that can be fitted to this constraint is a wave function $\cos(\theta)$, where θ ranges from $[0, \pi]$. The correlation r between two such functions is given by their dot product

$$r = \pm \frac{\int_0^\pi \cos^2(\theta) d\theta}{\sqrt{\int_0^\pi \cos^2(\theta) d\theta} \sqrt{\int_0^\pi \cos^2(\theta) d\theta}}, \quad (4.3)$$

where the denominator gives the normalisation so that the vectors are of unit length, and hence Eq. 4.3 returns either $r = 1$ or $r = -1$. If we relax the constraint that the patterns must be pinned to the vertices and allow the pattern along each edge to shift by $\phi \in [-\pi, \pi]$, where ϕ is drawn from a uniform distribution, then we need to evaluate

$$r = \frac{\int_0^\pi \cos(\theta) \cos(\theta + \phi) d\theta}{\sqrt{\int_0^\pi \cos^2(\theta) d\theta} \sqrt{\int_0^\pi \cos^2(\theta + \phi) d\theta}}. \quad (4.4)$$

By the simple change in variables, $\theta = \theta + \phi$, we can see that the denominator in Eq. 4.4 is the same as in Eq. 4.3. Expanding the numerator gives

$$\int_0^\pi \cos^2(\theta) \cos(\phi) d\theta - \int_0^\pi \cos(\theta) \sin(\theta) \sin(\phi) d\theta. \quad (4.5)$$

Either by explicitly evaluating the integral or by noting that $\cos(\theta)$ and $\sin(\theta)$ are anti-symmetric and symmetric about the midpoint of the range of integration, we can see that the second term vanishes, and hence that Eq. 4.4 becomes

$$r = \frac{\cos(\phi) \int_0^\pi \cos^2(\theta) d\theta}{\int_0^\pi \cos^2(\theta) d\theta} = \cos(\phi). \quad (4.6)$$

Therefore the distribution of correlations consists of values given by $\cos(\phi)$, where ϕ is a random variable drawn from a uniform distribution over $[-\pi, \pi]$. This is exactly equivalent to the distribution of the dot product between two vectors on the unit circle with an angle between them that is chosen from a random uniform distribution. Thus it gives a symmetric beta distribution with $\alpha = 0.5$ (see e.g. (Anderson, 2009) Ch. 4).

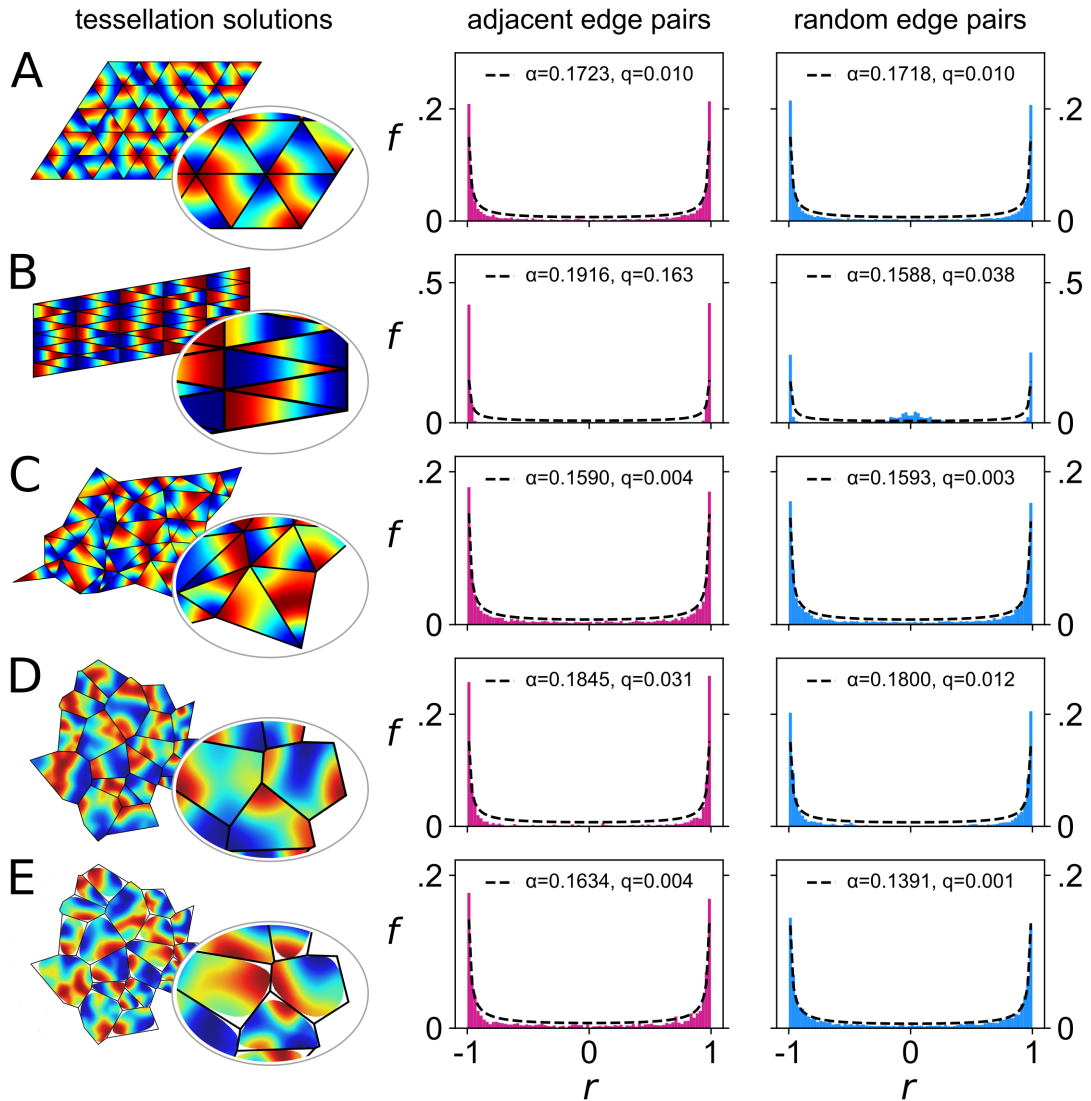


Figure 4.3. *Correlated pattern formation in adjacent tessellation domains without communication.* A system of reaction-diffusion equations (Eq.4.1; $D_n = \chi = 36$) was solved using boundary shapes that tessellate in different ways (left column), with blue and red corresponding to extreme positive and negative values, and black lines delineating the domains. Values were sampled along the individual vertices of each domain and samples were correlated between edges of *different* domains, either amongst pairs of edges that are adjacent in the tessellation (center column) or randomly selected (right column). Histograms show the distributions (f) of correlation coefficients (r) obtained in either case, which were fit by the beta-distribution (dotted line) parameterized by α (see text for details; q is the sum of squared differences between the data and the fit). Rows **A-E** show data obtained from tessellations comprising domains with different shapes: **A** equilateral triangles; **B** isosceles triangles; **C** scalene triangles; **D** a Voronoi tessellation; **E** a Voronoi tessellation with rounded vertices. Peaks at ± 1 in the histograms indicate that while pattern formation occurs entirely independently within each domain, patterns may become correlated between (adjacent) domains due to common constraints that derive from the fact that their boundary shapes tessellate.

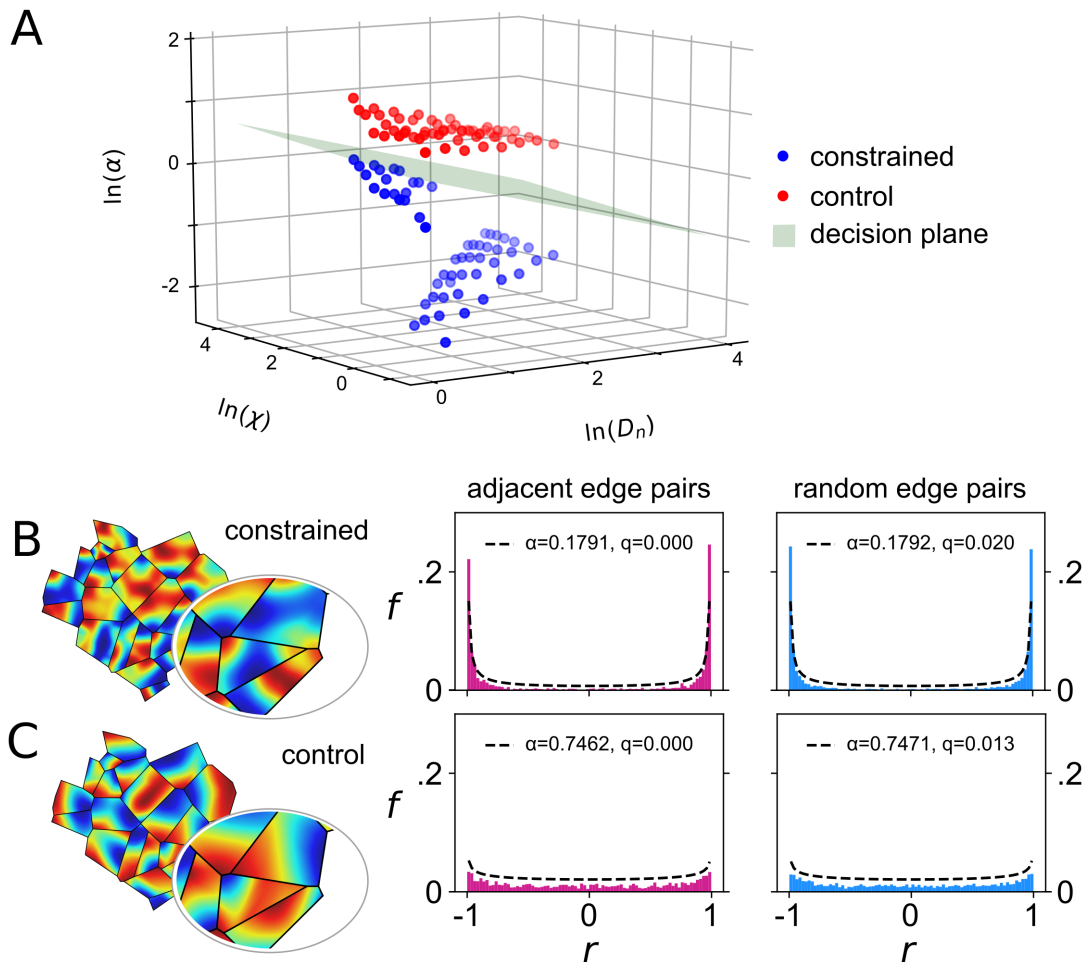


Figure 4.4. Analysis of control patterns formed without shaped boundary constraints registers only very weak correlations. Combinations of eight values of the diffusion constant D_n and eight values of the constant χ that weights the non-linear coupling term were evaluated on domains of a Voronoi tessellation generated from random seed points. The remaining free parameter, D_c was set to $0.3D_n$, and increments in χ were expressed as proportions of D_n to cover a large parameter space. In the ‘constrained’ condition, the shapes of the domain boundaries were a constraint on pattern formation. In the ‘control’ condition, solutions were obtained in circular domains, and the tessellation boundaries were imposed only after pattern formation, to allow a corresponding set of correlations to be measured for comparison. **A** Values of α were obtained in each condition and for each parameter combination by fitting the resulting distribution of adjacent-edge correlations. Only weak bimodality (high α) was observed in the control condition. Following a log transformation to each axis, α values were clearly linearly separable, as confirmed by the success of a perceptron in discriminating the two conditions (perceptron decision boundary shown in green). Example solutions in the constrained and control conditions are shown in **B** and **C**, respectively, for the combination of parameters ($D_n = \chi = 36$) that yielded the lowest α values in the control condition ($\alpha = 0.64$).

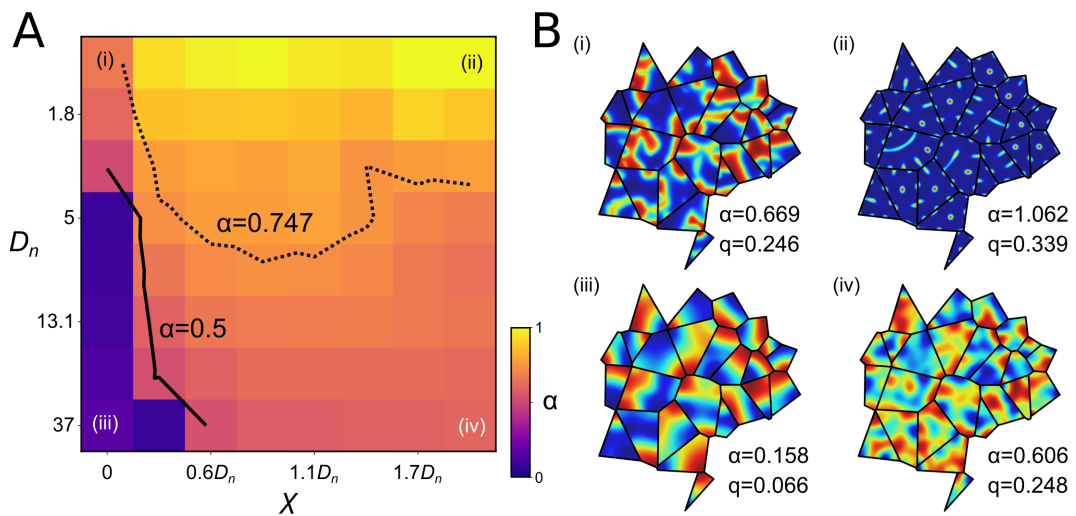


Figure 4.5. *Correlated pattern formation in tessellated domains is predicted to emerge robustly across a wide range of pattern-forming systems.* Correlations between self-organized patterns in adjacent domains of randomly seeded Voronoi tessellations were measured across a wide range of parameters. Panel **A** shows values of α estimated from the distribution of 1000 pairwise correlation coefficients obtained from each of sixty four combinations of parameter values (as in Fig. 4.4A; ‘constrained’). The overlaid contour corresponds to the threshold, $\alpha = 0.5$, at or below which the hypothesis that the domain boundaries constrained pattern formation is very strongly supported. Based on the former, patterns are expected to be correlated by the tessellation boundary constraints across a large portion of the parameter space. Panel **B** shows example patterns for four extreme cases.

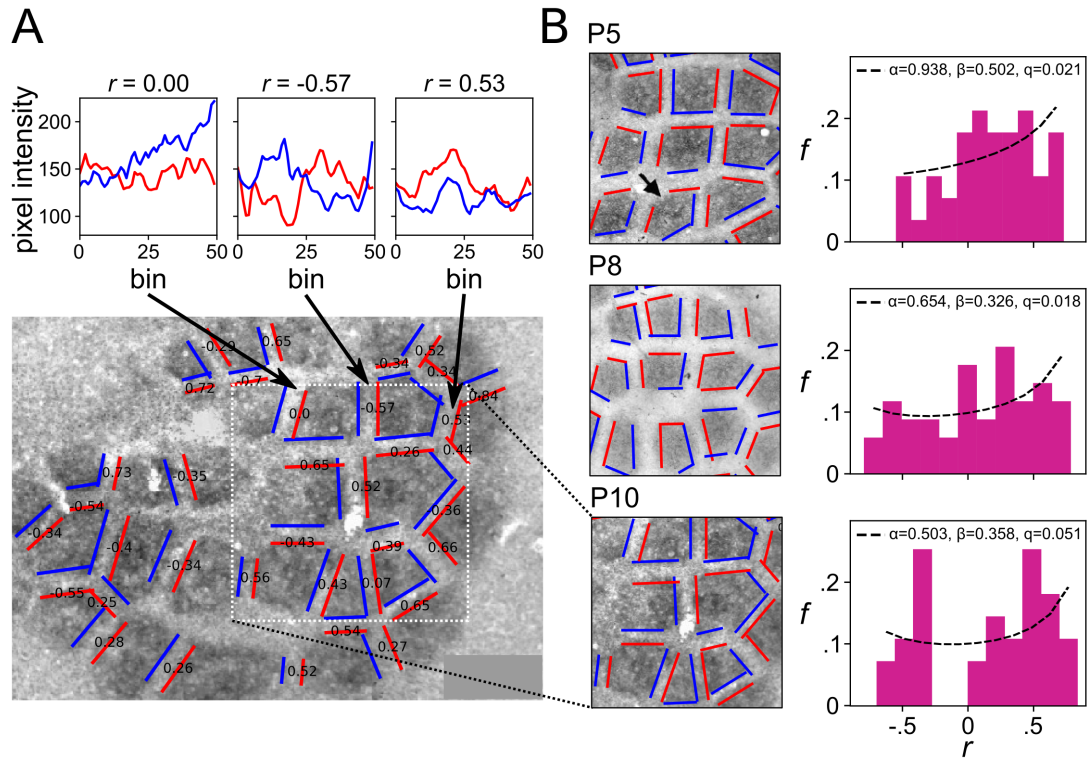


Figure 4.6. *Emergence of correlated patterns in adjacent domains of the developing neocortex.* We analysed images of immunohistochemical stains for serotonin transporter (5-HTT) expression on the surface of the rat barrel cortex, obtained at postnatal days 5 (P5), 8 (P8), and 10 (P10). This stain reveals the shapes of the barrel columns, each corresponding to a whisker on the animal's snout, as large dark polygonal patches forming a Voronoi tessellation. From P8, sub-barrel structures become apparent and by P10 they clearly identify several regions of high synaptic density within many barrels. Panel **A** shows the details of the analysis method for the P10 image. Overlaid pairs of parallel red and blue lines show the extents along which image intensity was sampled for each pairwise comparison. Each line marks a vertex of the barrel boundary, and samples were constructed by averaging the grayscale intensity of pixels in one of 50 regularly spaced rectangular bins extending a short distance in from the line towards the corresponding barrel center. The correlation coefficient for each pair of samples is shown in black text, and the plots above show sampled data used for three example pairwise comparisons. Distributions of correlation coefficients obtained from pairs of edges from adjacent barrels are shown for each postnatal day in **B**, showing a clear progression from a unimodal shape at P5 to a bimodal shape at P10, and supporting the hypothesis that pattern formation within the barrels occurs postnatally and is constrained by the barrel boundary shapes. Original images from (Louderback et al., 2006).

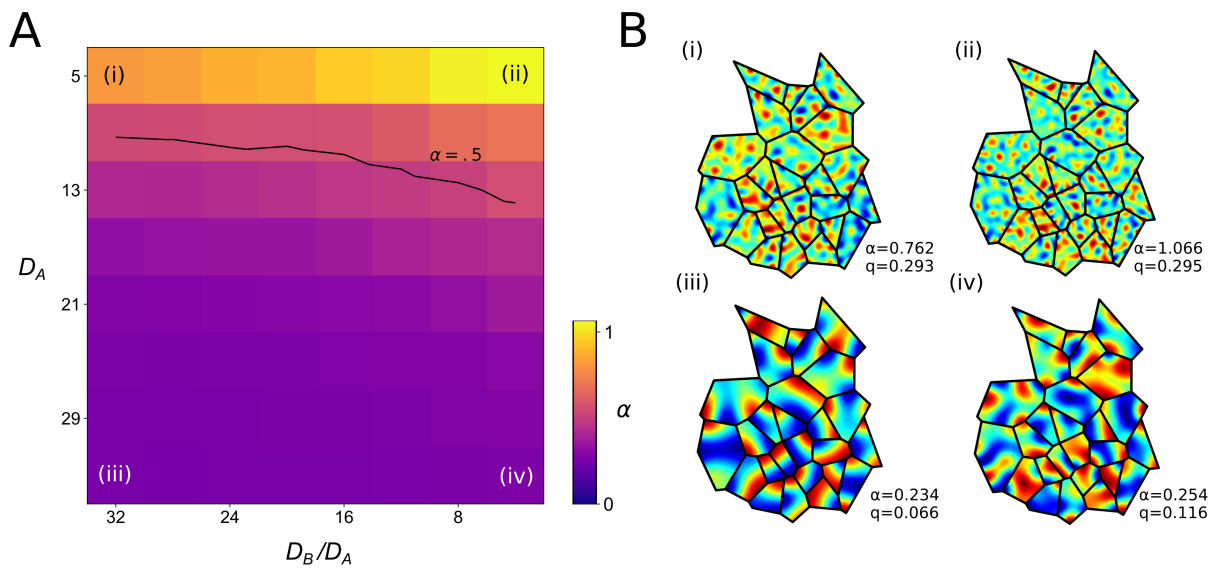


Figure 4.7. *Correlation of patterns in a system with the Turing mechanism.* We conducted a parameter sweep comparable to that presented in Fig. 5, instead using the Schnackenberg reaction-diffusion system (Schnackenberg, 1979), whereby patterns form via the Turing mechanism. This system has no nonlinear diffusion term and its dynamics are driven by the magnitudes and ratios of two parameters that scale the linear diffusion operators, D_A and D_B (see (Krause et al., 2021c)). **A** shows values of α obtained across a large portion of the parameter space, with the ratio of the two diffusion parameters, D_B/D_A , decreasing along the horizontal axis. The gradient in α corresponds well to that shown in Fig. 5 using the Keller-Segel model. **B** shows examples of the field patterns for parameter values corresponding to the four corners in **A**.

Chapter 5

Constraints on topological feature-map self-organisation

5.1 Introduction

The previous two chapters have described the effects of geometry and dynamics on pattern formation on structure formation, patterns are formed out of the stomata of cortical neurons. Here we examine their effects on pattern formation in feature mapping. Feature maps can develop in the cortex where the patterns are formed by the responses of columns of neurons to particular stimuli. In this chapter we investigate patterns formed by the response of neurons in the V1 area of the visual cortex to particular orientations. These responses can be modelled as a topological feature map (Wilson and Bednar, 2015). Many of the terms and ideas of cortical organisation have been discussed in chapter 1 to which reference should be made for a fuller discussion of the biological considerations of cortical structure and function. In modelling the mapping of orientation preferences, we need to take note of two observable quantities. The first is the selectivity, how strong a neuron's response is to a given direction, and the second is the direction itself. In the experimental investigation of these responses it has been found that in several different types of mammals the orientation preferences are organised as ribbons of a particular prefer-

ence that form patterns organised around topological singularities called “pinwheels” (Bonhoeffer and Grinvald, 1991). At these singularities ribbons of different patterns spiral into a centre which thus has a topological charge

$$q = \frac{1}{2\pi} \oint_C \nabla \theta d\vec{l} \quad (5.1)$$

where θ is the orientation preference in the range $0 - \pi$ since we do not give a sign to the orientation, C is a small contour around the pinwheel centre. The charge, q , is topologically constrained to only have values $\pm n/2$. For points away from the pinwheel singularities $q = 0$, from observations in mammals with pinwheel patterns $q = \pm 1/2$ at the phase singularities, thus the orientation ribbons do not wind multiple times round the singularity.

There has been discussion over whether the pinwheel patterns develop due to the influence of sensory input or whether they are formed by some spontaneous symmetry-breaking dynamics. In this context it is relevant to note that there exist mammals whose V1 cortex does have columns with orientation preference but these are distributed much more randomly and do not show pinwheel structure. Pinwheel organisation is not essential to the detection of orientation. Thus, as discussed in general survey of chapter 1, patterns may not be formed primarily for information processing purposes but may arise from general structure forming dynamics and can then be utilised in the evolutionary development of different organisms in different ways. In the background work which informs this chapter both learning and spontaneous pattern formation were examined. Much of this work has modelled the V1 and V2 domains with periodic boundary conditions, implicitly assuming an infinite domain, i.e. possible constraints caused by boundaries are neglected. However, (Keil and Wolf, 2011) does consider boundary effects and the results obtained here will be compared with this work in the discussion at the end of this chapter. We will specifically examine the effects produced by modelling in a finite domain with noflux boundary conditions imposed. One immediate and profound effect of this is that translational symmetry which has been important in formulating the models described here is broken.

There have been several modelling frameworks developed to exhibit and study pinwheel development. The *elastic net* model models the development of singularities due to the projection of a feature space

of dimension greater than two onto a flat surface representing the cortex (Durbin and Mitchison, 1990). The justification of representing the cortex as a 2D sheet is that the V1 cortex appears to be organised in vertical columns spanning the layers of the cortex and all layers of such a column respond maximally to the same orientation. The projection is a nonlinear mapping that attempts to optimising some multi-objective function defined on feature space. Examples of objectives are; continuity of orientation preference, continuous mapping of retinotopic space, continuous mapping of ocular dominance (which eye is selectively responded to by the column). It is impossible to map from such a higher dimensional space to the 2D cortical surface without topological singularities, of which pinwheels are an example.

Neural field models are much closer to the processes of neural firing and synaptic connections between neurons known from the study of the behaviour of neurons. The models use a mean field formalism to model the behaviour of populations of neurons to give a continuous representation of neuron behaviour, which is justified by considering the huge density of neurons relative to gradients of behavioural response. The development of the behaviour of the neural fields is driven by mechanisms of Hebbian learning of the models under inputs which can be random fields or else fields derived from natural scenes (Stevens et al., 2013). These models can be used to more directly models the physical mechanisms operating in pattern formation, for example to examine the balance between excitation and inhibition by transverse links in the cortex and the balance of local and long range connections (Rankin and Chavane, 2017).

Global optimisation models are similar to elastic net models in that they seek to minimise some global measure, but they are constructed by considering the symmetries of the feature and cortical area spaces rather than as projections from feature to cortical space (Wolf, 2005b), (Wolf, 2005a). By building their analysis on considerations such as symmetry they attempt to abstract from the details of the processes that shape the development of neuron preferences. Given that there is so much that is not yet known about these processes this holds the promise of finding fundamental features of pattern formation, however it makes them more difficult to compare with experimental behaviour.

However the global optimisation models have drawn attention to a measure that meets the criteria of

model independence but is also capable of experimental validation. The measure is a scale independent density of the pinwheels defined as

$$\hat{\rho} = P_{\Lambda} \quad (5.2)$$

here $\hat{\rho}$ is pinwheel density, P_{Λ} is the pinwheel count in an area defined by Λ^2 which is a characteristic length scale of the patterns, namely the typical distance between hypercolumns of neurons with a similar orientation. The motivation of this definition is to give a definition of $\hat{\rho}$ that is set by the pattern of selectivity of the hypercolumns and not by their size, which may be different in animals with differently sized brains. Thus $\hat{\rho}$ is a dimensionless quantity. If the ensemble of incoming patterns can be described as Gaussian field it can be shown that $\hat{\rho} = \pi$ is a minimum value (Wolf and Geisel, 1998). A Gaussian field is a field where the correlation between the field values at spatially separated points is derived from a Gaussian distribution (Adler and Taylor, 2007). It can be shown that this result can be deduced from the symmetry properties of the Gaussian field (Afgoustidis, 2015). It should be noted that the Gaussian nature of the cortical patterns depends on assumptions about the symmetry and randomness of the visual signals that impact on the retina. In particular it is necessary to assume that the modification of neuronal response to a single visual signal is sufficiently small so that the development of the cortical field depends on the properties of the ensemble of possible input signals. A neural field model has been used to show that if the response to individual patterns is not sufficiently damped, then the result $\hat{\rho} = \pi$ is no longer observed (Stevens et al., 2013). The importance of the input signals in the development of cortical patterns has been demonstrated by wiring the visual input from the retina to the auditory area of the sensorimotor cortex, orientation selective neurons are organised on patterns of orientation columns that are absent from the normally wired auditory region (Sharma et al., 1998).

5.2 Results

5.2.1 Construction of a model for pattern formation

Given the orientation of this thesis towards methods that are not dependent on the details of modelling, but are oriented towards universality in behaviour, we develop the analysis of the third type of model

discussed above, namely the global optimisation models. The following presentation is modelled on that given in (Wolf, 2005a). The model considers a mapping from the cortex modelled as \mathbb{R}^2 to \mathbb{C}^1 which represents the response of a neuronal column to a set of input orientations θ_k as

$$z(\vec{x}) = \sum_k e^{i2\theta_k} E_k(\vec{x}) \quad (5.3)$$

The reason why the exponent of the phase term has the factor 2 is that the neurons respond to the orientation without discriminating its direction. The responses of the column $E_k(\vec{x})$ will evolve with the input signals and if the condition that the response to individual signals is sufficiently small so that the eventual responses across the cortex are governed by the statistics of the ensemble of inputs then we can incorporate the statistics of the input into a dynamical system that is autonomous

$$\frac{\partial}{\partial t} z(\vec{x}) = F[z(\cdot)] \quad (5.4)$$

Here the square brackets $F[\cdot]$ indicates that the form of F will be dependent on the response to an ensemble of input signals. $z(\cdot)$ indicates that the RHS may be dependent on long range as well as purely local cortical dynamics. For an individual location if we consider the polar representation $z(\vec{x}) = r(\vec{x})e^{i\theta(\vec{x})}$ then r gives the selectivity of the response to the preferred orientation θ . The optimisation nature of the model is given by the assumption that $F[\cdot]$ derives from a global potential and that the development of the orientation preferences of the cortical map can be derived as an evolution towards minimisation of this potential.

(Wolf, 2005a) proceeds to develop the model in various stages. The first, which derives from (Wolf and Geisel, 1998) shows how assumptions that the initial dynamics is determined purely by the statistical properties of the input considered as a Gaussian field leads to development of cortical patterns of response that are Gaussian random fields. As described above such fields have a pinwheel density bounded below by $\hat{\rho} \geq \pi$. As the dynamics develops, a process of pinwheel annihilation leads to a reduction in the pinwheel density, which can lead to striped patterns that are devoid of pinwheels. Consequently further development of the model is considered to look at its stability properties as it deviates from the random

Gaussian field configuration. These dynamics are developed from the action of symmetry constraints on the form of the RHS of (5.4).

The three symmetries are

1. Translational symmetry $F(Tz(\vec{x}, t)) = TF(z(\vec{x}, t))$ with $T(z(\vec{x})) = z(\vec{x} + \vec{y})$
2. Rotational symmetry $F(z(R_\theta \vec{x})) = R_\theta F(z(\vec{x}))$ with $R_\theta z(\vec{x}) = z\left(\begin{pmatrix} \cos(\theta) & \sin(\theta) \\ -\sin(\theta) & \cos(\theta) \end{pmatrix} z(\vec{x})\right)$
3. Orientation symmetry $F(e^{i\phi} z(\vec{x})) = e^{i\phi} F(z(\vec{x}))$

Note that for this to make sense we are treating the function F as a mapping $\mathbb{R}^2 \rightarrow \mathbb{C}$ as for $z(\vec{x})$, so it is implicit that F can be expressed as $F(\vec{x})$ in order for the symmetries to be applied to the rhs of (5.4). The first two symmetries derive from the symmetry properties of \mathbb{R}^2 . Translational symmetry requires that the domain be infinite, this can be seen to be an idealisation and any form of boundary condition applied to (5.4) at a finite boundary will violate it. Rotational symmetry expresses a requirement that interaction between different points on the cortex depends only on the vector between them and not to any direction applied to the cortex as a whole. The third is different in that it relates to a symmetry in \mathbb{C} the space of cortical responses and not to \mathbb{R}^2 , the cortical surface. It expresses the requirement that there be no global orientation preference. This third symmetry means that if $F[z(\cdot), z(\bar{\cdot})]$ in (5.4) where \bar{z} denotes the complex conjugate, is expressed as a Volterra power series,

$$F[z(\cdot), z(\bar{\cdot})] = \sum_{n=0}^{n=\infty} N_n(z(\cdot), z(\bar{\cdot})) \quad (5.5)$$

where $N_n()$ denotes the sum of monomials in z, \bar{z} whose order is n , then all terms where n is even vanish. Moreover all odd order terms must be of the form $F'(z, \bar{z})z$ where F' is an even monomial.

A further restriction placed on the dynamical system is that $z = 0$ is a solution of the system and the the initial instability of this solution it to a solution of a single finite wavelength. As the control parameters are varied from the point of instability a range of wavelengths can appear but right at the bifurcation point the single finite wavelength property holds. This condition is often applied in investigating the dynamics

of fields with pinwheels however it is not necessary for the $\hat{\rho} = \pi$ condition to hold (Afgoustidis, 2015).

5.2.2 Swift-Hohenberg equations

A very simple form of dynamical system that meets the requirement of a single finite wavelength system is the Swift-Hohenberg equation (Swift and Hohenberg, 1977). The single finite wavelength instability is ensured by the linear terms and there are different versions of the such systems with different forms for the nonlinear terms which truncated at third order of nonlinearity. Since we are dealing with a complex field over \mathbb{R}^2 we require the complex form of the equation. Following the symmetry analysis above we have only odd order terms. Near to the bifurcation we make the approximation of truncating at third order to obtain,

$$\frac{\partial z(\vec{x}, t)}{\partial t} = rz(\vec{x}, t) - (k_c^2 + \nabla^2)^2 z(\vec{x}, t) - N_{3L}(z(\vec{x}), t) - N_{3NL}(z(\vec{x}, t)) \quad (5.6)$$

where $z(\vec{x}, t)$ is a complex field over the plane \mathbb{R}^2 . We specify precisely the spatial form of the right hand side of (5.4), by separating the nonlinear term into local and nonlocal parts,

The first two terms on the right represent the linear part of the equation, and we denote them as $\hat{L}(z(\vec{x}), t)$. r is a bifurcation parameter $r > 0$ produces growing solutions which produce exponentially growing solutions whose spatial structure is given by the second term. This is chosen so that if a trial solution (often called an ansatz) of form $e^{\lambda t} e^{i\vec{k}\cdot\vec{x}}$ is substituted in the purely linear part of the equation we obtain the dispersion equation,

$$\lambda(k) = r - (k_c^2 - k^2)^2 \quad (5.7)$$

This is a fourth order equation with a quadratic minimum at $k = 0$ and a quadratic maximum at $k = \pm k_c$. If $r > 0$ then $\lambda(k_c) > 0$ at maximum and patterns with wavelength k_c can grow. As r increases then patterns with a continuous range of k can grow in the case of an infinite domain. In a finite domain the boundary conditions and the domain shape will restrict the patterns to a finite number of k from this range. The eventual state of the patterns is then determined by the form of the local and nonlocal terms. The orientation symmetry described above restricts the nonlinear terms to be of odd degree and

prescribes their form when they are written as functions of z and its complex conjugate \bar{z} . The Volterra series (5.5) is truncated at third order, which is valid very near to the bifurcation.

In the model of (Wolf, 2005b) the nonlinear effects use simple two point correlations between values of $z(\vec{x}), z(\vec{y})$ with the strength of the nonlocal interactions on a point \vec{x} is modelled by an integral with a Gaussian kernel, which respects the rotational symmetry,

$$N_{3NL} = \frac{g_1}{2\pi\sigma^2} \int d^2\vec{y} |z(\vec{y}, t)|^2 z(\vec{x}, t) e^{-\frac{|\vec{y}-\vec{x}|^2}{2\sigma^2}} + \frac{g_2}{2\pi\sigma^2} \int d^2\vec{y} z(\vec{y}, t)^2 \bar{z}(\vec{x}, t) e^{-\frac{|\vec{y}-\vec{x}|^2}{2\sigma^2}} \quad (5.8)$$

Since our main interest is in the effect of the nonlocal terms in establishing stability the local term is modelled simply as

$$N_{3L} = g_0 |z(\vec{x})|^2 z(\vec{x})$$

By considering the effects of translational symmetry and making several simplifying assumptions we can set $g_0 = 1 - g$, $g_1 = 2 - g$, $g_2 = (2 - g)/2$ (see section 5.4.1 for motivation for these choices).

The full equations then become

$$\begin{aligned} \frac{\partial z(\vec{x}, t)}{\partial t} &= rz(\vec{x}, t) - (k_c^2 + \nabla^2(z(\vec{x}, t)))^2 + (1 - g)|z(\vec{x}, t)|^2 z(\vec{x}, t) \\ &- \frac{2 - g}{2\pi\sigma^2} \int d^2\vec{y} |z(\vec{y}, t)|^2 z(\vec{x}, t) e^{-\frac{|\vec{y}-\vec{x}|^2}{2\sigma^2}} \\ &- \frac{2 - g}{4\pi\sigma^2} \int d^2\vec{y} (z(\vec{y}, t))^2 \bar{z}(\vec{x}, t) e^{-\frac{|\vec{y}-\vec{x}|^2}{2\sigma^2}} \end{aligned} \quad (5.9)$$

The parameter g plays an important role in determining the roles that the local and nonlocal terms play in stabilising the solutions. For $1 < g < 2$ the local term is excitatory and the nonlocal terms are inhibitory. This represents what is currently known of the role of neurons close to or far from a given neuron. In terms of producing patterns of sufficient complexity to exhibit pinwheels, (Wolf, 2005b), (Wolf, 2005a) present an analysis in terms of the theory of pattern formation under weak nonlinearities (Manneville, 1990), (Cross and Hohenberg, 1993) to show that stabilisation by the local terms should produced stable solutions which have wavevectors in only two directions (horizontal and vertical), they call these ‘‘essentially non-complex’’ solutions. The biological interest is in solutions with many vectors covering many

directions. If they all have the same wavelength given by the linear term then they will be evenly and densely distributed on the unit circle. Both the weakly nonlinear analysis and the results of simulations in the papers cited produce such solutions when the local terms are excitatory and the nonlocal ones are inhibitory. This weakly nonlinear analysis is discussed in more detail in section 5.4.1.

5.3 Effects of boundary shape

5.3.1 Periodic and noflux boundary conditions

The structure of equation (5.9) is given by the three symmetries described above, as explained in section 5.4.1 below. If the patterns are confined in shape and no-flux boundary conditions are applied so that the shape has a causal effect on the patterns, translational symmetry will be broken. Whether rotational symmetry is broken depends on the shape of the domain, if the domain is circular it will not, if it is polygonal it will. In this section we compare simulations two domains that break symmetries, firstly a circle which breaks translational symmetry and secondly a parallelogram domain which breaks both translational and rotational symmetries. On the parallelogram domain we compare solutions with periodic boundary conditions applied on opposite sides with solutions where noflux boundary conditions are applied on all sides. Strictly speaking, periodic boundary conditions introduce a periodic translational symmetry to replace the translational symmetry defined in Section 5.2.1 above, thus we do not have the full translational symmetry. However since integration on an infinite domain is impossible on a finite computer, this is a commonly used way of integrating without boundary influence and was used in (Wolf, 2005b).

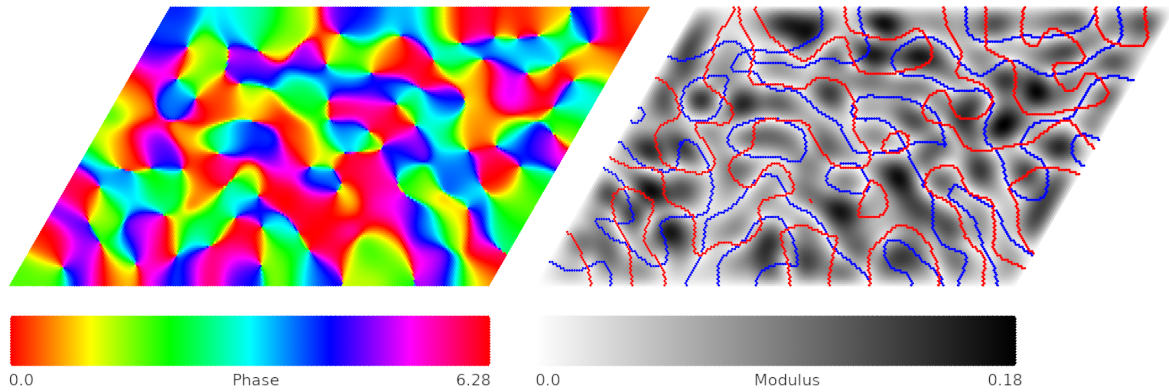
It is very plausible that the wavelength of the patterns relevant to the domain size is important. If the wavelength is large and comparable to the size of the domain then the boundary conditions should have a much bigger influence than if the wavelength is much smaller. The wavelength can be controlled by changing k_c in (5.9). We integrated with three values of k_c in a series where the next value was twice the one before. There are some numerical issues in how to do this which are addressed in section 5.4.1 below, but from a mathematical viewpoint, k_c gives the wavelength just after the first breaking of spatial

homogeneity.

In order to test the effect of the boundary conditions when the wavelengths of the patterns are comparable to, or much less than, the size of the domain we integrated (5.9) on two domains. The first was a parallelogram with both periodic and noflux boundary conditions. The second was a circular domain with no-flux conditions applied at the boundary. We also manipulated k_c in (5.9) to obtain patterns where between 5 and 6 iso-orientation columns could fit into each side, these are called *coarse* patterns. The *fine* patterns has around 16 times this number per side. Comparison of coarse solutions with periodic and noflux boundaries are shown in figures 5.1. Two types of plots were made for each one, on the left is a plot of the phase θ of the field $z = re^{i\theta}$. On the right is the modulus of \vec{x} superimposed on which are the contours of zero real and imaginary field when the field is expressed as $z = z_r + iz_i$. The field strength must be zero at the pinwheel centres or since the only way a point can have multiple orientations is if its modulus is zero, in biological terms it has zero selectivity for any orientation. It can be seen that in the top plot with noflux boundary conditions these contours adjust to intersect the boundary orthogonally. In the lower plots, where periodic boundary conditions are applied this effect is not seen. For example on the right hand edge of the parallelogram it can be seen that one of the contours of zero real field runs parallel to the boundary. This effect is also present in the fine fields of figure 5.2, however it has much less effect on the overall pattern since a smaller fraction of the domain is close to the boundary. The fields in a circular domain, figure 5.3, cannot have periodic boundary conditions applied but the effect of aligning the contours to be orthogonal to the boundary can be seen in both the coarse fields (bottom) and the fine fields (top).

We took $g = 0.98$ for all runs, since this is where (Wolf, 2005b), (Wolf, 2005a) indicated that solutions that had a full distribution of orientations were found. The patterns obtained appear visually similar to those given in (Wolf, 2005b). We did attempt to count the pinwheels and to determine $\hat{\rho}$ in (5.2) using the methods described in (Kaschube et al., 2010), however we found that the pinwheel counts fluctuated with time. This led to the results being unreliable, however (Keil and Wolf, 2011) also report fluctuations over time in $\hat{\rho}$. We return to this issue in section 5.5.

No flux boundary conditions applied to a parallelogram. Left: phase of z . Right: modulus of z



Periodic boundary conditions applied to a parallelogram. Left: phase of z . Right: modulus of z

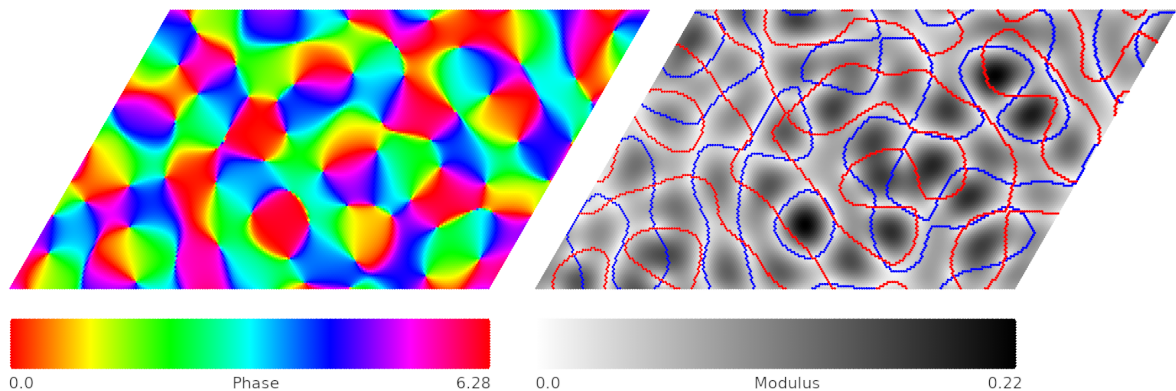


Figure 5.1. Comparison of the solutions of (5.9) in a parallelogram domain with periodic boundary conditions (top plots) and no flux boundary conditions. On the left plots are shown the phase θ of $z = re^{i\theta}$ using a rainbow colour scale from $0, 2\pi$. The black markers are the pinwheel centres. On the right is plotted the modulus r . Superimposed are the lines of zero imaginary value z_i of $z = z_r + iz_i$ in red, while the lines of zero real value z_r are in blue. The top two plots are solutions with no flux boundary conditions. The bottom two plots are solutions with periodic boundary conditions. It can be seen that in the no flux case these contours adapt to intersect the boundary at right angles. In the periodic case this is not seen, indeed the contours of zero real value are actually parallel to the boundary on both the left and right sides. In the phase plots it can be seen that the contours of phase also align at right angles to the boundary, thus the patterns of phase around the boundary are different to those in the centre of the circle. No such difference is observed in the periodic case. The no flux boundary condition causes breaking of translational symmetry, affecting the behaviour of the solutions of (5.9)

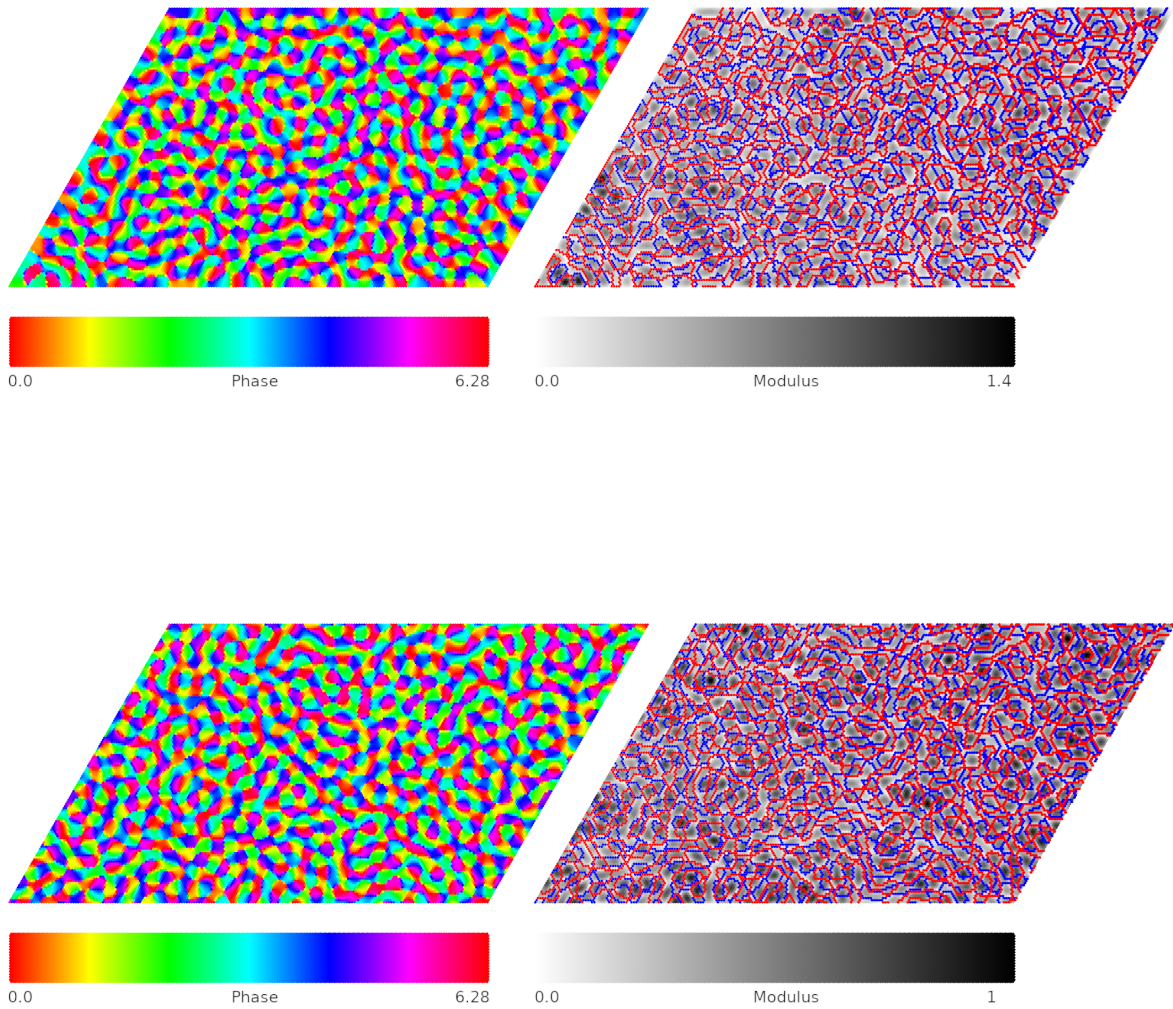
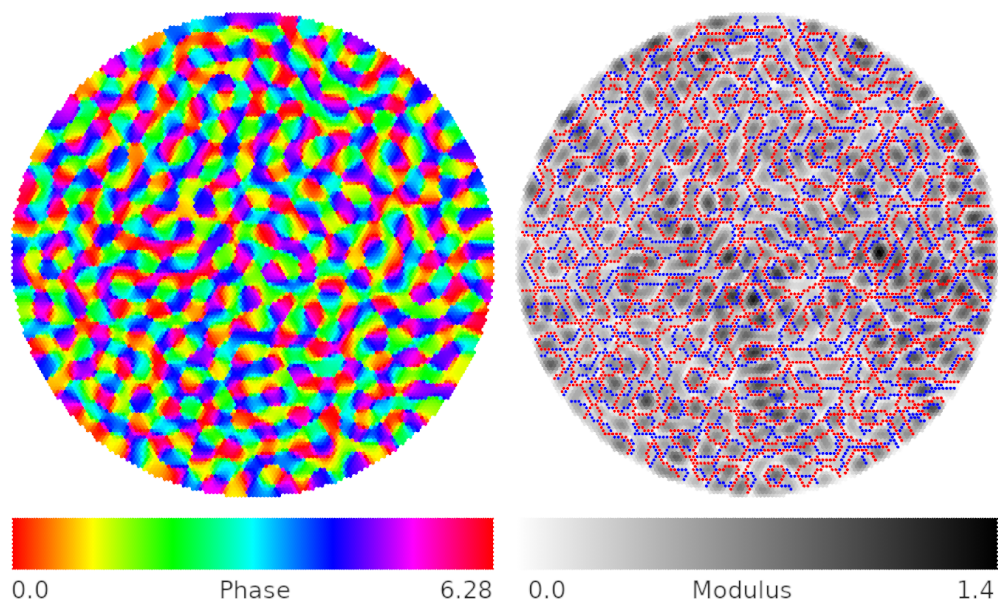


Figure 5.2. Comparison of solutions of (5.9) at the finest level of resolution. All details of the plots are as for figure 5.1. The effect of alignment to the boundary at right angles can still be seen to be present in the circular solutions and absent in the periodic ones. However since the fraction of the region close to the boundary is now much less, the overall appearance of the solutions is not as notably dissimilar as in figure 5.1

Solutions in a circle with no flux boundary conditions, fine resolution



Solutions in a circle with no flux boundary conditions, coarse resolution

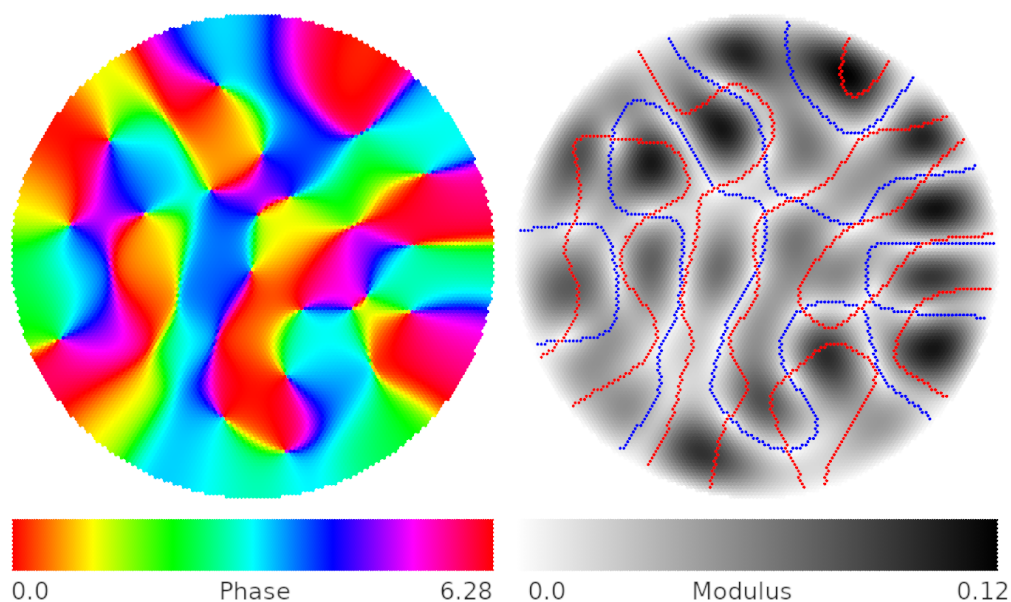


Figure 5.3. Comparison of solutions of (5.9) with no flux boundary conditions applied. The colour maps are the same as in figure 5.1. The effect of alignment to the boundary at right angles is seen to be present in the circular solutions at both levels of resolution. We also performed a similar integration with solutions in a square with no flux boundary conditions with the same result as for the circle and parallelogram. The alignment of the contours of zero real and imaginary parts of the field is a property of the boundary conditions and not of the shape.

5.3.2 Comparison of patterns across boundaries

Pinwheel patterns are seen in regions of the visual cortex that are adjacent but separate regions. This is true of V1 and V2 regions of the cortex. So it is of interest to see if the correlation statistics discussed in chapter 4 will appear in solutions of (5.9). We obtained a spread of correlations by solving in an ensemble of random tessellations and extracting correlations across adjacent edges. We used noflux boundary conditions, since it is not possible to apply periodic boundary conditions to domains that are not regular polygons. There is no need to compare randomly matched edges as our interest here is not in the behaviour of the tessellation but to use it to develop a sufficiently representative sample of correlations of field across edges. We solved for three different wavelengths by adjusting k_c in (5.9). Each value of k_c was twice the value below in the series. Thus the finest fields 4 times as many waves as the coarsest, this is ratio used in section 5.3.1. The longest was longer than the size of the domains, the others had wavelengths which fitted into the domain. We extracted the values of θ and r from the solutions $z = re^{i\theta}$ of (5.9) by the methods outlined in chapter 4.

When the wavelength was greater than the domain size pinwheels cannot form. Several waves must be present for pinwheel formation. In the coarsest solutions shown in figure 5.4 the phase was not able to cover the full range from $0 - 2\pi$. The patterns of phase resemble the fields of the lowest mode of the Keller-Segel equations shown in chapter 4. The fields representing the modulus form elliptical shapes which take their eccentricity from the shape of the boundary. Since r must always be $r \geq 0$ the contours represent maximum field strength in the centre and the lowest field at the boundary. So the field patterns are away from the boundary. There are 20 regions in each tessellation and the dimensions of the whole tessellation are similar to the domains in section 5.3.1. It can be seen that in the finest resolution there are enough waves in each domain to form pinwheel patterns which look visually similar to those in section 5.3.1.

We looked at the statistics of the distributions by the methods of chapter 4, this is shown in figure 5.5. We used the metric α where $\alpha < 0.5$ represented definite evidence of alignment across the boundary, $0.5 < \alpha < 1.0$ meant there could be some weak alignment and with $\alpha > 1$ the correlations tend towards

a random Gaussian distribution centred on the origin, no alignment affects at all. We used 3 resolutions, coarse, medium and fine as described above. At long wavelength the correlations of the pattern of phase have $\alpha = 0.23$ and their visual similarity to the low order patterns in the Keller-Segel equations in chapter 4 is confirmed. and the distribution looks flat. The correlation for the r field is 1.47, this is consistent with all the field structure being internal so there will only be small, uncorrelated fluctuations about zero field on the boundary. For the medium wavelength the value for phase is 0.43, still showing significant correlation. For the modulus the correlation has increased to 2.23. For the finest resolution, where we are getting pinwheels throughout the domain the α value has increased to 1.48, a considerable jump and indicating that correlation across the boundary has been lost. For the modulus field (shown in figure 5.4) we have $\alpha = 3.53$. Both fields increase with increasing complexity of field but ratio from coarsest to finest is 1 : 6.4 and for the modulus it is only 1 : 2.3 and the results are all qualitatively the same, i.e. no correlations whereas there is a qualitative difference in the α values for the phase.

5.4 Materials and Methods

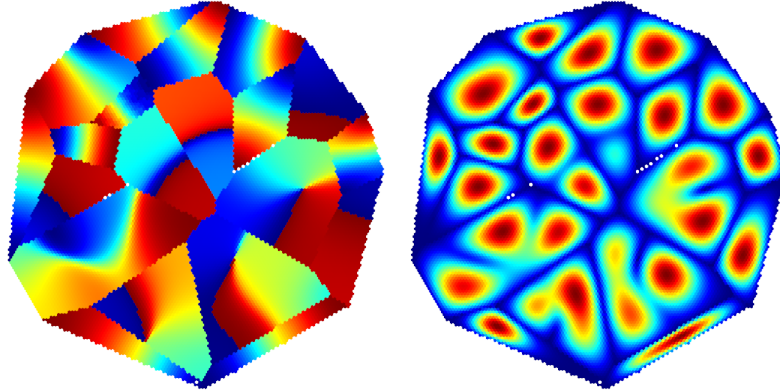
5.4.1 Weakly nonlinear analysis

Here we give the motivation for the form of the terms in (5.9) following the discussion in (Wolf, 2005a) following the principles of weakly nonlinear analysis given in (Manneville, 1990), (Cross and Hohenberg, 1993). We consider solutions very close to the bifurcation where spatial homogeneity is broken, and consider that the amplitudes of the instability will be very small. Note that we can talk of such amplitudes having magnitude because (5.9) is nonlinear. Thus in the Volterra expansion of a dynamical system (5.5) under the orientation symmetry we have only odd terms and will truncate these at third order giving

$$\frac{\partial z(\vec{x})}{\partial t} = \hat{L}(z(\vec{x})) + N_3(z(\vec{x})) \quad (5.10)$$

Where \hat{L} is the linear part written as an operator and the orientation symmetry means that the terms in N_3 are of form $N_3(z, z, \bar{z}$ and all its permutations (here we not not write the dependence on \vec{x} explicitly since the orientation symmetry operates on \mathbb{C}). We then separate the largest eigenvalue of the linear part

Solutions with wavelength greater than the domain diameter. Left: phase. Right: modulus.



Solutions with wavelength much smaller than the domain diameter. Left: phase. Right: modulus.

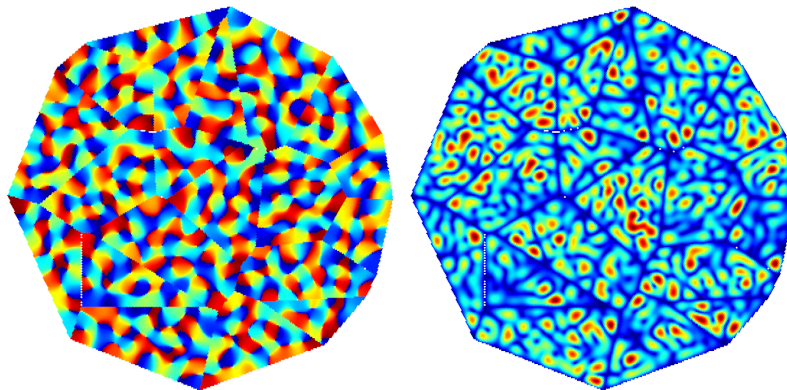


Figure 5.4. Solutions of (5.9) in tessellations with no flux boundary conditions. The left plots show the phase and on the right plots the modulus of the field (see figure 5.1 for details). The top plot shows solutions where the wavelength of the patterns is greater than the size of the region. In this case the pinwheels cannot form and the plots of phase look like the basic mode of the Keller-Segel equations of chapter 4. In all regions the modulus has its greatest value in the centre and lowest at the boundary. The wave characteristics of the field are not evident, in each individual region the phase only occupies a fraction of the full range $0, 2\pi$ thus it is impossible for pinwheels to form. In the bottom plots the basic wavelength is considerably less than the size of the domain and pinwheel centres are observed.

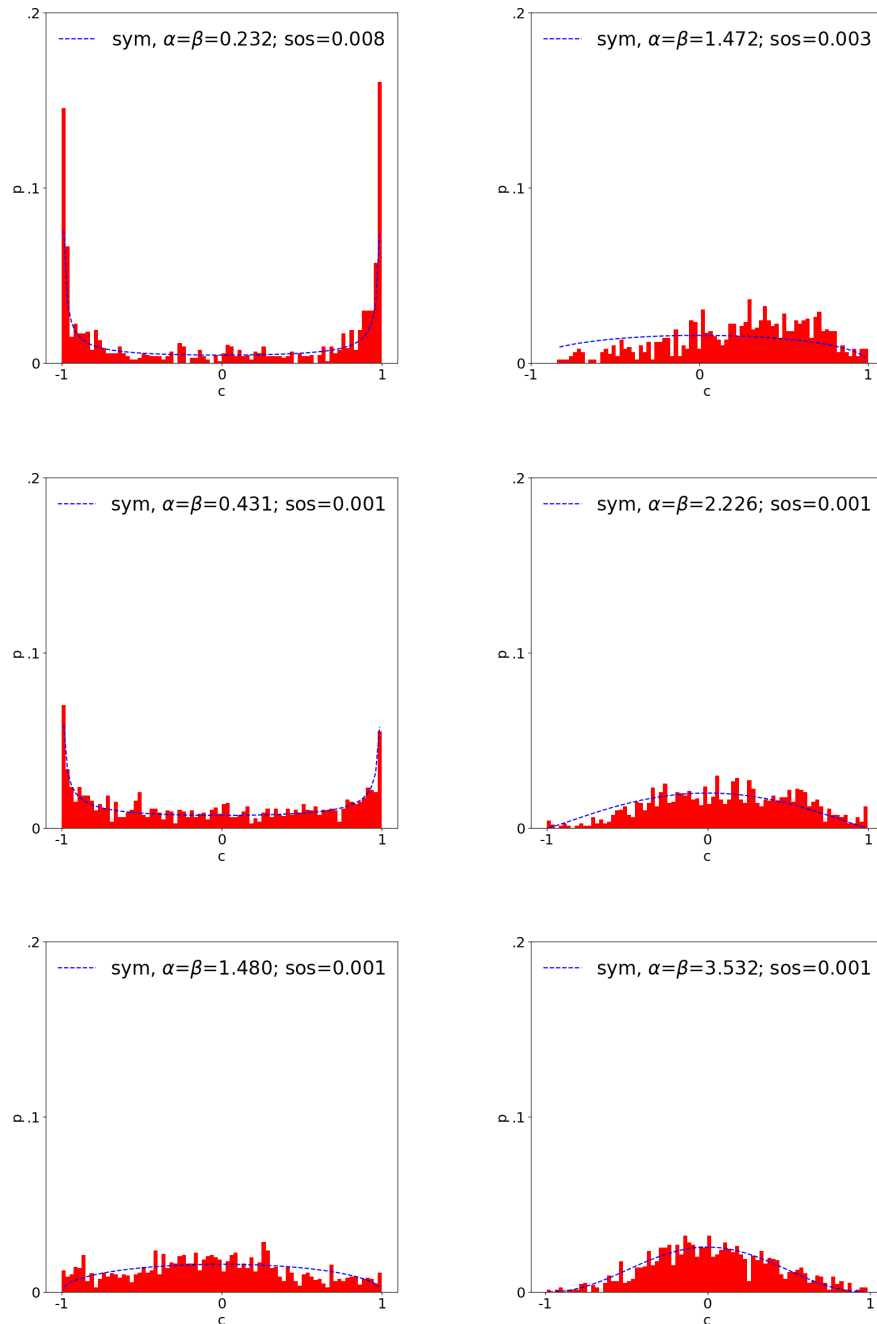


Figure 5.5. Statistics of correlations between adjacent edges of the tessellations, namely the α measure defined in chapter 4. The plots are for three levels of wavelength, for each level half that of the one before, they are described as coarse, medium and fine. The fields corresponding to coarse and fine are shown in figure 5.4. The statistics are being used to determine if there are any alignment effects between fields on either side of an edge. The edges are a basic attempt to model pinwheel fields across different regions of the visual cortex, (V1 and V2), the random tessellation here is just a device to collect sufficient statistics. Different runs with different randomly shaped tessellations were run until at least 100 edge pairs were obtained. The top plot shows the results for the solutions with wavelengths greater than the region size. The middle and bottom plots show solutions with decreasing wavelength but both smaller than the region. Plots on the left shown correlations of phase across the edge, plots on the right show correlations of the modulus. As the wavelength decreases the distribution is converging towards a Gaussian distribution centered on zero. There is a much bigger quantitative and qualitative difference in the statistics for the phase component of the field compared to the modulus component.

to write

$$\hat{L} = r + \hat{L}_0 \quad (5.11)$$

We are considering a bifurcation where the maximum eigenvalue of \hat{L} passes through zero. Since this is a maximum it follows that of \hat{L}^0 has zero eigenvalues.

We now define a scale parameter ϵ so that we can expand r and z as

$$r = r_1\epsilon + r_2\epsilon^2 + r_3\epsilon^3 \quad (5.12)$$

$$z(\vec{x}) = z_1(\vec{x}) + z_2(\vec{x}) + z_3(\vec{x}) \quad (5.13)$$

where we truncate at third order consistent with our level of approximation. Near to the bifurcation point the time evolution scale tends to infinity so we rescale time as $T = rT$. With this time rescaling and using (5.13) in (5.10) we obtain

$$\begin{aligned} 0 = & \epsilon \hat{L}_0(z_1) + \epsilon^2 (\hat{L}_0(z_2) + r_1 z_1 - r_1 \frac{\partial z_1}{\partial T}) \\ & + \epsilon^3 (\hat{L}_0(z_3) + \sum_{i+j=3} r_i z_j + \sum_{i+j=3} r_i \frac{\partial z_j}{\partial T}) + N_3[z_1] \\ & + \epsilon^4 (\dots \\ & \vdots \end{aligned} \quad (5.14)$$

where we again suppress the spatial dependence of z and truncate at third order. $N[z_i]$ is a third order nonlinear term constructed from terms of form $N(z_i, z_i, \bar{z}_i)$ with all permutations of the arguments. We use the construction of \hat{L}_0 to have zero eigenvalue as described above. For (5.14) to hold, the coefficient of each power of ϵ must separately be set to zero. This produces a set of equations of form

$$\hat{L}_0(z_i) = \mathfrak{F}(z_j), \quad j < i \quad (5.15)$$

Since the operator \hat{L}_0 has zero eigenvalues (5.15) cannot be solved unless the right hand side meets a compatibility condition. To obtain this, firstly note that since $\hat{L}_0 : \mathbb{C} \rightarrow \mathbb{C}$ it is self-adjoint, i.e. $\hat{L}_0^\dagger = \hat{L}_0$.

Therefore if we consider the inner product of $\hat{L}_0 z_i$ with an eigenvector w of \hat{L}_0^\dagger that has zero eigenvalue. we obtain,

$$\langle w, \hat{L}_0(z_i) \rangle = \langle \hat{L}_0^\dagger(w), z_i \rangle = 0 \quad (5.16)$$

which combined with (5.15) gives the compatibility condition

$$\langle w, \mathfrak{F}(z_j) \rangle = 0 \quad (5.17)$$

i.e. the right hand side of the coefficients of the powers of ϵ in (5.14) must be orthogonal to the kernel of \hat{L}_0 . This is an application of the theorem known as the Fredholm alternative.

The compatibility condition for the ϵ coefficient simply states that $z_1 \in \ker \hat{L}_0$. The coefficient of ϵ^2 gives

$$\hat{L}_0(z_2) = r_1(z_1 + \frac{\partial z_1}{\partial T}) \quad (5.18)$$

and since $z_1(\vec{x}, T) \in \ker \hat{L}_0$ this can only be satisfied if $r_1 = 0$. The compatibility condition for ϵ^3 gives the lowest order non-trivial dynamics. We define the projection operator $\hat{P}_C : (C) \rightarrow \ker \hat{L}_0$ and using $r_1 = 0$ we obtain,

$$0 = r_2(z_1 + \frac{\partial z_1}{\partial t}) + \hat{P}_C(N_3[z_1]) \quad (5.19)$$

since $\hat{P}_C(z_1) = z_1$ due to $z_1 \in \ker \hat{L}_0$ by the ϵ level compatibility condition. By using (5.19) to define the scale of z_1 , the lowest order term in the expansion of z we can set $r_2 = 1$ and obtain

$$0 = z_1 + \frac{\partial z_1}{\partial t} + \hat{P}_C(N_3[z_1]) \quad (5.20)$$

5.4.2 Amplitude dynamics

(5.20) defines the dynamics of the breaking of spatial homogeneity at length and time scales defined by ϵ giving the behaviour just after the bifurcation point. If the equation is of Swift-Hohenberg form, the space in which this dynamics evolves will be spanned by waves all of which lie on a circle in Fourier space. We can therefore represent z_1 as a *planform* which is a Fourier expansion with a finite number of

terms,

$$z(\vec{x}) = \sum_{j=0}^{j=N} A_j e^{i\vec{k}_j \cdot \vec{x}} \quad (5.21)$$

where the A_j are in general complex and where $|\vec{k}_i| = k_c, \forall i$ and k_c is the radius of the circle of eigenvectors for the solution at the bifurcation point. In the Swift-Hohenberg equation (5.9) k_c appears explicitly but this analysis applies to a wider class of systems. We now project the dynamics of (5.20) onto the \vec{k}_i subspace of $\ker \hat{L}_0$ denoting this projection by the operator \hat{P}_i which commutes with the operators $\frac{\partial}{\partial T}$ and with \hat{P}_C giving

$$\frac{\partial A_i}{\partial t} e^{\vec{k}_i \cdot \vec{x}} = A_i e^{\vec{k}_i \cdot \vec{x}} + \sum_{j,k,l} d_{j-i,k-i,l-i} A_j A_k \bar{A}_l \hat{P}_i N_3 [e^{\vec{k}_j \cdot \vec{x}}, e^{\vec{k}_k \cdot \vec{x}}, e^{\vec{k}_l \cdot \vec{x}}] \quad (5.22)$$

since $\hat{P}_i \hat{P}_C = \hat{P}_i$. This can be rewritten,

$$\frac{\partial A_i}{\partial t} = A_i + \sum_{j,k,l} d_{j-i,k-i,l-i} A_j A_k \bar{A}_l e^{-\vec{k}_i \cdot \vec{x}} \hat{P}_i N_3 [e^{\vec{k}_j \cdot \vec{x}}, e^{\vec{k}_k \cdot \vec{x}}, e^{\vec{k}_l \cdot \vec{x}}] \quad (5.23)$$

since $\hat{P}_i \hat{P}_C = \hat{P}_i$ where the form of the coefficients of the nonlinear terms indicates that only the cyclic differences in terms are important (from rotational We now require that (5.23) be invariant under translational symmetry $\vec{x} \rightarrow \vec{x} + \vec{y}$ for arbitrary \vec{y} . Given the restriction of the form of the nonlinear terms discussed when considering the Volterra series (5.5), we see that the effect of the translational symmetry is to multiply the $N_3[\cdot]$ term by $e^{i(-\vec{k}_i + \vec{k}_j + \vec{k}_k - \vec{k}_l) \cdot \vec{x}}$. and the requirement that the dynamics is invariant to the translation requires

$$0 = -\vec{k}_i + \vec{k}_j + \vec{k}_k - \vec{k}_l \quad (5.24)$$

This is a resonance condition and requires that the four wavevectors form a parallelogram and $-\vec{k}_i, \vec{k}_j, \vec{k}_k, -\vec{k}_l$ form (anti)parallel pairs with the following possible combinations,

$$\begin{aligned} \vec{k}_i &= \vec{k}_j \\ \vec{k}_k &= \vec{k}_l \end{aligned} \quad (5.25)$$

$$\begin{aligned}\vec{k}_i &= \vec{k}_k \\ \vec{k}_j &= \vec{k}_l\end{aligned}\tag{5.26}$$

$$\begin{aligned}\vec{k}_i &= -\vec{k}_l \\ \vec{k}_j &= -\vec{k}_k\end{aligned}\tag{5.27}$$

Substituting into (5.23) we see that there are essentially only two types of amplitude terms $A_j \bar{A}_j A_i$ from (5.25, 5.26) and $A_j A_{j^-} \bar{A}_{i^-}$ where i^- denotes the wave vector antiparallel to that denoted by i , so $k_{i^-} = -k_i$ and (5.28) becomes

$$\frac{\partial A_i}{\partial t} = \lambda A_i - \sum_j g_{ij} |A_j|^2 A_i - \sum_j f_{ij} A_j A_{j^-} \bar{A}_{i^-}\tag{5.28}$$

where

$$g_{ij} = -e^{i\vec{k}_i \cdot \vec{x}} (N_3(e^{i\vec{k}_i \cdot \vec{x}}, e^{i\vec{k}_j \cdot \vec{x}}, e^{-i\vec{k}_j \cdot \vec{x}}) + N_3(e^{i\vec{k}_j \cdot \vec{x}}, e^{i\vec{k}_i \cdot \vec{x}}, e^{-i\vec{k}_j \cdot \vec{x}}))\tag{5.29}$$

and

$$f_{ij} = -\frac{1}{2} e^{i\vec{k}_i \cdot \vec{x}} (N_3(e^{i\vec{k}_j \cdot \vec{x}}, e^{-i\vec{k}_j \cdot \vec{x}}, e^{-i\vec{k}_i \cdot \vec{x}}) + N_3(e^{-i\vec{k}_j \cdot \vec{x}}, e^{i\vec{k}_j \cdot \vec{x}}, e^{i\vec{k}_i \cdot \vec{x}}))\tag{5.30}$$

This can be compared to (5.9). Only the third term on the right can affect the phase at a given point by the convolved effect of nonlocal field values whose phase may be different. The form of the dynamics is given by the form of the nonlinear term N_3 . In (Wolf, 2005a) arguments are given for developing particular forms of g_{ij} and f_{ij} and relating them to the stability of planforms with increasing N . Physically increasing N means that more instabilities with wave vectors satisfying $|\vec{k}| = k_c$ are stable at the bifurcation point. This means that the coverage of different orientations increases. An essential part of the argument, which is summarised in a very condensed form in (Wolf, 2005b), is that unless there is sufficient coverage of the possible orientations registered from the environment onto the retina, the V1 cortex cannot perform its task of recording the structure of the environment for processing by higher levels of the visual pathway.

If the amplitudes are real then $A_{i^-} = \bar{A}_i$ and (5.28) takes the form of the Stuart-Landau equation is

recovered. In the full equations (5.9) convolution with the Gaussian kernel takes the place of summation over indices i, j .

5.4.3 Numerical methods

In devising a numerical scheme to solve (5.9) a major issue is how to deal with the Laplacian terms which are of even order up to fourth order ∇^4 . We use a result due to (Lee et al., 2014) which is described in chapter 2 where the Laplacian ∇^2 can be discretized using a finite volume method without the need to calculate derivatives. To utilise this we write (5.9) as a set of coupled equations, introducing the variable $w := \nabla^2 z$. Since the complex field obeys the same arithmetic rules as the real field and the finite volume method only requires simple arithmetic operations we immediately can apply the same numerical methods as was used for equations with real variables in previous chapters. We obtain

$$w(\vec{x}, t) = \nabla^2 z(\vec{x}, t) \quad (5.31)$$

and

$$\begin{aligned} \frac{\partial z(\vec{x}, t)}{\partial t} &= -2w(\vec{x}, t) - \nabla^2 w(\vec{x}, t) + (r - 1)z(\vec{x}, t) + (1 - g)|z(\vec{x}, t)|^2 z(\vec{x}, t) \\ &- \frac{2 - g}{2\pi\sigma^2} \int d^2\vec{y} \quad |z(\vec{y}, t)|^2 z(\vec{x}, t) e^{-\frac{|\vec{y}-\vec{x}|^2}{2\sigma^2}} \\ &- \frac{2 - g}{4\pi\sigma^2} \int d^2\vec{y} \quad z(\vec{y}, t)^2 z(\vec{x}, t) e^{-\frac{|\vec{y}-\vec{x}|^2}{2\sigma^2}} \end{aligned} \quad (5.32)$$

The time stepping used fourth-order Runge-Kutta solver was used to advance the solutions to a steady state (parameter values were chosen so that all solutions were eventually constant in time, i.e., patterns were stationary). Important numerical details are that in practice w was evaluated as an average of the value on the previous time step and the current value calculated using the values of z from the previous time step. This averaged value was then used in the to advance the z equation. This was for reasons of numerical stability. Also the nonlocal terms are expensive to calculate. The kernel does not depend on z so it was evaluated as a matrix before integration and then multiplied with the z vector over the whole

hexagonal domain as time advanced. Since it was expensive, the matrix multiplication was applied every T timesteps. If T becomes too large then the nonlocal terms cannot stabilise the evolution when the local nonlinearity is excitatory ($g < 1$). For exploratory work $T = 45$ was adequate, to obtain better quality final results we set $T = 15$. We checked that the field structure had stabilised before the integration was considered complete. There is a very slowly growing instability where the field configuration stays the same but the modulus of the maximum field point grows and eventually the solution becomes unstable. It is probable that a more sophisticated analysis of the numerical stability of (5.32) could resolve this, but since the field configuration is steady for a long time before this is an issue we did not investigate further but found we could control it by adjusting T . In (Wolf, 2005b) the criterion for considering that a steady state had been reached was not discussed.

Simulations were written in C++ with the help of the support library *morphologica* (James and Wilson, 2021) (see also (James et al., 2020)). We verified that all simulation results reported were insensitive to the choice of spatial discretization (i.e., to the lattice density). A hexagon-to-hexagon distance of $O(10^{-3})$ on a domain whose spatial scale was normalized to be $O(10^0)$ was found to be sufficient. At this scale, the domain contained $O(10^4)$ hexagonal grid-points, some runs were made with a hex-to-hex distance that was halved to check that resolution was sufficient.

5.5 Discussion

We have compared solutions of the Swift-Hohenberg equations with periodic and noflux boundary conditions. As discussed the noflux boundary conditions break the Euclidean plane symmetries used in much theoretical analysis and most simulation studies have also used such conditions or have only reported on fields away from the boundary. However (Keil and Wolf, 2011) examined the effects of nonperiodic boundary conditions in elastic net model. (Wolf and Geisel, 1998) used an elastic net model to study pinwheel formation and annihilation. Later Wolf and co-workers developed the global optimisation model discussed above and derived conditions of the formation of quasiperiodic fields of phase which gave the universal pinwheel density measure $\hat{\rho} = \pi$. (Kaschube et al., 2010) presented evidence that this measure

could be observed across a range of mammalian species which were widely separated on the mammalian evolutionary tree. (Keil and Wolf, 2011) examined elastic net models in considerable detail. In their Figure 28 the comparison of periodic and nonperiodic boundary conditions on the phase of the field and on the retinotopic perturbations are shown. The nonperiodic boundary conditions have a big effect on the retinotopic perturbations, these are almost completely absent in the periodic case. As a consequence, in the periodic boundary solutions the field relaxes to stripes which have a $\hat{\rho}$ value well below π whereas for the non-periodic boundary conditions the field retained a quasiperiodic structure and $\hat{\rho}$ was close to π . By contrast in the solutions of the Swift-Hohenberg equations we found that that the effects of the boundary were only apparent close to the boundary by the orientation of the contours of zero real and imaginary components of the field to be orthogonal to the boundary. Keil and Wolf (2011) also show evidence that the value of $\hat{\rho}$ can show oscillations as the solutions advance in time, see their Figure 13b. We also found evidence of such oscillations but did not examine them in sufficient detail to comment further.

The most novel feature of the work presented here (section 5.3.2) was the use of the α measure of correlation across boundaries of different region that are separated physically but can “communicate” via the geometric structure of the tessellation as discussed in chapter 4. We found that this effect was particularly strongly observed in the field of phase, which represents in our models the map of orientation preferences across the cortex. While the results presented here are preliminary they suggest the interesting possibility that the appearance of pinwheels changes the structure of the field to being determined by the boundary and therefore by the shape of the domain, to a structure that is determined by the pinwheels. This latter structure could be influenced primarily by the symmetries of the Euclidean plane and be insensitive to the actual shape of the domain in which the pinwheels appear.

Chapter 6

The effects of geometry and dynamics on biological pattern formation

6.1 Review of research question

The fundamental research question posed in this thesis is "How can we evaluate the effects on pattern formation caused by the shape of the domain in which the patterns form and dynamical constraints on the process." The risk in posing this question is that the effects may be minor. For example patterns which appear in perfectly circular domains might be distorted when in differently shaped domains but not in any fundamental way different. Also changes to the dynamics such as changes in the initial conditions or by applying constraints such as a low occupancy requirement for patterns might have a minor effect. The initial conditions might be quickly "forgotten" by the action of diffusive processes, the dynamical constraints likewise might not fundamentally change the pattern forming process, just as shape might not.

Instead it was found that both types of influence, geometric and dynamical have profound and surprising effects, that could not be predicted from the theory of linear pattern breaking instability. We now review the major results from chapters 3, 4 and 5 that support this conclusion.

In chapter 3 an experiment was performed where simulations of the Keller-Segel equations were performed in a collection of identical squares with three different types of initial conditions which took a uniformly randomly distributed field and made some perturbations of it near to the boundary. Three qualitatively different types of solution were obtained.

In the same chapter it was shown that a dynamical constraint of low occupancy caused some types of solution that would be expected from the linear results and the simulation of the nonlinear equations without this constant became unstable, in the sense that their structure retreats from the whole region of the barrel and can only be seen as perturbations of the walls of stomata (septae) that separate the regions of the tessellation.

Taken together these two effects can provide an alternative explanation of the patterns observed in the rat barrel cortex. It is shown that the linear theory, which explains the appearance of different patterns purely in terms of domain size, would not explain why the full range of patterns appears even though the spread in sizes of the first four rows of the barrel tessellation is much too small. Moreover, intermediate patterns which should be also seen given the range of barrel sizes are not observed. The alternative explanation that emerges from this work is that the polygonal structure of the regions of the tessellation promotes patterns which spread in rays to the boundary. The low occupancy requirement causes these rays to be unstable so only patterns formed of a few rays, mainly one or two but occasionally three, are observed. Such ray-like patterns can also be observed in the markings inside the regions formed by the tessellated pattern on the giraffe's pelt.

In chapter 4 another effect is confirmed which had not been predicted from previous work on pattern formation, namely that patterns which evolve in a tessellation and are subject to the constraints of noflux boundary conditions have a much higher degree of alignment compared with patterns that evolve in domains of exactly the same shapes as those in the tessellation but where any possible effects of the tessellation structure have been removed. These results are surprising because the boundary conditions ensure that there is no possible physical influence that can align the patterns. It might be thought that perhaps the discretization caused the boundary conditions to be imperfectly implemented. However this

would cause a preponderance of positive correlations. Instead we observed a symmetrically bimodal distribution of positive and negative correlations.

We have been able to understand and analyse this geometrically determined alignment by normalising the vectors of field values across boundaries. In this way we equate the problem to examining the distribution of correlations in terms of the distribution of points on a hypersphere. There exists a considerable body of mathematically proven results about this and we use this to derive an analytical discriminator which can determine if the boundaries have been causal to the development of the patterns. This is shown for a wide class of tessellations ranging from regular tessellations of triangles to Voronoi tessellations formed from points randomly distributed in a region, called random tessellations for shorthand.

Finally this alignment to the boundaries was also shown in a different type of pattern formation, namely a feature mapping of visual input to response of cortical neurons. Unlike with the subbarrel patterns where pattern of physical neuron stomata are formed, the orientation preference columns of the V1 and V2 cortex are patterns of neuron response to particular features of the input from the eyes, namely the orientation of regions of dark and light in the visual field. Previous modelling of these pinwheel patterns has assumed that they develop on regions which are boundariless, either by assuming the symmetry of the full Euclidean group or by applying periodic boundary conditions to a domain used for numerical simulation.

6.2 Implications for biology

Darwin said "How odd it is that anyone should not see that an observation must be for or against some view if it is to be of service." In the case of the subbarrel patterns in the rat cortex very little has been published since the original papers that established their form and existence in 2005-6 and the theoretical insight that they resembled certain modes of the Bessel functions and could therefore be produced by processes of the reaction-diffusion type, as spatial bifurcations in the solution of partial differential equations. In the absence of alternative viewpoints it is hard to see how further investigations might proceed. The work presented here provides an alternative explanation for the patterns. It also highlights

certain gaps between modelling and observation that could provide clues for a better understanding of the process of pattern formation and a reexamination of the methodology of classifying the patterns. Our very preliminary comparison of these patterns with those seen in the subregion patterns of the giraffe could be an avenue. The models developed in this thesis predict the existence of patterns which have only a single ray from the centre to the boundary, these can be clearly seen in the giraffe but they are not reported from the observations of the barrel cortex. However the methodology adopted in the original papers, namely that only patterns which divided the barrel into two or more regions were counted would preclude recording such uniray patterns.

The work presented in chapter 4 demonstrates the existence of a process of alignment of patterns in neighbouring regions without communication and presents evidence that this is not specific to a particular type of tessellation, but is a general property. In this chapter we make some suggestions for biological implications in terms of providing routes for transport of fluids or the ability to coordinate processing of stimuli that occur across the whisker pad. In the context the original papers (Land and Erickson, 2005), (Louderback et al., 2006) noted that their four patterns did not seem to appear in the same places in the rows and arcs, apart from a preponderance of the coffeebean (CB) pattern in row A. We have shown that the pattern alignment is between patterns across edges rather than whole patterns and in this context it may be significant that the processing in the regions of a barrel next to the boundary tend to be more to do with processing stimuli that excite neuronal response in multiple barrels. Again, our model results suggest new avenues for experimental exploration. In terms of the spandrels argument of (Gould and Lewontin, 1979) discussed in chapter 1 these alignments arise from engineering constraints in the developing organ. However given the adaptation pressures to utilise such effects it is likely that the existence of pattern alignment will be utilised for improving the fitness of the organism.

In chapter 3 we present evidence for the important role of chance in the development of patterns. Slight changes in the initial conditions can produce solutions which are qualitatively different. We have not investigated using a noisy term in the equations so that chance events influence throughout development, nor of randomising the external signals which were shown to influence development. In this context, just as this thesis was being finalised, the New Scientist of September 22 2022 had a cover article reporting

recent research that suggest that random events during development can be responsible for a considerable amount of the variance between individuals in terms of certain traits such as intelligence, comparable to the influence of the environment. In experiments on organisms such as fruit flies it has been shown that chance events in development cause different amounts of asymmetry in their brains. This is very different from the role played by random mutations that are important in the evolution of the genotype, they influence the development of the phenotype. It might be thought that to say that differences between individuals will be produced by chance events is obvious and uninteresting but the extent of the influence is suggested to be far beyond what has been considered before. It would appear that development is sensitive and has memory which does not get erased with time. This is what the results of chapter 3 show and they have bearing on this new direction of research in development.

6.3 Implications for mathematics

The work presented here has all been towards the reproduction of patterns that do not develop in time. There are two major ways to produce such patterns in mathematical models based on partial differential equations. One is to model the system as elliptical equations of the form

$$F(\vec{z}, \frac{\partial \vec{z}}{\partial \vec{x}}) = 0 \quad (6.1)$$

where \vec{z} represents the field and $\frac{\partial \vec{z}}{\partial \vec{x}}$ represents its derivatives up to a particular order. In the diffusion related problems studied here this order is usually even and in the example equations studied in this work it is 2 or 4.

An alternative approach is to model the system as a dynamical system

$$\frac{\partial \vec{z}}{\partial t} = F(\vec{z}, \frac{\partial \vec{z}}{\partial \vec{x}}) \quad (6.2)$$

and evolve it forward in time until a time-steady state is reached (or not!). The elliptical equation (6.1) can often be solved by deriving F from a higher order potential and minimising this potential gives

the system of elliptical equations. A classic example is deriving a system of equations representing static equilibrium of a system of forces that are derived from a potential that represents the energy of the system. Minimising the energy potential produces the equations for the forces, this is known in mechanics as d'Alembert's principle. In this example there are no derivatives in the system of equations but the same considerations apply when they are present. The work of (Wolf, 2005b), (Wolf, 2005a) represents pinwheel development as an optimisation process and this helps to inform the structure of the equations developed. The existence of a minimisation problem gives the approach of modelling by elliptical equations an elegance and analytical tractability that can produce deep insights into the pattern forming process.

By contrast the approach adopted in this thesis, that of numerically integrating equations of form (6.2) until a steady state is reached can be unkindly compared to understanding the causes of an incidence of car crashes on a mountain bend by driving a fleet of cars round it rather than by analysing the shape of the bend and the limits of traction of the tyres under different road conditions. In chapters 3, 4 we address this by developing metrics that can look at deeper properties of the patterns and conducting numerical experiments that isolate the effect of particular terms in the equations, for example the difference in behavior of the Keller-Segel terms when the diffusion parameter D_n is varied, compared with when the chemotaxis parameter χ is varied.

One major advantage of the dynamical systems method (6.2) is that it can be applied when there are many multistable solutions all of which can fit the boundary conditions of the domain. In this situation the initial conditions and chance events in development can have a major influence on the final state. Also we can observe the evolution of the patterns which is often a key interest in biology. None of these things can be explored by the elliptical equations approach which only considers a final state. Moreover in complex and irregular domains many of the advantages of elegance and analytical tractability are lost.

We have attempted to move towards a formalism that can address such issues by conceptualising the

development of the solutions via a series of states, to recapitulate (2.21)

$$H \rightarrow C \rightarrow S^1 \quad (6.3)$$

where H is the space of random fields at a very fine level of resolution S^1 is the final state, governed by some symmetry group and C is a space of intermediate states which develop rapidly from the randomness of H to length scales comparable to the domain. C gives a wide range of routes to eventual states and can explain why even at the same parameter values, solutions of different form can stabilise.

6.4 Future work

The correlation statistics of chapter 4 apply only to comparisons of the parts of the pattern close to the boundary. An unanswered question is: what implications, if any, does this have for any possible alignment of the full patterns in the region? Clearly such alignment will have to adjust to the alignment of the edges of the region to neighbouring regions, but is there some form of integration of the effects that produces alignment of whole pattern shapes?

Another area of interest is the finding that the solutions of the Keller-Segel equations show alignment effects but the solutions of the Swift-Hohenberg equations modelling feature maps of orientation preference do not. This could be because the presence of the topological singularities is more important in organising the field than are the boundary shapes. It would be of interest to see if this difference could be confirmed in other classes of systems.

It would also be of interest to see if the edge alignment effects occur in wider classes of pattern forming dynamical systems. We have modelled systems described by partial differential equations which require smoothness in the distribution of field variables, for example we do not model neurons or even columns of neurons, but densities of neurons. But development can be modelled by agent based methods where single neurons or collections of neurons are modelled by a discrete agent with rules for how it interacts with other agents. Also, as we move from modelling patterns based on actual physical structure to

patterns of neuronal response, there is even less reason to assume continuity or that partial differential equations are the best modelling approach. Models that use principles of learning and are built on dynamics of different interacting layers representing different processing stages between the environment and the cortex have shown that they can reproduce response structure such as pinwheels (Stevens et al., 2013) Numerical experiments could test if phenomena such as geometric alignment of patterns, and sensitivity of patterns to chance events in development are seen in these models also.

The results of chapter 3 suggest that the patterns in images of the rat cortex should be reexamined to see if the original methods of classification by considering the number of subregions that the patterns produce may have biased the results. Only 25% of the total number of barrels examined were counted in the final statistics. If the original classification is shown to account for all patterns observed is upheld then this is a problem for models that explain the development of patterns as dynamical instabilities within the barrel region because it is hard to see how only those patterns are observed and not other patterns equally likely to be excited. Also, if it is shown that subbarrel patterns are only seen in arcs 1-4 of the rat PMBSF then this is also a problem for such models since other barrels in the PMBSF are very similar in shape and size to those in arcs 1-4. Even if proved wrong, models such as (Ermentrout et al., 2009) and the adaptation of it presented here will serve a useful purpose because they indicate that more investigation of the effects of interactions between developing patterns in the thalamus and cortex need to be investigated and modelled. These models also suggest that comparative studies between subbarrel patterns and subregion patterns in other biological contexts, such as patterns on the skin would be fruitful. Are there universal aspects of such pattern formation? The model developed in this thesis suggests there are and gives predictions sufficiently specific to be potentially falsifiable by such a comparative study so it would be a good starting point for such research.

In terms of mathematical research, in chapter 4 developed a correspondence between the analysis of pattern alignment across edges of a tessellation with the analysis of distributions of unit vectors on a hypersphere. Given that a considerable amount of research interest and development is going into the latter, while the former is in its infancy, exploring this correspondence further would seem to be very fruitful. Pattern alignment across a wider range of tessellations could be explored, for example random

tessellations that are not Voronoi, e.g. can have long narrow shapes, could be included. There is interest in Voronoi tessellations in non-Euclidean geometries, for example hyperbolic geometry. The methods developed in this thesis could be adapted to such geometries. Also, in this work we have examined alignment of patterns that are stationary in time, but dynamical systems with time varying solutions could be examined to see if spatiotemporal correlations could be studied. This would be equivalent to studying dynamical systems on hyperspheres.

In terms of numerical methods, all numerical solutions in this work were evolved on a hexagonal grid. A key decision was to use the finite volume method for discretizing the Laplacian operator developed by (Lee et al., 2014). This extended very naturally to discretizing the hyperdiffusion operator ∇^4 for complex fields in chapter 5. Hexagonal grids have advantages for image processing and digitisation which are related to the study of pattern formation. It has been shown that methods based on hexagonal meshes can be more efficient in terms of image storage to a given resolution compared to methods based on Cartesian meshes. This advantage is related to the property that all centres of a hexagonal mesh are equidistant, this property is also behind the very simple form for the Laplacian operator. One problem that has held back methods on hexagonal grids has been the lack of an equivalent for the fast Fourier transform. The technical difficulty here is that the directions in a hexagonal grid are not orthogonal. However a method based on two overlapping hexagonal grids to represent a single one has recently resolved this difficulty. Given the links between Fourier analysis and the Laplacian operator, it would be worth investigating how the equations solved here could be transferred to Fourier space and comparisons of efficiency between this and the solution on the space domain could be of interest in numerical analysis.

References

- Abramowitz, M. and Stegun, I. (1970). *Handbook of mathematical functions*. Dover, 9 edition.
- Adler, R. and Taylor, J. (2007). *Random fields and geometry*. Springer.
- Afgoustidis (2015). Monochromaticity of orientation maps in V1 implies minimum variance for hyper-column size. *The Journal of Mathematical Neuroscience*, 5:1–20.
- Ames, W. (1977). *Numerical methods for partial differential equations*. Academic Press.
- Andermann, M. L. and Moore, C. I. (2006). A somatotopic map of vibrissa motion direction within a barrel column. *Nat Neurosci*, 9(4):543–551.
- Anderson, T. W. (2009). *An Introduction to multivariate statistical analysis*. John Wiley and Sons, London.
- Asllani, M., Busiello, D. M., Carletti, T., Fanelli, D., and Planchon, G. (2014). Turing patterns in multiplex networks. *Phys. Rev. E*, 90:042814.
- Bard, J. B. (1981). A model for generating aspects of zebra and other mammalian coat patterns. *Journal of Theoretical Biology*, 93(2):363–385.
- Bednar, J. and Wilson, S. (2016). Cortical maps. *The Neuroscientist*, 22(6):604–617:604–617.
- Bednar, J. A. and Miikkulainen, R. (2006). Joint maps for orientation, eye, and direction preference in a self-organizing model of V1. *Neurocomputing*, 69(10):1272 – 1276. Computational Neuroscience: Trends in Research 2006.

- Blaussius, B. and Stone, L. (2000). Nonlinearity and the Moran effect. *Nature*, 400(6798):846–7.
- Bonhoeffer, T. and Grinvald, A. (1991). Iso-orientation domains in cat visual cortex are arranged in pinwheel-like patterns. *Nature*, 353:429–431.
- Brooke, J. M., James, S. S., Jimenez-Rodriguez, A., and Wilson, S. P. (2022). Biological action at a distance: Correlated pattern formation in adjacent tessellation domains without communication. *PLoS Computational Biology*, 18(3):e1009963–e1009963.
- Bruno, R. M., Khatri, V., Land, P. W., and Simons, D. J. (2003). Thalamocortical angular tuning domains within individual barrels of rat somatosensory cortex. *J Neurosci*, 23(29):9565–9574.
- Caro, T., Argueta, Y., Briolat, E., Bruggink, J., Kasprovsky, M., and Lake, J. (2019). Benefits of zebra stripes: Behaviour of tabanid flies around zebras and horses. *PLoS ONE*, 14:e0210831.
- Constantine-Paton, M. and Law, M. I. (1978). Eye-specific termination bands in the tecta of three-eyed frogs. *Science*, 202:639–641.
- Crampin, E. J., Gaffney, E. A., and Maini, P. K. (1999). Reaction and diffusion on growing domains: Scenarios for robust pattern formation. *Bulletin of Mathematical Biology*, 61(6):1093–1120.
- Crank, J. (1975). *The Mathematics of Diffusion*. Clarendon Press Oxford.
- Cross, M. and Hohenberg, P. (1993). Pattern formation outside of equilibrium. *Reviews in Modern Physics*, page 851.
- Durbin, R. and Mitchison, G. (1990). A dimension reduction framework for understanding cortical maps. *Nature (London)*, 343(6259):644–647.
- Ermentrout, G., Simons, D., and Land, P. (2009). Subbarrel patterns in somatosensory cortical barrels can emerge from local dynamical instabilities. *PLOS Computational Biology*, 10(10):e1000537.
- Gierer, A. and Meinhardt, H. (1972). A theory of biological pattern formation. *Kybernetik*, pages 30–39.

- Golubitsky, M. and Stewart, I. (2002). *The symmetry perspective: from equilibrium to chaos in phase space and physical space*. Birkhauser.
- Gomez, D., Iyaniwura, S., Panquin-Lefebvre, F., and Ward, M. (2021). Pattern forming systems coupling linear bulk diffusion to dynamically active membranes or cells. *Philosophical Transactions of the Royal Society A*, page 20200276.
- Goodwin, B. C. and Kauffman, S. A. (1990). Spatial harmonics and pattern specification in early *Drosophila* development. part i. bifurcation sequences and gene expression. *Journal of Theoretical Biology*, 144(3):303 – 319.
- Gould, S. J. and Lewontin, R. C. (1979). The spandrels of San Marco and the Panglossian paradigm: a critique of the adaptationist programme. *Proc. R. Soc. of London: Series B*, 205:581–598.
- Green, J. B. A. and Sharpe, J. (2020). Positional information and reaction diffusion: two big ideas in developmental biology combine. *Development*, 142:1203–1211.
- Gómez-Gálvez, P., Vicente-Munuera, P., Tagua, A., and et al. (2018). Scutoids are a geometrical solution to three-dimensional packing of epithelia. *Nat Commun*, 9:2960.
- Honda, H. (1978). Description of cellular patterns by Dirichlet domains; the two-dimensional case. *Journal of Theoretical Biology*, 72:523–543.
- Honda, H. (1983). Geometrical models for cells in tissues. *International Review of Cytology*, 81:191–248.
- Hubel, D. and Wiesel, T. (1959). Receptive fields of single neurones in the cat's striate cortex. *Journal of Physiology*, 148:574–591.
- Hubel, D. and Wiesel, T. (1962). Receptive fields, binocular interaction and functional architecture in the cat's visual cortex. *Journal of Physiology*, 160:106–154.
- Hubel, D. and Wiesel, T. (1963). Shape and arrangement of columns in the cat's striate cortex. *Journal of Physiology*, 165:559–568.

- Iserles, A. (2009). *A first course in the numerical analysis of differential equations*. Cambridge University Press.
- Issa, N. P., Rosenberg, A., and Husson, T. R. (2008). Models and measurements of functional maps in V1. *J Neurophysiol*, 99(6):2745–2754.
- Izhikevich, E. M. and Hoppensteadt, F. C. (2009). Polychronous wavefront computations. *International Journal of Bifurcation and Chaos*, 19:1733–1739.
- Jacob, V., Cam, J. L., Ego-Stengel, V., and Shulz, D. E. (2008). Emergent properties of tactile scenes selectively activate barrel cortex neurons. *Neuron*, 60(6):1112–1125.
- James, S. and Wilson, S. (2021). morphologica. RRID: SCR_018813.
- James, S. S., Krubitzer, L. A., and Wilson, S. P. (2020). Modelling the emergence of whisker barrels. *eLife*, 9.
- Jeffress, L. A. (1948). A place theory of sound localization. *J Comp Physiol Psychol*, 41(1):35–39.
- Jung, C.-Y., Park, E., and Temam, R. (2017). Boundary layer analysis of nonlinear reaction–diffusion equations in a polygonal domain. *Nonlinear Analysis: Theory, Methods & Applications*, 148:161–202.
- Kaschube, M., Schnabel, M., Löwel, S., Coppola, D. M., White, L. E., and Wolf, F. (2010). Universality in the evolution of orientation columns in the visual cortex. *Science*, 330(6007):1113–1116.
- Kauffman, S. (2020). Answering Schrödinger’s “What is Life?”. *Entropy*, 22:815.
- Kauffman, S. A. (1993). *The Origins of Order: Self-Organization and Selection in Evolution*. Oxford University Press.
- Kauffman, S. A. (2019). *A world beyond physics: The emergence and evolution of life*. Oxford University Press.
- Kauffman, S. A. and Goodwin, B. C. (1990). Spatial harmonics and pattern specification in early

- Drosophila development. part ii. the four colour wheels model. *Journal of Theoretical Biology*, 144(3):321 – 345.
- Keil, W. and Wolf, F. (2011). Coverage, continuity and visual cortical architecture. *Neural systems and circuits*, 1(17):1–55.
- Keller, E. and Segel, L. (1971). Model for chemotaxis. *Journal of Theoretical Biology*, 30:225–234.
- Kida, H., Shimegi, S., and Sato, H. (2005). Similarity of direction tuning among responses to stimulation of different whiskers in neurons of rat barrel cortex. *J Neurophysiol*, 94(3):2004–2018.
- Koch, A. J. and Meinhardt, H. (1994). Biological pattern formation : from basic mechanisms to complex structures. *Rev. Modern Physics*, 66:1481–1507.
- Krause, A., Gaffney, E., Maini, P., and Klika, V. (2021a). Modern perspectives on near-equilibrium analysis of Turing systems. *Philosophical Transactions of the Royal Society A*, page 20200268.
- Krause, A., Gaffney, E., Maini, P., Klika, V., and Eds. (2021b). Introduction to ‘recent progress and open frontiers in Turing’s theory of morphogenesis.’. *Philosophical Transactions of the Royal Society A*, page 2020280.
- Krause, A. L., Burton, A. M., Fadai, N. T., and Van Gorder, R. A. (2018). Emergent structures in reaction-advection-diffusion systems on a sphere. *Phys. Rev. E*, 97:042215.
- Krause, A. L., Klika, V., Maini, P. K., Headon, D., and Gaffney, E. A. (2021c). Isolating patterns in open reaction-diffusion systems. *Bulletin of Mathematical Biology*, 83:1–35.
- Kremer, Y., Léger, J.-F., Goodman, D., Brette, R., and Bourdieu, L. (2011). Late emergence of the vibrissa direction selectivity map in the rat barrel cortex. *J Neurosci*, 31(29):10689–10700.
- Krubitzer, L. and Dooley, J. C. (2013). Cortical plasticity within and across lifetimes: how can development inform us about phenotypic transitions. *Frontiers in Human Neuroscience*, 7:620.
- Land, P. and Erickson, S. (2005). Subbarrel patterns of thalamocortical innervation in rat somatosensory cortical barrels. *Journal of Computational Neurology*, 490:414–426.

- Lee, D., Tien, H., Luo, C., and Luk, H. N. (2014). Hexagonal grid methods with applications to partial differential equations. *International Journal of Computer Mathematics*, 91(9):1986–2009.
- Louderback, K., Glass, C., Shamalla-Hannah, L., Erickson, S., and Land, P. (2006). Subbarel patterns of thalamocortical innervation in rat somatosensory cortical barrels: Organization and postnatal development. *Journal of Comparative Neurology*, 497(1):32–41.
- Manger, P., Sum, M., Szymanski, M., Ridgway, S., and Krubitzer, L. (1998). Modular subdivisions of dolphin insular cortex: Does evolutionary history repeat itself? *Journal of Cognitive Neuroscience*, 10:153–166.
- Manneville, P. (1990). *Dissipative structures and weak turbulence*. Academic Press.
- Maturana, H. and Varela, F. (1980). *Autopoiesis and Cognition: The Realization of the Living*. D Reidel Publishing Company.
- Miikkulainen, R., Bednar, J. A., Choe, Y., and Sirosh, J. (2005). *Computational maps in the visual cortex*. Springer, Berlin.
- Mitchell, G. and Skinner, J. D. (2004). Giraffe thermoregulation: a review. *Transactions of the Royal Society of South Africa*, 59:109–118.
- Montévil, M. and Mossio, M. (2015). Biological organisation as closure of constraints. *J. Theoretical Biology*, 7:179–191.
- Montévil, M., Mossio, M., Pocheville, A., and Longo, G. (2016). Theoretical principles for biology: Variation. *Progress in Biophysics and Molecular Biology*, 122(1):36–50.
- Moran, P. (1953). The statistical analysis of the Canadian lynx cycle. II. Synchronization and meteorology. *Australian J. of Zoology*, 1:291–298.
- Morse, P. M. and Feshbach, H. (1953). *Methods of Theoretical Physics Vol. 1*. McGraw-Hill.
- Mossio, M., Montévil, M., and Longo, G. (2016). Theoretical principles for biology: Organization. *Progress in Biophysics and Molecular Biology*, 122(1):24–35.

- Muolo, R., Asllani, M., Fanelli, D., Maini, P. K., and Carletti, T. (2019). Patterns of non-normality in networked systems. *Journal of theoretical biology*, 480:81–91.
- Murray, J. D. (1984). *Mathematical Biology I: First Edition*. Springer.
- Murray, J. D. (1989). *Mathematical Biology II: First edition*. Springer.
- Murray, J. D. (1993). *Mathematical Biology I: Second Edition*. Springer.
- Othmer, H. and Scriven, L. (1971). Instability and dynamic pattern in cellular networks. *Journal of Theoretical Biology*, 32(3):507–537.
- Petkov, C. I., Kaye, C., Augath, M., and Logothetis, N. K. (2006). Functional imaging reveals numerous fields in the monkey auditory cortex. *PLOS Biology*, 4:e215.
- Press, W. H., Teukolsky, S. A., Vetterling, W. T., and Flannery, B. P. (2007). *Numerical Recipes (C++ version)*. Cambridge University Press.
- Prigogine, I. and Stengers, I. (1984). *Order out of chaos*. Flamingo.
- Purves, D., Riddle, D., and LaMantia, A.-S. (1992). Iterated patterns of brain circuitry (or how the cortex gets its spots). *Trends in Neuroscience*, 15:362–368.
- Rall, R. (1996). *The Shape of Life: Genes, Development, and the Evolution of Animal Form*. University of Chicago Press.
- Rankin, J. and Chavane, F. (2017). Neural field model to reconcile structure with function in primary visual cortex. *PLOS Computational Biology*, 13(10):1–30.
- Royama, T. (1984). Population dynamics of the spruce budworm, *choristoneura fumiferana*. *Ecological Monographs*, 54(4):429–462.
- Royama, T. (2005). Moran effect on nonlinear processes. *Ecological Monographs*, 75(2):277–293.
- Schnackenberg, J. (1979). Simple chemical reaction systems with limit cycle behaviour. *Journal of Theoretical Biology*, 81:389–400.

- Schrödinger, E. (1944). *What is Life?* Cambridge University Press.
- Seirin Lee, S., Gaffney, E. A., and Baker, R. E. (2011). The dynamics of turing patterns for morphogen-regulated growing domains with cellular response delays. *Bulletin of mathematical biology*, 73(11):2527–2551.
- Senft, S. and Woolsey, T. (1991). Mouse barrel cortex viewed as Dirichlet domains. *Cerebral Cortex*, 1:348–363.
- Sharma, J., Angelucci, A., and Sur, M. (1998). Introduction of visual orientation modules in auditory cortex. *Nature*, page 820.
- Shimegi, S., Akasaki, T., Ichikawa, T., and Sato, H. (2000). Physiological and anatomical organization of multiwhisker response interactions in the barrel cortex of rats. *J Neurosci*, 20(16):6241–6248.
- Sneddon, I. N. (1966). *Special Functions of Mathematical Physics and Chemistry*. Oliver and Boyd.
- Sterling, P. and Laughlin, S. (2015). *Principles of Neural Design*. The MIT Press.
- Stevens, J.-L. R., Law, J. S., Antolík, J., and Bednar, J. A. (2013). Mechanisms for stable, robust, and adaptive development of orientation maps in the primary visual cortex. *Journal of Neuroscience*, 33(40):15747–15766.
- Swift, J. and Hohenberg, P. (1977). Hydrodynamic fluctuations at the convective instability. *Physical Review A, Atomic, molecular, and optical physics*, 15(1):319–328.
- Swindale, N. V. (1996). The development of topography in the visual cortex: A review of models. *Network: Comput Neural Syst*, 7(2):161–247.
- Thom, R. (1975). *Structural Stability and Morphogenesis*. Benjamin, Reading Massachusetts.
- Thom, R. (1989). *Paraboles et catastrophes*. Flammarion.
- Thompson, D. T. (1917). *On growth and form*. Cambridge University Press.
- Turing, A. (1952). The chemical basis of morphogenesis. *Phil. Trans. R. Soc. Lond. B*, 237:37–72.

- Varea, C., Aragón, J., and Barrio, R. (1999). Turing patterns on a sphere. *Physical review. E, Statistical physics, plasmas, fluids, and related interdisciplinary topics*, 60(4):4588–4592.
- Waddington, C. (1948). The genetic control of wing development in *Drosophila*. *Journal of Genetics*, 1:75–113.
- Welker, C. and Woolsey, T. (1974). Structure of layer iv in the somatosensory neocortex of the rat: description and comparison with the mouse. *Journal of Comparative Neurology*, 158:437–453.
- Wilson, S. and Prescott, T. (2021). Scaffolding layered control architectures through constraint closure: Insights into brain evolution and development. *Philosophical Transactions of the Royal Society B*, (in press).
- Wilson, S. P. and Bednar, J. A. (2015). What, if anything, are topological maps for? *Developmental Neurobiology*, 75(6):667–681.
- Wilson, S. P., Bednar, J. A., Prescott, T. J., and Mitchinson, B. (2011). Neural computation via neural geometry: A place code for inter-whisker timing in the barrel cortex? *PLoS Computational Biology*, 1(1):1.
- Wilson, S. P., Law, J. S., Mitchinson, B., Prescott, T. J., and Bednar, J. A. (2010). Modeling the emergence of whisker direction maps in rat barrel cortex. *PLoS One*, 5(1):e8778.
- Wolf, F. (2005a). Methods and models in neurophysics. *Lecture notes of the Les Houches summer school 2003*, Session LXXX:575–683.
- Wolf, F. (2005b). Symmetry, multistability, and long-range interactions in brain development. *Physical Review Letters*, 95:208701–208704.
- Wolf, F. and Geisel, T. (1998). Spontaneous pinwheel annihilation during visual development. *Nature*, 395:73–78.
- Woolsey, T., C. W., and Schwartz, R. (1975). Comparative anatomical studies of the SmL face cortex

with special reference to the occurrence of “barrels” in layer iv. *Journal of Comparative Neurology*, 164:79–94.

Xu, X., Anderson, T. J., and Casagrande, V. A. (2007). How do functional maps in primary visual cortex vary with eccentricity? *Journal of Comparative Neurology*, 501(5):741–755.